THE DEVELOPMENT OF IGNITION RESISTANT MAGNESIUM ALLOYS VIA STRONTIUM AND CALCIUM ALLOYING

Luis Angel Villegas-Armenta

Department of Mining and Materials Engineering

McGill University, Montréal, QC, Canada

April 2020

A thesis is submitted to McGill University in partial fulfillment of the requirements of the degree of Doctor of Philosophy

Abstract

The search for obtaining a competitive edge in the aerospace industry is pushing the boundaries of the commonly used materials for aircraft construction. Mg has not been used due to the perceived fire risk that this metal possesses, however, its low density (1.7 g/cm^3) represents an asset that should not be underestimated. As an example, if only the aluminum components in the passenger seats of an Airbus A380 were replaced by Mg (540 seats approximately), more than 5000 kilograms could be reduced from the plane weight. This potential has led the aircraft companies and Mg producers to work with the Federal Aviation Administration (FAA) to modify the standards on Mg ignition. Pure Mg ignites at ~650 °C and the commonly used alloys AZ (Aluminum-Zinc) and AM (Aluminum-Manganese) have even lower ignition temperature. Currently only two rare-earth containing Mg alloys have been identified as having passed the new FAA/SAE flammability test for Mg alloys (WE43 and Elektron 21®). There is now a drive for new research on the development of ignition-proof Mg alloys.

The present thesis is aimed at studying the potential of Sr and Ca alloying for the development of ignition-resistant Mg alloys. The use of these elements was motivated by the necessity to develop ignition resistant Mg alloys which are not mostly dependent on the use of rare-earth elements.

The results presented in this thesis have demonstrated that the simultaneous use of Sr and Ca in Mg improves the formation of a compact oxide scale at high temperatures. This oxide scale develops at the gas/oxide interface, where CaO is formed mostly in the solid-state while SrO becomes predominant during the liquid state. A new parameter, the Effective Pilling-Bedworth Ratio (EPBR), was developed in this study, which is the ratio of the volume of the composite oxide that forms to the volume of the Mg alloy substrate. The additions need to have an EPBR greater

than 1 and have a Gibb's free energy of oxidation more negative than Mg to ensure the formation of a relatively thin but compact composite oxide over the Mg alloy.

An important factor was isolated; that of heating rate which governs the ignition temperature of binary Mg-Sr and Mg-Ca alloys. It was discovered that, while the use of different heating rates does not alter significantly the ignition temperature of pure Mg, there are significant changes in some binary systems. Mg-Sr alloys displayed the most dramatic change, going from reaching temperatures between 750-800 °C adding 1-2.4 wt% to igniting as soon as the alloys were molten (~640 °C). Mg-Ca alloys ignition temperatures were affected by the heating rate only when 2 and 3 wt% Ca was added. The Mg-1Ca wt% alloy seemed unaffected. Microstructural and surface analysis of both binary alloys revealed the existence of underlying mechanisms not reported before. The observed differences in the Mg-Ca alloys were attributed to the formation of molten eutectic pools during the semi-solid state that proved to be thermodynamically more resistant to the oxidation than the solid intermetallics once the semi-solid range was reached. A low heating rate promoted the formation of these oxidation-resistant pools, while a high heating rate resulted in the excessive oxidation of the solid intermetallics.

For the Mg-Sr binary alloys, it was found that its low oxygen affinity against Mg hinders its effectiveness protecting the alloy when a high heating rate is used; causing profuse oxidation from the interdendritic regions and developing a non-protective oxide scale with large internal stresses. A low heating rate promotes the formation of Sr-rich pools which in turn allows the formation of a continuous SrO scale at the gas/oxide interface, hindering further oxidation during the liquid state.

Résumé

La recherche d'un avantage concurrentiel dans l'industrie aérospatiale repousse les limites des matériaux couramment utilisés pour la construction aéronautique. Le Mg n'a pas été utilisé en raison du risque d'incendie perçu que ce métal possède. Cependant, sa faible densité (1,7 g / cm3) représente un atout à ne pas sous-estimer. Ce potentiel a conduit les entreprises aéronautiques et les producteurs de magnésium à collaborer avec l'Administration Fédérale de l'Aviation (FAA) dans le but modifier les normes en matière d'ignition du magnésium. Le Mg pur s'enflamme à environ 650 ° C et les alliages couramment utilisés, AZ (aluminium-zinc) et AM (aluminium-manganèse), ont une température d'ignition encore plus basse. Aujourd'hui, seul deux alliages de Mg contenant des terres rares ont été identifiés comme ayant réussi le nouvel essai d'inflammabilité FAA / SAE des alliages de Mg (WE43 et Elektron 21 ™).

La présente thèse vise à étudier le potentiel du Sr et le Ca pour le développement d'alliages de Mg résistant à l'inflammation. L'utilisation de ces éléments a été motivée par la nécessité de développer des alliages de magnésium résistants à l'inflammation qui ne dépendent pas uniquement de l'utilisation d'éléments obtenus à partir de terres rares. Les résultats présentés dans cette thèse ont démontré que l'utilisation simultanée de Sr et de Ca dans le Mg améliore la formation d'une couche d'oxyde compact à des températures élevées. Cette couche d'oxyde se développe à l'interface gaz / oxyde, où le CaO se forme principalement à l'état solide, tandis que le SrO devient prédominant à l'état liquide. Un nouveau paramètre, le Rapport Effectif Pilling-Bedworth, a été développé dans cette étude. Il s'agit du rapport entre le volume de l'oxyde composite formé et le volume du substrat en alliage de Mg. Les additions doivent avoir une valeur EPBR supérieure à 1 et une énergie d'oxydation libre de Gibb plus négative que le Mg afin

d’assurer la formation d’un oxyde composite relativement mince mais compact dans l’alliage de Mg.

Un facteur important a été isolé; celui de la vitesse de chauffage qui régit la température d'inflammation des alliages binaires Mg-Sr et Mg-Ca. Il a été découvert que, bien que l’utilisation de vitesses de chauffage différentes ne modifie pas de manière significative la température d’inflammation du Mg pur, il existe des modifications importantes dans certains systèmes binaires.

Les alliages de Mg-Sr ont présenté le changement le plus spectaculaire, allant de l’atteinte de températures comprises entre 750 et 800 ° C en ajoutant 1-2,4% en poids à l’inflammation dès que les alliages étaient fondus (~ 640 ° C). Les températures d'inflammation des alliages Mg-Ca n'étaient influencées que par la vitesse de chauffage seulement lorsque des teneurs de 2 et 3% en poids de Ca étaient ajoutées. L'alliage de Mg-1Ca % en poids ne semblait pas affecté. L'analyse microstructurale et superficielle des deux alliages binaires a révélé l'existence de mécanismes sous-jacents non signalés auparavant. Les différences observées dans les alliages Mg-Ca ont été attribuées à la formation de bassins eutectiques en fusion au cours de l'état semi-solide, qui s'est révélée être thermodynamiquement plus résistante à l'oxydation que les composés intermétalliques solides une fois que l’état semi-solide a été atteint. Pour les alliages binaires Mg-Sr, il a été constaté que la faible affinité du Sr pour l'oxygène contre le Mg entrave son efficacité en protégeant l'alliage lorsqu'un taux de chauffage élevé est utilisé; provoquant une oxydation abondante à partir des régions inter-dendritiques et en développant une couche d'oxyde non protectrice avec de fortes contraintes internes. Une faible vitesse de chauffage favorise la formation de bassins riches en Sr, ce qui permet à son tour la formation d'une couche continue de SrO à l'interface gaz / oxyde, empêchant une oxydation supplémentaire pendant l'état liquide.

Acknowledgements

I would like to thank the following people for their valuable support during my Ph.D. journey:

Professor Mihriban O. Pekguleryuz for her constant support during my Ph.D. studies; her teachings and guidance were fundamental for my formation as a researcher.

Professor Robin A. L. Drew for his valuable discussions and insights during the preparation of this work.

Konstantinos Korgiopoulos for his unwavering resolve in all the tasks we did together and for being an excellent colleague and friend.

Amir R. Farkoosh for his support, teachings, and patience during the early years of my Ph.D.

Pierre Vermette, for his assistance and teachings during the casting process of my alloys.

To all my laboratory partners through these years for their help and friendship; Karan Narang, Brian Cook, Dr. Mert Celikin, Dr. Alireza Sadeghi, Dr. Yasser Zedan, and Dr. Baoqi Guo.

Sunyong Kwon for his valuable insight in thermodynamic calculations.

The McGill Facility for Electron Microscopy Research (FEMR), particularly to David Liu and Weawkamol Leelapornpisit.

To all my friends in the Mining and Materials department; thanks for making my years here such an amazing experience.

To my family, for supporting me even when it meant being away from home for so many years.

My wife, Dulce Diana, who is an essential part of my life and accompanied me during every step of this journey.

Contributions of Authors

This is a manuscript-based thesis containing four manuscripts. I, Luis A. Villegas-Armenta, performed the required experiments, wrote the manuscripts and integrated them into a thesis according to the guidelines described by the Graduate and Postdoctoral Studies office of McGill University. Dr. Mihriban O. Pekguleryuz, as my thesis supervisor, guided the development of my research and reviewed my manuscripts, while Dr. Robin A. L. Drew supported the research by

collaborating in the discussion of the manuscripts and the description of the observed phenomena. Detailed contributions are described below. These manuscripts are presented from Chapter 4 to Chapter 7:

Chapter 4

The Ignition Behavior of a Ternary Mg–Sr–Ca Alloy, LA. Villegas-Armenta and M.O. Pekguleryuz, (2020), Adv. Eng. Mater. doi:10.1002/adem.201901318".

In this manuscript, I performed the required experiments and wrote the manuscript. Prof. M. O. Pekguleryuz proposed the influence of the Effective Pilling Bedworth Ratio in the ignition temperature of Mg alloys.

Chapter 5

The Ignition Behavior of Mg-Ca binary alloys: The Role of Heating Rate. L.A. Villegas-Armenta, R. A. L. Drew, M. O., Pekguleryuz. Oxidation of Metals (2020). *In production.*

In this manuscript, I performed the required experiments and wrote the manuscript. Prof. M. O. Pekguleryuz and I proposed the oxidation resistant behaviour of molten pools through thermodynamic calculations, while Prof. R. A. L. Drew discussed the oxidation mechanism that influenced the observed ignition behaviour.

Chapter 6

Understanding Oxide-Scale Evolution on Ignition Resistant Mg-3Ca Alloy at Low and High Heating Rates. L.A. Villegas-Armenta, R. A. L. Drew, M. O., Pekguleryuz. *To be submitted.*

In this manuscript, I performed the required experiments and wrote the manuscript. In collaboration with Prof. M. O. Pekguleryuz and Prof. R. A. L. Drew, we defined the phenomena behind the oxide scale growth in the Mg-3Ca alloy, based in the XPS experimental observations.

Chapter 7

The Effect of Heating Rate in the Effectiveness of Sr as an Alloying Element for Ignition Resistance Improvement. L.A. Villegas-Armenta, R. A. L. Drew, M. O. Pekguleryuz. *To be submitted.*

In this manuscript, I performed the required experiments and wrote the manuscript. Prof. M. O. Pekguleryuz, Prof. R. A. L. Drew and I we discussed all the possible causes for the early ignition of Mg-Sr samples, reaching a consensus in the mechanism observed.

Table of Contents

List of Figures

List of Tables

Chapter 1 - General Introduction

1.1 The Importance of Mg for the Aerospace Industry

Magnesium is a material of interest for the aerospace industry due to its lower density (1.8 g/cm^3) compared to other structural materials like aluminum (2.7 g/cm^3) or titanium (4.5 g/cm^3). Due to the growing concern to reduce fuel consumption and the search to obtain a competitive edge in airplane performance, the development of Mg alloys has regained interest in the last decades. It is known that the use of less dense materials, along with a proper design, represents a

significant improvement over the use of structure-efficient heavy materials [1], such as high strength steels.

When compared to polymeric materials, Mg has better mechanical properties, electrical and thermal conductivity and, unlike some composite materials, has the potential to be recycled [2], reducing the waste generated during manufacture and at the end of their life-cycle. Magnesium use is also of interest for space applications due to its ability to withstand ozone-free radicals, shortwave electromagnetic radiation, and high energy particles, [3]. Considering the high expenses required to place vehicles, satellites, and other payloads in orbit, Mg would be a viable alternative to reduce the structural weight imposed by other heavier materials. These characteristics are the basis for the long-standing interest in magnesium for aeronautic applications, particularly in the military aircraft. During WWI, Mg production raised to 3000 pounds per year for different applications, but after the end of the war, its production stopped being profitable and remained being used mostly for pyrotechnics [4]. However, Mg production for the aeronautic industry took importance during the WWII, where the production of Mg reached above 160,000 metric tons in the U.S. to produce airplanes such as B-36 bomber which contained 8620 kg of Mg components [5]. After WWII, the difficulties to translate Mg use from warplanes to civilian use was magnified by its costly fabrication. Even when pure Mg and pure Al could be produced at a similar price, the fabrication of Mg components was three times higher [6]. The U.S. production of Mg went down to only 5300 metric tons by 1946, while the plants that existed in Germany were dismantled and taken to the USSR. The Korean War brought a new impetus to Mg production that reflected on the increase of production capacity in the U.S. by Dow Chemical [7]. Peacetime applications of Mg ranged from automotive use by VW in the 70s with AS41 (Mg-Al-Si), AZ91(Mg-Al-Zn) for structural applications and ZE41(Mg-Zn-RE-Zr), or QE22 (Mg-RE-Ag-Zr) for engine components

on several military and civilian aircraft [8]. Thorium containing Mg alloys reached impressive strength levels but were discontinued due to the radioactivity of thorium [9].

The rise and fall in Mg production continued through the century, but the perceived limitation of Mg regarding corrosion and ignition has limited the use of this metal in structural applications. The weak corrosion resistance was addressed by the development of different surface treatment technologies and the development of Mg alloys with controlled impurity levels [10-15]. Development of alloys for the automotive applications included the AJ62 (Mg-Al-Sr) alloy used in the BMW 3.0-liter engine block [16] and AE44 alloy used in the Corvette engine cradle [17].

The aerospace industry is more weight sensitive, but largely refrains from the use of magnesium alloys due to its deficient oxidation and ignition resistance. The use of magnesium in commercial aircraft inside in seat components; seat spreaders, backrests, armrests, rear legs, and front legs, overhead bins, and doors [18] (as shown in Fig. 1), could lead to a 30% reduction in weight. However, major industrial players such as Airbus, Boeing, and Embraer did not adopt the use of Mg [19] due to challenges that needed to be overcome.

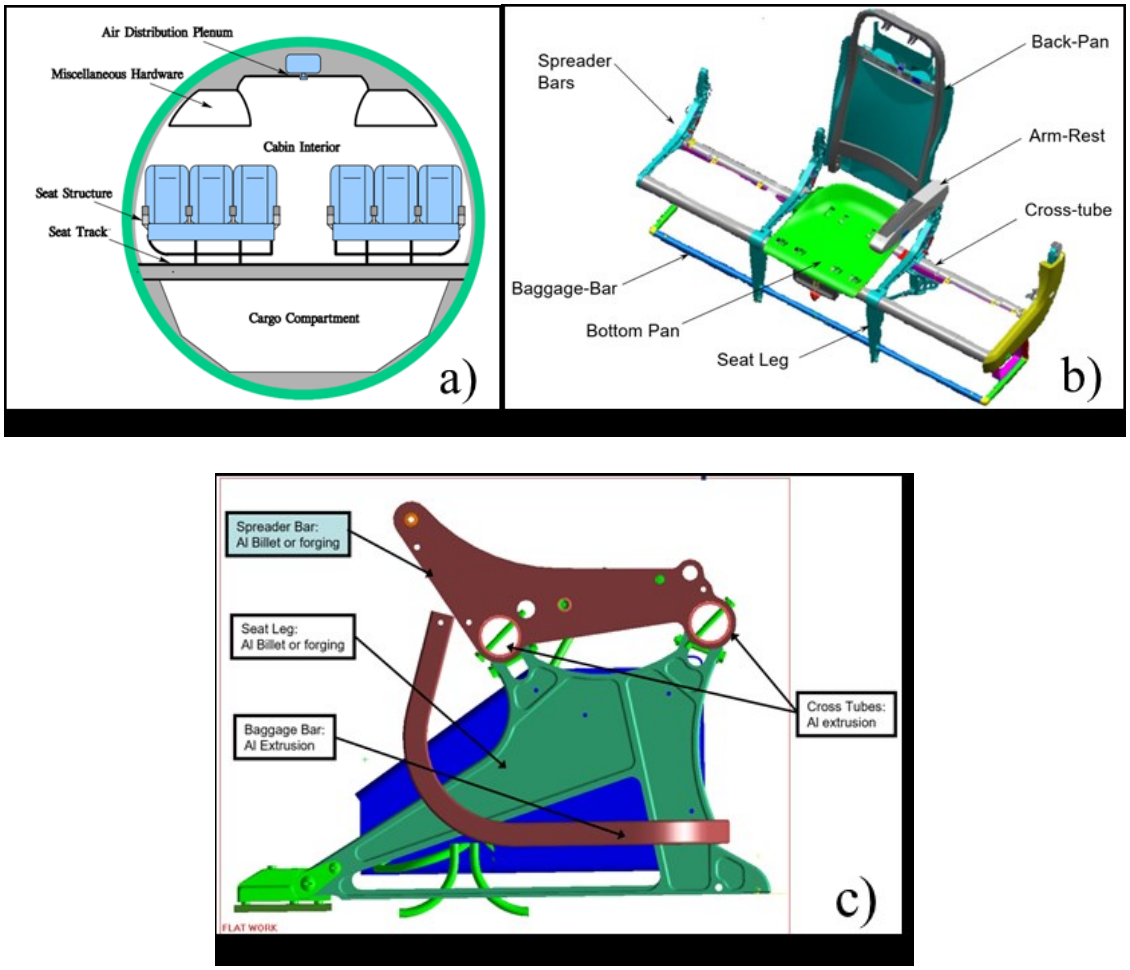

Fig. 1.1. Components in the commercial aircraft cabin (a) and seat assembly (b) with the potential to be manufactured in Mg. A detailed image of the cast and extruded seat components is shown in (c) [18].

In commercial aircraft, the use of Mg as part of cabin components must comply with specific requirements established by the Federal Aviation Administration (FAA), due to the perceived in-flight and post-crash fire hazards [20]. In recent years, tests performed by the FAA [21] demonstrated that Mg ignition resistance is highly composition-dependent, where regular commercial alloys such as AZ (Mg-Al-Zn) series have poor performance, while rare earth-containing alloys, such as WE43 (Mg-Y-RE), offer a safer alternative during flammability tests.

The SAE Aerospace Standard AS8049 was revised in August 2014 [22], which opened the door for the development of new magnesium alloys that could be not only as part of the seat structure but in overhead ducts, galley, lavatory, and floor components as well [23]. Recently, the European Aviation Safety Agency started the revision of the conditions defined by the FAA [24].

Table 1.1. Alloy design parameters for the development of commercial aircraft cabin Mg components

Requirements	**The parameter**	**Target quantities**	**Comments**	**Ref.**
Ignition Temperature	Self-ignition temperature (T_i)	T_i > 750 °C (induction furnace) WE43 T_i > 644 °C (resistance furnace) WE43		[25] [26]
Flammability Test	Time to burn with sustained ignition (t_i) & weight loss (w_l)	t_b > 2 minutes W_l < 10 % m_o	Ch. 25 of the FAA Fire Safety Handbook	[27]
Mechanical Properties	Ultimate tensile strength, ductility	**WE43** UTS = 250 MPa; ε = 2 % **Elektron 21** UTS = 280 MPa; ε = 5% **Elektron 43 (Wrought, Longitudinal)** UTS = 352 MPa; ε = 11.5 %	Alloys approved are listed on the FAA report DOT/FAA/TC13/52	[21]
Process: 1. Cast 2. Wrought	1. Castability, fluidity, porosity. 2. Extrudability, formability	**WE43 (Castability and extrudability) and Elektron 21 performance (Castability).**		

Currently, only the alloys Elektron® 43 (a wrought version of WE43) and Elektron® 21 by Magnesium Elektron are considered safe to be used as part of the seat structure in civil aircraft after eight years of work to remove the previously mentioned ban [28]. Because these alloys have passed the flammability tests defined by the FAA to be deemed safe and having in mind that flammability/ignition resistance is mostly dependant on the chemistry of the alloy, new alloys developed should reach or surpass at least WE43 capabilities. Table 1 shows a summary of some characteristics relevant to the development of future alloys that could be used as part of cabin components.

1.2 Objective of the Research: The Development of Mg Ignition Resistant Alloys

The ignition behavior of an alloy with several phases is very complicated. The mechanisms have not been well studied, but the formation of MgO through an exothermic reaction, which increases the surface temperature leading to Mg vaporization, is the main factor in the ignition of Mg alloys. There are consequently ways proposed to improve the ignition resistance of Mg by reducing/minimizing MgO formation:

(i) *By forming a protective oxide scale:* Use alloying elements that form an oxide scale which reduces the contact between the metal and an oxidizing agent and consequently minimizes the exothermic reaction that forms MgO. (ii) *By designing a self-healing oxide scale:* using elements in the alloy that oxidize preferentially when the oxide scale cracks, again minimizing MgO. (iii) *By altering the surface chemistry* to form phases with a lower tendency to MgO formation. These effects can be enhanced by alloying with surface-active elements which segregate to the surface of the solid or liquid Mg alloy. The consequence is the reduction of the Mg content on the surface

exposed to the oxidizing environment and the selective oxidation of the surface-active elements, resulting in a reduction of the Mg vaporization.

The two ignition resistant alloys that have currently passed the FAA flammability test both contain rare-earth additions. It is strategically vital to develop alternate alloys that eliminate the dependence on rare-earths. The long-term objective of this thesis work is to develop ignition resistant Mg alloys using alloying elements calcium (Ca) and strontium (Sr), which are known to be surface-active in magnesium. Sr is selected because of its surface-active behavior and proven effectiveness for ignition resistance demonstrated by our research group [29]. The improvement was attributed mainly to the surface enrichment of Sr, which can prevent the Mg evaporation due to the formation of MgO and consequent ignition. However, high amounts of Sr could lead to reduced mechanical resistance. Hence, its weight percentage must be reduced to improve the mechanical performance, while maintaining the ignition resistance. Ca, on the other hand, is an element whose oxide (CaO) is more stable in terms of Gibbs energy than MgO, making it a suitable candidate for ignition resistance. Its capacity as an ignition-improvement alloying element in Mg has been previously reported [30-36]; however, the mechanisms of Ca in improving the ignition behavior as a function of composition are not well understood.

Hence, this thesis aims to understand the various factors affecting the ignition of Mg-Ca and Mg-Sr alloys and to find the underlying mechanisms affecting their ignition temperature.

1.3 Thesis Structure and Chapter Description

The present manuscript contains 10 chapters, including the current general introduction. Chapter 2 consists of a literature review of the relevant topics required to understand the ignition behavior of Mg, along with a summary of the research progress made to date. Chapter 3 describes the experimental set up used to synthesize the used alloys and the furnace configuration used for

the ignition testing. Some details concerning the microstructural and oxide scale characterization are presented as well. Chapter 4 evaluates the feasibility of a Mg-Sr-Ca system as an ignition-resistant alloy, while Chapter 5 contains the work made for the analysis of the heating rate effect on Mg-Ca binary alloys. Chapter 6 concentrates on the in-depth analysis of the ignition mechanism of the Mg-3Ca alloy when heated using two different heating rates. Chapter 7 describes the effect of heating rate in Mg-Sr alloys and the in-depth analysis of a Mg-2.4 Sr alloy. A general discussion is presented in Chapter 8, finally, the conclusions of the work and the suggestions for future work are presented in Chapter 9.

1.4 References for Chapter 1

[1] T. Marker, "Update on Flammability Testing of Magnesium Alloy Components," in International Aircraft Materials Fire Test Working Group: Federal Aviation Administration, 2008.

[2] A. P. Mouritz, "Introduction to Aerospace Materials," Cambridge, UK: Elsevier Science & Technology, 2012, pp. 569-600.

[3] B. Mordike and T. Ebert, "Magnesium: properties—applications—potential," Mater. Sci. Eng. A, vol. 302, no. 1, pp. 37-45, 2001.

[4] F. H. Froes, D. Eliezer, and E. Aghion, "The science, technology, and applications of magnesium," J. Met., journal article vol. 50, no. 9, pp. 30-34, September 01 1998.

[5] R. E. Brown, "Magnesium wrought and fabricated products yesterday, today and tomorrow," Magnesium Technol., pp. 155-163, 2002.

[6] S. Mathaudhu, E. Nyberg, and A. P. G. WMM-F, "Magnesium Alloys in Army Applications: Past, Current and Future Solutions," ed: Minerals, Metals and Materials Society/AIME, 2010.

[7] W. O. Blanchard, "Magnesium—The Metal for Motion," Journal of Geography, vol. 47, no. 1, pp. 31-36, 1948/01/01 1948.

[8] M. B. Lieberman, "The magnesium industry in transition," Review of Industrial Organization, vol. 19, no. 1, pp. 71-80, 2001.

[9] B. Gwynne, P. Lyon, and M. E. UK, "Magnesium alloys in aerospace applications, past concerns, current solutions," in Trienn. Int. Aircr. Fire Cabin Saf. Res. Conf, 2007.

[10] E. F. Emley, "Principles of magnesium technology," 1966.

[11] J. E. Hillis, "The effects of heavy metal contamination on magnesium corrosion performance," SAE Trans., pp. 553-559, 1983.

[12] K. Reichek, K. Clark, and J. Hillis, "Controlling the salt water corrosion performance of magnesium AZ91 alloy," SAE Trans., pp. 318-329, 1985.

[13] J. E. Hillis and K. Reichek, "High Purity Magnesium AM60 Alloy: The Critical Contaminant Limits and the Salt Water Corrosion Performance," SAE Trans., pp. 227-234, 1986.

[14] W. E. Mercer and J. E. Hillis, "The critical contaminant limits and salt water corrosion performance of magnesium AE42 alloy," SAE Technical Paper0148-7191, 1992.

[15] R. W. Murray and J. E. Hillis, "Magnesium finishing: chemical treatment and coating practices," SAE Technical Paper0148-7191, 1990.

[16] J. E. Hillis and S. O. Shook, "Composition and performance of an improved magnesium AS41 alloy," SAE Technical Paper0148-7191, 1989.

[17] M. K. Kulekci, "Magnesium and its alloys applications in automotive industry," Int. J. Adv. Des. Manuf. Technol., journal article vol. 39, no. 9, pp. 851-865, November 01 2008.

[18] J. Aragones, K. Goundan, S. Kolp, R. Osborne, L. Ouimet, and W. Pinch, "Development of the 2006 corvette z06 structural cast magnesium crossmember," No. 2005-01-0340. SAE Technical Paper, 2005.

[19] I. Ostrovsky and Y. Henn, "Present state and future of magnesium application in aerospace industry," in International Conference “New Challenges in Aeronautics”, Moscow, 2007.

[20] T. Marker, "The Use of Magnesium in Airplane Interiors," in International Aircraft Materials Fire Test Forum, 2007.

[21] T. R. Marker, "DOT/FAA/TC-13/52 - Development of a Laboratory-Scale Flammability Test for Magnesium Alloys Used in Aircraft Seat Construction," Federal Aviation Administration, New Jersey, 2014.

[22] C. P. Sarkos, "Application of full-scale fire tests to characterize and improve the aircraft postcrash fire environment," Toxicol., vol. 115, no. 1-3, pp. 79-87, 1996.

[23] T. Marker, "The Use of Magnesium in Airplane Interiors," in The Sixth Triennial International Fire and Cabin Safety Research Conference. Atlantic City, NJ, USA, 2010.

[24] E. Canari, "Revised EASA SC on Use of Magnesium Alloys for Passenger Seat Components," in International Aircraft Materials Fire Testing Working Group Meeting, Cologne, 2017.

[25] N. V. R. Kumar, J. J. Blandin, M. Suery, and E. Grosjean, "Effect of alloying elements on the ignition resistance," Scr. Mater., vol. 49, pp. 225–230, 2003.

[26] M. Liu, D. S. Shih, C. Parish, and A. Atrens, "The ignition temperature of Mg alloys WE43, AZ31 and AZ91," Corrosion Science, vol. 54, pp. 139–142, 2012.

[27] A. Horner, "Aircraft Materials Fire Test Handbook," No. DOT/FAA/AR-00/12. United States. Federal Aviation Administration, 2000.

[28] (2015). Magnesium Elektron Welcomes New Standard on Use of Magnesium in Commercial Aircraft Seats Available: https://www.businesswire.com/news/home/20150831005314/en/

[29] D. S. Aydin, Z. Bayindir, and M. O. Pekguleryuz, "The effect of strontium (Sr) on the ignition temperature of magnesium (Mg): a look at the pre-ignition stage of Mg–6wt% Sr," J. Mater. Sci., vol. 48, no. 8117–8132, 2013.

[30] B.-H. Choi, B.-S. You, W.-W. Park, Y.-B. Huang, and I.-M. Park, "Effect of Ca addition on the oxidation resistance of AZ91 magnesium alloys at elevated temperatures," Met. Mater. Int., journal article vol. 9, no. 4, pp. 395-398, 2003.

[31] T.-S. Shih, J.-H. Wang, and K.-Z. Chong, "Combustion of magnesium alloys in air," Mater. Chem. Phys., vol. 85, no. 2, pp. 302-309, 2004.

[32] J.-K. Lee, H.-H. Jo, and S. K. Kim, "Effet of CaO addition on ignition behavior in molten AZ31 and AZ91D magnesium alloys," Rare Met., vol. 25, no. Special Issue, pp. 155-159, 2006.

[33] M. Sakamoto, S. Akiyama, and K. Ogi, "Suppression of ignition and burning of molten Mg alloys by Ca bearing stable oxide film," J. Mater. Sci. Lett., vol. 16, no. 1048-1050, 1997.

[34] S.-Y. Chang, M. Matsushita, H. Tezuka, and A. Kamio, "Ignition prevention of magnesium by simultaneous addition of calcium and zirconium," Int. J. Cast Met. Res., vol. 10, no. 6, pp. 345-351, 1998.

[35] F. Li et al., "Development of non-flammable high strength AZ91+ Ca alloys via liquid forging and extrusion," Mater. Des., vol. 99, pp. 37-43, 2016.

[36] D. B. Lee, "High temperature oxidation of AZ31 + 0.3 wt.%Ca and AZ31 + 0.3 wt.%CaO magnesium alloys," Corros. Sci., vol. 70, no. 243–251, 2013.

Chapter 2 - Literature Review on Mg Ignition and the Development of Ignition Resistant Mg Alloys

In this chapter, Section 2.1 explains the basics of Mg ignition and Section 2.2 presents the fundamental concepts related to oxidation at high temperatures. Sections 2.3 and 2.4 give the background on the high-temperature oxidation behavior of Mg along with mechanisms proposed in the literature for improving the ignition resistance of Mg through alloying. Section 2.5 reviews the literature on studies undertaken for improving the ignition resistance of Mg via the alloying route. Finally, Section 2.6 describes the Ignition and Flammability Tests conducted on Magnesium Alloys.

2.1 The Ignition of Mg

The susceptibility of a substance to undergo ignition depends on the formation of vaporized molecules which form a gaseous mixture with oxygen, causing combustion at high temperatures [1]. Accordingly, Mg ignites when there is a strong reaction between Mg vapor and oxygen, and not through a reaction directly at the metal surface [2]. A significant surface temperature increase is required to vaporize Mg and undergo ignition. Fassell et al. [3] defined the ignition temperature as an *"explosion temperature"*, which is the point where Mg oxidizes vigorously, and a flame appears. This is because Mg oxidation represents a driving force for ignition due to the heat generated by this reaction. They defined the ignition temperature of pure Mg as 623 °C under an oxygen atmosphere. Furthermore, Hill et al. [4] defined the spontaneous-ignition temperature as the point where the heat generated by oxidation surpasses the heat dissipated by the surface. Mg

vapor oxidation would increase exponentially due to the temperature dependence of this phenomenon, leading to eventual ignition, as shown in Fig. 2.1; the ignition temperature is the intersecting point between the curves representing the heat loses (due to conduction, convection, radiation or melting) and the heat generated by oxidation when the metal temperature is plotted against the heat flow rate.

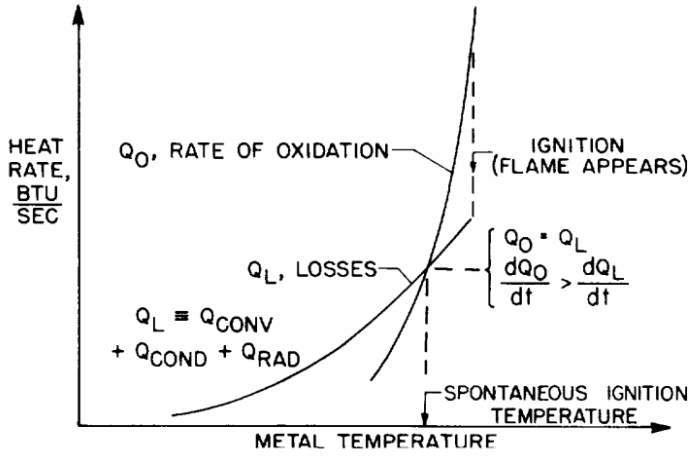

Fig. 2.1. Curves are defining the increase in metal temperature due to the oxidation and the losses due to convection, radiation, and conduction. The intersection between these two curves defines the spontaneous ignition temperature as defined by Hill et al. [4].

In the observations made by Derevyaga et al. [5], when Mg is held at its melting temperature (650 °C) under an oxidizing atmosphere, protuberances are formed at the surface which proliferates through pores or cracks in the oxide scale. The heat evolved from the surface reaction alone is insufficient for the thermal breakaway to take place. However, the surface temperature increase would promote Mg vaporization. In sections such as cracks and pores in the oxide scale, the vapor generated would react with the oxygen resulting in a thermal breakaway and consequential ignition. It is possible to see the intimate relationship that exists between Mg ignition

and high-temperature oxidation behavior. Avoiding vigorous oxidation of Mg is the primary concern when an increase in Mg ignition temperature is searched.

2.2 Fundamentals of High-Temperature Oxidation

In general terms, *high-temperature oxidation* (also known as *gaseous oxidation*) occurs when a gas such as oxygen reacts with a metal, without the existence of an electrolyte. This process starts with the adsorption of oxygen over the metal surface. Since the physical adsorption bond of oxygen to the metal surface is not stable (<6 kcal/mol), oxygen chemically interacts with the metal through chemisorption, creating a stronger bond (>50 kcal/mol). This first layer is formed by atomic oxygen; if there is more oxygen available, the molecular oxygen piles up over the outer layer. Eventually, the chemisorption of molecular oxygen layer takes place, energetically favoring the transition from an adsorbed layer to an oxide scale that nucleates at metal imperfections such as edges, steps, and lattice defects (**Error! Reference source not found.**2.2), which are sites that favor the multilayer adsorption of oxygen [6] .

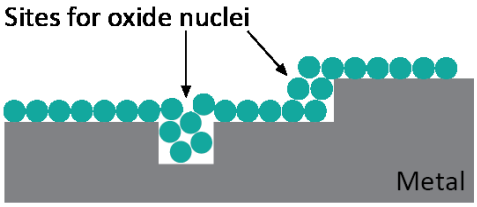

Fig. 2.2. Schematic diagram describing the *preferential oxide nucleation at the metal surface imperfections. Redrawn from [6].*

The formation of the oxide scale due to the interaction of a metal and oxygen can be expressed via two partial chemical reactions [7]:

$$\frac{1}{2}O_2 + 2e^- \rightarrow O^{-2} \quad (1)$$

$$M \rightarrow M^{2+} + 2e^{-} \quad (2)$$

Where the overall reaction is:

$$M + \frac{1}{2}O_2 \rightarrow MO \quad (3)$$

In reaction (1), oxygen is reduced to oxygen anions at the oxide/gas interface, while in reaction (2) the metal is oxidized to metal cations at the metal/oxide interface where the oxide scale allows mobility of both ions and electrons. Here, vacancy formation due to an interstitial ion from a lattice position (Frenkel defect) and vacancy formation due to a missing anion-cation pair (Schottky defects) [8] allow the ionic mobility, and hence, the reaction between these defects is considered to be a chemical reaction. For oxides with a predominantly ionic character such as MgO, the dominant reactions are those that maintain the compound stoichiometry. Hence, cations and anions diffuse trough lattice-defect sites and interstitial spaces, however, because of the higher electron mobility, the ionic conductivity will control the oxidation rate. A schematic diagram for this process is shown in Fig. 2.3.

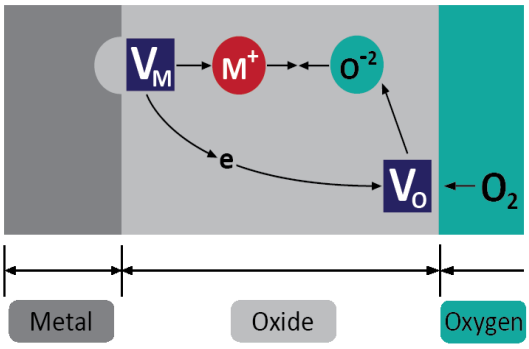

Fig. 2.3. The schematic diagram for the high-temperature oxidation of metal in oxygen. Redrawn from [7]. Metal vacancies formed due to cation formation are denoted as V_m, while vacancies formed due to anion formation are denoted by V_o.

The self-diffusion of ionic species can be either intrinsic or extrinsic [9]. Intrinsic diffusion represents the case when the diffusing species displace through the lattice due to thermal energy available and, by consequence, it is highly dependant on very high temperatures. This type of diffusion possesses high activation energy, which becomes higher for oxides formed by lighter metal ions, making it more challenging to take place. On the other hand, extrinsic diffusion depends on the existence of impurities and defects in the oxide scale and becomes the dominant mechanism at low temperatures. The mobility of ionic species may define the oxidation rate when the oxide scale represents a barrier for the contact between a metal and oxygen. However, the oxidation kinetics may follow a different trend in some cases, as explained in the next section.

2.2.1 Kinetics of Oxidation

When the oxidation rate of a metal surface is controlled by oxide growth, it will depend on the increase of the oxide layer thickness or its gain weight. However, if oxidation is independent of the thickness of the oxide scale formed (x), then the oxidation rate is defined by [10]

$$\frac{dX}{dt} = k_1 \tag{1}$$

Integrating (1) yields

$$X = k_1 t, \tag{2}$$

where k_1 is the linear rate constant and depends either on oxygen adsorption or oxygen partial pressure. This behavior can be observed where the oxide layer does not prevent the metal from interacting with oxygen

When diffusion through a continuous oxide scale becomes the controlling process, the transport mechanism can be attributed to concentration gradients [11]. In this case, a parabolic behavior that continuously reduces the oxidation rate can be observed, resulting in

$$X^2 = 2k_p t. \tag{4}$$

where k_p corresponds to the parabolic oxidation constant. The oxidation kinetics can also follow a logarithmic rate law when subjected to oxidation at low temperatures or with a gradual increase in temperature. In this model, a rapid increase in weight can be observed at the beginning, followed by an almost negligible increase. This can be attributed to an electrical field formed by the potential difference between the metal and the adsorbed oxygen, which leads to ion migration through the oxide layer almost independent from the temperature [12], where the film growth is controlled by the movement of mass, not the electron transfer [13].

A combination of trends can also occur. In the work presented by Pettit et al. [14], the transition from linear to parabolic rate law is observed during the high-temperature oxidation of iron in a CO-CO_2 mixture. At early stages where the oxide layer is thin, the oxidation rate is controlled by the formation of CO from CO_2 and the consequent adsorption of oxygen through the surface, with a thick oxide layer, the transition towards a parabolic rate law can be observed.

2.2.2 Thermodynamics of Oxidation

The tendency of an element to react with oxygen can be a useful tool to predict the oxide formation when a metal is subjected to high-temperature oxidation. This phenomenon represents a crucial factor for the ignition resistance of Mg and its alloys. It can be measured through the change in Gibbs energy for an oxide formation reaction.

The free Gibbs energy, according to the International Union of Pure and Applied Chemistry (IUPAC), is the "*thermodynamic quantity equal to the difference between the enthalpy of a system and the product of the thermodynamic temperature to the entropy of this system*" [15] and can be defined by equation 9:

$$G = H - TS = U + pV - TS, \quad (5)$$

where H represents the enthalpy, S entropy, T temperature, U internal energy, p pressure, and V the volume. Under constant temperature and pressure conditions, a chemical reaction can undergo only if the total Gibbs energy decreases, as the equilibrium state (when dS=0) coincides with its minimum value [16]. According to the second law of thermodynamics, if the change in Gibbs energy is lower than 0, the reaction will undergo spontaneously. A value equal to 0 defines the equilibrium state, while a value above 0 represents a non-spontaneous reaction.

In general terms, the Gibbs energy of a chemical reaction is determined by:

$$\Delta G°_{Reaction} = \Delta G°_{Products} - \Delta G°_{Reactants} \quad (6)$$

where ΔG° represents the Gibbs energy change under standard state conditions. If it is necessary to calculate the Gibbs energy change at non-standard conditions (e.g., high temperature, variable activities), we can define the change in Gibbs energy as:

$$\Delta G = \Delta G°_{Reaction} + RT\, ln\left(\frac{a_C^c a_D^d}{a_A^a a_B^b}\right) \quad (7)$$

where "a" represents the activities (or partial pressure for ideal gases) of every component in the reaction as:

$$aA + bB = cC + dD \quad (8)$$

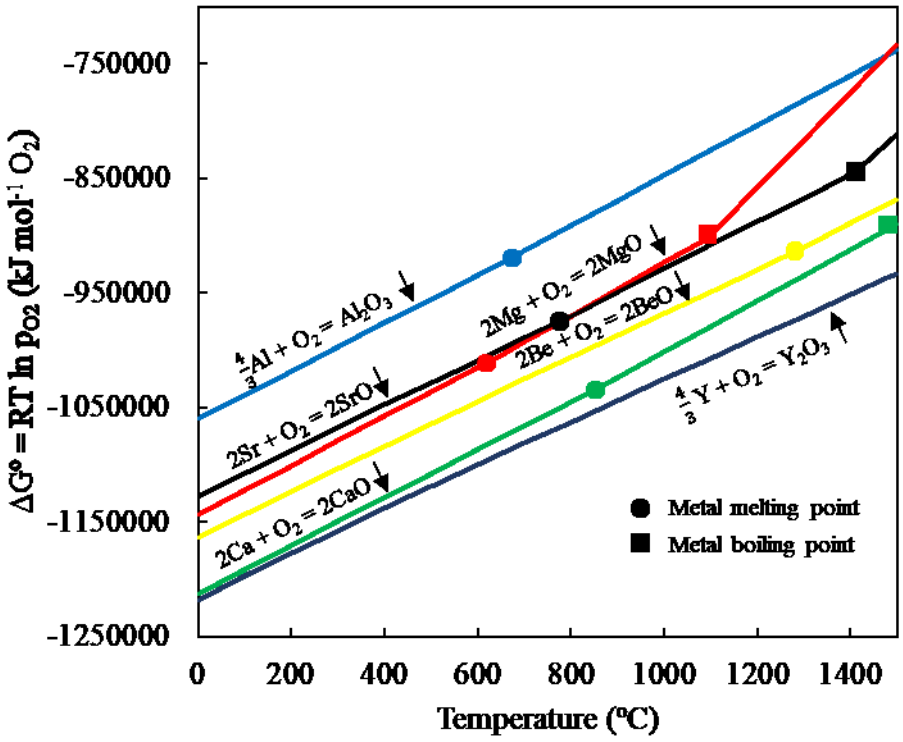

Fig. 2.4. Ellingham diagram for selected oxides. Calculated using FactSage™-FT lite software.

The most negative value for Gibbs energy change would define which oxide in a system is more likely to form, without considering kinetic factors. In Ellingham Diagrams (Fig. 2.4), the value of ΔG versus temperature is plotted, creating straight lines that define the trend of an oxide formation, considering 1 mol of O_2. This can give us an insight into the oxides more likely to form when a metal interacts with oxygen, where the lower values correspond to more stable oxides. In **Error! Reference source not found.**2.4, an Ellingham diagram for selected oxides is shown. As can be seen, Mg has one the highest affinities for oxide formation, making it more prone to oxidize in comparison to other elements. Notably, Ca in the same group of the periodic table has a higher affinity than Mg.

The oxygen activity in the Ellingham diagram assumes of 1 mole of O_2 reacting with a given element. However, the oxygen activity in the system also influences the outcome of oxide formation. The chemical reaction between a metal and oxygen can be written as:

$$M + O_2 = MO_2 \quad (9)$$

When the activities of the metal and the oxide are taken as 1, the partial pressure at which both species exist in the system can be defined by:

$$p_{O_2}^{M/MO_2} = \exp \frac{\Delta G^\circ}{RT} \quad (10)$$

where R represents the gas constant and T the temperature [17]. If the activities of both metal and oxide are different from 1, equation 8 can be written as:

$$p_{O_2}^{eq} = p_{O_2}^{M/MO_2} \frac{a_{MO_2}}{a_M} \quad (11)$$

The resulting pressure is commonly named decomposition pressure. This pressure can determine the existence of oxide over a metal surface. For example, in the case of Wüstite formation [10] which has a $p_{O_2}^{FeO}$ equal to 1.2×10^{-15} atm, no oxide will be formed until the oxygen partial pressure reach this value. If oxygen partial pressure is higher, the iron will oxidize until enough oxygen is consumed to lower the value below 1.2×10^{-15} atm.

2.3 The High-Temperature Oxidation of Mg

Mg ignition resistance can be related to its high-temperature oxidation behavior, as the formation of non-protective oxide scales results in a free contact between Mg vapor and O. When Mg enters in contact with the atmosphere, it oxidizes through the following exothermic reaction: $2Mg + O_2 \rightarrow 2MgO$.

The process starts with the oxygen adsorption on the surface, followed by the formation of MgO islands on the surface and continues with the growth of the oxide scale [18]. Mg is one of the metals with the highest oxygen affinity, but unlike other active materials like aluminum, which is protected by a passive Al_2O_3 layer, the MgO layer formed will change its behavior as the temperature is increased. MgO (also known as periclase) is a rock salt structure oxide (NaCl) which melts at 2852 °C, and a vaporizes at 3600 °C, making it resistant to degradation at high temperatures. It has a single cation site and a single anion site, for each one has octahedral coordination [19].

The MgO non-protective behavior is mostly attributed to the geometric mismatch between the hexagonal structure of Mg with the oxide layer formed on the surface, which leads to high compressive strain and eventual cracking [20]. However, at room temperature, the oxide scale formed over the surface of Mg provides protection against further oxidation due to its amorphous nature [21]. Once the metal surface has been completely covered, further oxidation at the surface will proceed by the diffusion of Mg^{+2} ions through MgO towards the oxide/gas interface. It was noted by Gulbransen [22] that the existence of a uniform oxide scale is just an approximation, given the fact that the grain orientation may affect the growth of the oxide scale in a polycrystalline metal. After the initial oxide formation, oxide growth continues through the formation of a fine mosaic structure randomly oriented (**Error! Reference source not found.**2.5). Further growth (thickness from 50 to 100 Å) would result in the formation of crystals following the original crystal habits. Addiss [23] indicated that the growth of MgO would be influenced by the crystallographic orientation of Mg. It was noted that oxide growth was faster in the basal plane than in the prismatic plane at initial stages of oxidation at 400 °C, but this trend changes after an oxide thickness of 70 Å, when the oxidation rate for the prismatic plane surpasses that of the basal plane. This was

attributed to structural changes in the oxide as the oxide shows a stronger preferred orientation in the basal plane than in the prismatic plane. From this point on, oxidation of Mg would proceed through two main mechanisms: (a) diffusion of Mg and O ions through the oxide scale and (b) the use of fast diffusion paths such as grain boundaries and defects.

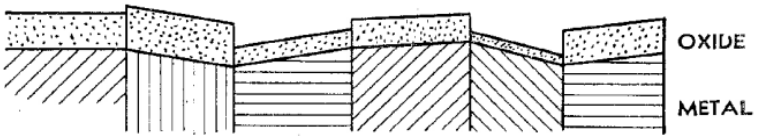

Fig. 2.5. Relationship between surface oxidation and grain orientation [22].

For scenario (a), and as mentioned in section 2.2, ion mobility within an oxide scale will have a significant impact on its behavior as a barrier for oxidation. Diffusion through MgO is mainly extrinsic. Hence it depends on the presence of vacancies for oxide growth. The displacement of a Mg or O ion to an interstitial site to create a vacancy (Frenkel defect) is energetically unfavorable when the enthalpy of formation of this defect is compared to the enthalpy of vacancy formation through the absence of an ionic pair (Schottky defect) [24, 25]. This makes the presence of vacancies in the lattice the dominant mechanism of ion transport through the oxide scale. It is important to note that though the displacement of smaller ions could still be possible in MgO for elements such as Be [19]. As previously explained, the former would depend on the presence of point defects and diffusion through the scale, making the process slower compared to other faster routes.

In the scenario (b), fast diffusion paths such as dislocations and grain boundaries play an essential role in Mg oxidation. Sakaguchi et al. [26], analyzed the contribution of dislocations to the effective diffusion of Mg ions through MgO. It was determined that diffusion is enhanced by

the presence of dislocation arrays when the dislocation density is higher than $8.1x10^{15}$ m^{-2}, and this contribution increases towards low temperatures (experiments were performed between 1100 and 1300 °C). In another study, Sakaguchi et al. [27] observed that a significant increase in diffusion through dislocation arrays, affects Ca^{2+} ions as well, even though the activation energy for this ion diffusion does not differ significantly between lattice and dislocation diffusion. The observed change was then attributed to the higher vacancy concentration in the dislocation pipe. Regarding grain boundaries, Hashimoto et al. [28] demonstrated that diffusion of oxygen ions through MgO grain boundaries is significantly faster compared to its diffusion through the lattice. This is especially important if we have in mind that diffusion of Mg ions through the MgO lattice is the dominant mechanism. Mg can also diffuse through MgO oxide grain boundaries significantly faster, as its activation energy is two thirds lower compared to the lattice diffusion activation energy [29].

Because of the nature of MgO cation mobility, it will tend to generate internal stresses to keep contact with the metal. This is because the metal atoms diffuse outwards during the oxidation process, leaving a depletion zone leading to the formation of voids in the oxide scale. Hence zones like corners and edges are more prone to ignition, as the protective ability of the oxide scale depends on the plasticity of the oxide to creep and maintain contact with the surface [17]. Increasing oxidation by either route will lead eventually to ignition if the temperature is continuously increased, as the MgO protective behavior observed is lost at higher temperatures. Gulbransen [30] defined that weight gain due to oxidation of pure Mg below 475 °C follows a parabolic rate, which is evidence of the formation of a protective oxide scale that retards oxidation and evaporation. However, at temperatures above 475 °C, the oxide scale starts to follow a linear trend, and Mg evaporation takes place, caused by the formation of a discontinuous cellular film

that does not offer protection for further oxidation. At this point, oxidation will proceed rapidly through direct evaporation where Mg evaporation is controlled by a rate defined by an Arrhenius relation [31] of K_{Evap} (g/cm^2 sec) = 0.6 exp - 25 000/RT.

This analysis reveals that the formation of MgO is clearly insufficient to prevent ignition once the temperature rises towards Mg melting temperature (650 °C). Alloying Mg with other elements modifies its oxidation behaviour. However, the modification of the oxide scale may not be enough to improve the ignition resistance. Thicker oxides usually lead to cracking and spalling changing the kinetics and the mechanisms of oxidation. The next section describes the factors governing the oxide scale formation and ignition of Mg alloys

2.4 Alloying Effects on Oxide Scale Formation and Ignition of Mg

Studies show that the addition of alloying elements to pure Mg can have a significant effect on its high-temperature oxidation resistance and its ignition resistance. The mechanisms governing these interactions are Reactive Element Effect (REE), Pilling-Bedworth Ratio (PBR), and the Wigner-Seitz Radius (WSR), which will be discussed in this section.

2.4.1 The Reactive Element Effect (REE)

The Reactive Element Effect (REE) consists in the addition of trace amounts of reactive elements such as Y, Ce, Hf, Gd, and La among others (not necessarily rare-earths) to improve the oxidation resistance of Mg alloys [32]. This effect is different from the common hypotheses that the formation of a compact and protective complex oxide scale between the oxygen/gas and the oxide/metal interfaces is needed to slow down oxidation and ignition. The REE hypothesis, on the other hand, centers on the hypothesis that the diffusion of the reactive element ions towards the native oxide grain boundaries (which are regions for preferential diffusion compared to the oxide

lattice) may block the outward metal cation diffusion through these channels, limiting the oxidation to the inward diffusion of oxygen. However, a more in-depth analysis of the mechanism behind the reduced oxidation rate is still required to fully understand this hypothesis.

A different approach regarding reactive elements is presented by Bobryshev et al. [33], where the ignition temperature of Mg was increased significantly with the addition 0.7 wt% of Er, Dy, Gd and Nd and 0.5 wt% of Y. The improvement was attributed to the modification of the oxidation sequence of Mg, where the more negative Gibbs energy of formation of the reactive element oxides modifies the growth sequence of the overall oxide scale. This concept has roots in the fact that reducing the oxidation of Mg, which is exothermic reduces the increase of surface temperature and the vaporization Mg that would lead to ignition.

2.4.2 The Concept of Pilling-Bedworth Ratio (PBR) on Mg Ignition Resistance

The Pilling-Bedworth Ratio (PBR) can be defined as the relation between the volumes of oxide formed from a certain amount of metal substrate and the metal itself, and can be calculated as follows [34]:

$$PBR = \frac{V_{oxide}}{V_{metal}}. \quad (12)$$

In the case of alloys, this value can be affected by both crystal structure and lattice constants, where a difference between the structure of the base metal and the alloy would lead to a difference in PBR [35]. It is generally considered that a PBR > 1 could mean the formation of a less porous oxide layer, as it is more compact and continuous, while a value below 1 could lead to a less protective porous oxide layer, as in MgO (PBR = 0.81). A PBR higher than 1, could lead to sizeable compressive stress along the oxide scale, will lose adhesion to the metal surface and eventually crack through spallation or blistering [36]. Both outcomes will result in weak oxidation

resistance. Some authors have attributed increases observed in ignition resistance to the high PBR of the oxides formed on the surface of Mg alloys [37-39], however, other oxides like CaO or SrO, both having a PBR<1, have a demonstrated effectiveness increasing the ignition resistance of pure Mg (discussed in Section 2.5). However, it is important to note that with this approach, the molar volume of the oxide is formed over the pure metal as a substrate, not over an alloyed material, which is the case for Mg alloys containing these alkaline-earth metals. In work presented by Kim et al. [40] some Mg binary systems are tested, where the PBR and the Gibbs energy of oxide formation are considered as criteria for alloying elements selection. However, even though elements such as Pr and La possess high oxygen affinity and PBR>1, the ignition temperature improvement was significantly low.

2.4.3 Wigner-Seitz Radius and Surface Segregation

Certain elements can be surface active in metals and lead to surface compositions that are more concentrated than the bulk both in the solid and liquid states. Surface activity is possible because the elements decrease the surface energy of the metal. Surface-active elements can minimize MgO formation by the fact that they decrease the Mg content of the surface and thereby reduce MgO formation and the resultant surface temperature increase and the eventual Mg vaporization.

One approach to predict the surface segregation of elements in metals is presented by Yamauchi [41] using a binary jellium model for a solid solution. This model defines that when the Wigner-Seitz radius of the solute element is larger than the solvent of the solution, then the surface segregation will take place because of the accompanying reduction in surface energy. The Wigner-Seitz (W-S) radius can define the degree of compactness of a material, as it is the radius that one atom occupies in a lattice [42]. The Density Functional Theory approach treats this as a system

governed by the change in Gibbs energy, relative to the concentration gradient between the bulk alloy and the surface. The relation between segregation potential per area (J/m^2) and the W-S radius for selected solutes at 5 at% for a Cu binary system, is calculated by Yamauchi, where ρ is defined as the relation between the solute and solvent W-S radius, as $\rho = \frac{r_{solute}}{r_{solvent}}$. It is demonstrated that a value of ρ above 1 would lead to surface segregation, showing good agreement with experimental data.

The application of this mechanism on Mg alloys was proposed by Aydin et al. [43], predicting the surface segregation of Sr because its Wigner-Seitz radius is 4.5 while the W-S radius of Mg is 2.66. This is related to the smaller Brillouin zone of solute elements with a sizeable W-S radius, which could then segregate to the surface in order to decrease the surface energy of the solvent metal. A comparison between different W-S radii compared to Mg is presented in Table 2.1. Elements like Ca, Y, Sr, or Er could show surface segregation as their ρ is higher than 1. Here Ca can be highlighted as having the highest ρ and the highest potential to surface segregate in Mg.

Table 2.1. Wigner-Seitz Radius and Maximum Solid Solubility of Selected elements that could show surface segregation in Mg according to Yamauchi rule.

Element	**Maximum Solid Solubility**		**Ref.**	**Wigner-Seitz Radius (a.u.)**	**Ref.**
	wt%	**at%**			
Be	*	*	[44]	1.87	[42]
Mg	-	-	-	2.66	[42]
Sc	24.6	14.99	[45]	3.35	[46]

Element	Maximum Solid Solubility		Ref.	Wigner-Seitz Radius (a.u.)	Ref.
	wt%	at%			
Y	11.4	3.4	[45]	3.78	[47]
Er	30	5.86	[48]	3.69	[49]
Ce	0.52	0.09	[45]	3.81	[50]
Ca	1.34	0.82	[45]	4.12	[50]
Sr	0.11	0.03	[45]	4.5	[47]

**Be possesses virtually no solid solubility in Mg beyond ppm levels*

2.4.4 The Effects of Second Phases and of Phase Change

The oxidation at the metal/oxide interface can be significantly influenced by the microstructural and phase changes that take place during heating and at high temperatures. The evolution of the microstructure includes dissolution and precipitation of the second phases, eutectic melting, and complete melting. Since each phase has a different tendency for oxidation based on the Gibbs free energy considerations, the evolution of the microstructure and the loss or the appearance of second phases significantly influence the oxidation of the alloy surface and oxide scale formation.

The multi-phase alloys also undergo selective oxidation of certain phases influencing the ignition behavior of the alloy. In some instances, the multiphase oxidation has been reported to be beneficial for oxide adherence and hence the cohesive strength of the oxide scale by creating an adherent scale at the metal/oxide interface [51]. In other cases, the disappearance of the second phase via dissolution at high temperatures has been found to be beneficial. Kim et al. [40] tested

several binary alloys under the assumption that elements with a PBR>1, such as Pr and La, might increase the ignition resistance of Mg. However, the results showed a low ignition temperature in both cases. They theorized that was attributed to the low solubility of these elements in Mg (0.14 for Pr and 0.18 wt% for La). On the other hand, elements with higher solubility limits such as Y, Gd, Dy, and Er, showed better ignition resistance when the eutectic intermetallic compounds dissolved at high temperature forming a single solid solution phase.

The adverse effect of second phases on ignition resistance was also seen in the heat treatment of Mg-Al alloys, as demonstrated by Mebarki et al. [52]. In their research, an AZ91 (Mg-Al-Zn) alloy, was tested for ignition at two different heat treatment states, to be compared with the as-cast microstructure, one solutionized at 460 °C for 24 hours and the second one artificially aged at 200 °C for 24 hours. During an isothermal holding at 520 °C used to test their ignition resistance, the aged alloy shows the earliest onset of ignition at 10 minutes. This was attributed to the existence of the $Mg_{17}Al_{12}$ second phase particles in the matrix in comparison to the single-phase solutionized state.

Eutectic melting also influences the ignition behavior of Mg alloys. In a study on AZ91D [53], the interdendritic eutectic regions of the alloy which melt during the semi-solid stage have been postulated [51] to be an essential factor in the low ignition resistance of the alloy. It was described that Mg evaporates form from the molten regions and condenses within the oxide scale pores leading to vigorous oxidation. In general, eutectic melting in Mg-Al based alloys is deemed detrimental to ignition resistance.

It must be noted that the main factor in the ignition of multiphase alloys or upon phase change is the differences in Gibbs free energy change, ΔG of oxidation from different phases that can alter the extent of MgO formation and thereby influence the ignition behavior of the alloy.

Accordingly, it is expected that the existence of second phases or change of phase may either positively or negatively influence the ignition resistance depending on ΔG values.

2.4.5 Third Element Effect

In a ternary system exposed to high-temperature oxidation, *the third element effect* occurs when the oxide stability of the third element resides between the oxide stabilities of the other two elements. In this case, the third element would be capable of lowering the oxygen activity at the metal/oxide interface, thus promoting the oxide formation at lower amounts of the element with the most stable oxide [10].

This effect can be seen in the work presented by Dunn [54], where the high-temperature oxidation behavior of a Cu-Al system in combination with Zn is analyzed. Two alloys, Cu-29 at% Zn - 4.7 At% Al and Cu-19 at% Al, are compared. The later alloy shows more weight gain, even when the aluminum content is higher. This is related to the formation of a dense Al_2O_3 layer when Zn is added to the alloy. In Fig. 2.6, the weight gain of a Cu-30 wt% Zn alloy at 850 °C for 3 hours, versus the Al aluminum addition is plotted. This behavior is discussed by Wagner [55], who states that in a Cu-Al system, a Cu_2O scale is formed and the oxygen partial pressure of the metal/oxide interface is around 0.01 at%. When the Zn is added, this concentration is $1x10^6$ times lower at the metal/oxide interface, making it virtually impossible to generate Al_2O_3 internally. Because of this, Al tends to migrate towards the surface and oxidize, thanks to its high oxygen affinity, which could reduce the existing Cu_2O and ZnO through displacement reactions. Zn could also work as an oxygen getter, preventing this element from reaching into the alloy.

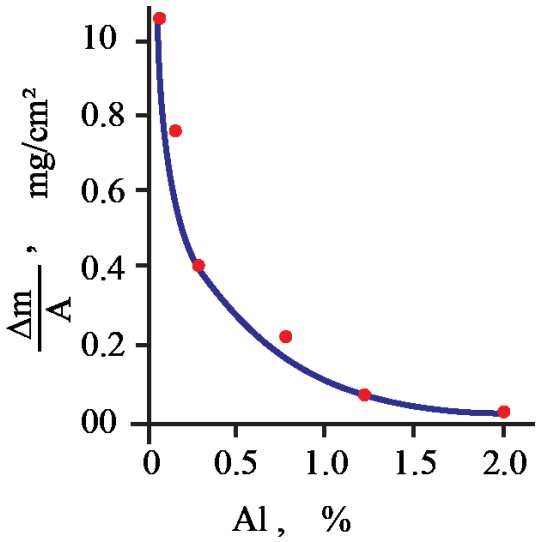

Fig. 2.6. Weight gain (mg/cm^2) of a Cu –29 wt% Zn alloy, when oxidized at 850 °C for 3 hours, versus the weight percentage of Al in the alloy. Redrawn from [54].

This effect was reported by Fan et al. [56] for the Mg-Y-Ca system where Ca plays a role as an oxide with intermediate stability (between Mg and Y). The effect translates into a reduction in the amount of Y required to increase the ignition temperature up to 900 °C (from 11 to 3.5 wt% Y) when 0.8 wt% Ca is added. The improvement was attributed to the formation of Y_2O_3 at the metal/oxide interface, which forms a continuous oxide scale. CaO was the intermediate layer which acts as an oxygen getter, preventing this element diffusion to inner layers. MgO was formed at the gas/oxide interface.

2.5 Studies on the Development of Ignition Resistant Mg Alloys

Most of the research on the development of ignition resistant alloys has been conducted during the last decade, including flammability tests, the study of oxidation kinetics and the effect of alloying elements. Consequently, we may define three main branches of work where the ignition resistance of Mg is analyzed: (1) commercial Mg alloys, (2) modified commercial Mg alloys and (3) new binary to quinary Mg alloys.

2.5.1 Commercial Alloys

Some of the other alloys used for aerospace and automotive applications (e.g., AZ91, AM50, and AZ31) contain Al, Mn, and Zn, which reduce the ignition temperature of the alloy below the ignition temperature (T_i) of pure Mg. The low ignition resistance (T_i = 580 °C) of AZ91 [57] alloy is mainly due to the lower eutectic temperature of the alloy. This could lead to the formation of liquid pools over the matrix, evidenced by the formation of cauliflower oxide morphology. This represents the breakdown of the protective oxide layer at the initial stages of ignition and Mg evaporation from the molten areas. In another study. It is known that trace levels of Be in this commercial alloy prevents burning and that Mg-Al casting alloys such as AZ91D are alloyed with ppm levels of Be [58]. A study by Tan et al. [59] tested the effect of 60 ppm Be, resulting in the formation of a fine-grained (Mg,Be)O scale, which withstood better the internal oxide stresses and Mg evaporation, resulting in a prolonged the oxidation incubation period. Contents as small as 10 ppm can delay the oxidation onset, improving a the same time the ignition resistance of Mg [60]. Alloys like AM50 exhibit also a lower T_i than alloys such as WE43, but higher than the AZ91 likely due to the existence of Zn, which may change the eutectic temperature.

Particular aerospace alloys (e.g., gearbox) such as WE43 containing Nd and Y exhibit higher T_i up to 644 °C [61]; many studies have attributed this to the to the formation of a smooth oxide scale over the surface and crack healing with Y_2O_3 [62]. Other factors, such as the surface activity of Y and its oxygen affinity should really be considered in understanding the exact mechanisms.

2.5.2 Modified Commercial Alloys

There is research made towards modifying commercial Mg alloys to improve their ignition resistance. Calcium (Ca), beryllium (Be) and rare earth elements (RE) are among the additions

most commonly used. The mechanisms proposed focuses on the ability of these elements to increase the compactness of the oxide scale and the crack healing ability of the oxide scale.

Perhaps, based on the differences in alloying and test conditions and the analysis techniques, the results are usually contradictory. Be is known to improve the burning resistance of Mg alloys [58]. Xiaoqin et al. [63] added 0.3wt% Be to AZ91 and explained the improved ignition resistance via the surface activity of Be where it enriches at the surface of the molten alloy up to ten times higher than in the bulk. They postulated that this enrichment increases the tightness of the oxide layer, preventing the diffusion of oxygen towards the alloy and thus make it possible to cast without the use of a protective atmosphere. However, other explanations have also been given: the fact that surface activity of Be can merely minimize the exothermic reaction of MgO formation [64].

Li et al. [65] proposed that 0.25 wt% Ce added to AZ91 increases T_i up to 525 °C. Further addition of this element is detrimental, as 0.45 wt% Ce reduces T_i to 507 °C that the authors attributed to the formation of $Al_{11}Ce$, which forms a depletion zone around itself where the matrix becomes vulnerable to oxidation due to its high Mg composition and forms a non-protective oxide scale. In the same work, the effect of 0.25 wt% Ce on the T_i of AM50 was also analyzed; the authors stated that due to its lower Al content, a lower amount of $Al_{11}Ce$ would form, thus increasing the T_i up to 535 °C, (slightly higher than AZ91 with the same Ce amount with T_i of 525 °C). The effect of Ce on the T_i of Mg – 9 wt% Al system was reported by Zhenghua et al. [66]. When Ce is increased up to 1.0 wt%, the T_i is increased to 720 °C that they related to the surface-active behavior of Ce in Mg. However, the above explanations seem to be plausible hypotheses rather than the results of mechanistic studies.

The AZ31 ignition resistance was improved by Lee [67] through the addition of Ca and CaO. He justifies the use of CaO as a way to overcome the difficulties that could be experienced in handling pure Ca. The results show a lower weight gain in AZ31 + 0.3 wt% Ca and 0.3 wt% CaO alloys compared to AZ31 during isothermal holding at 500 °C, were the latter displays the formation of a porous and loose oxide scale over the surface. Even with this non-protective oxide scale morphology, the T_i of AZ31 increased from 578 °C to 629 °C for AZ31 + 0.3 wt% CaO and 634 °C for 0.3 wt% Ca. It is suggested that the protective behavior of the alloy cannot be attributed to a dense protective scale due to the low PBR of 0.64 of CaO, but to the formation of CaO at low decomposition pressures (more negative ΔG), which reduces MgO formation, and hence the temperature increase due to that reaction and the eventual evaporation of Mg at the surface [67]. In another publication, Zhao et al. [68] proposed the improvement of ignition resistance of an AZ31 alloy through the addition of La and La_2O_3. The T_i increases from 520 °C to around 570 °C with the addition of 0.6 wt% of La_2O_3 and 0.55 of wt% of La. The weight gain curves at 450°C demonstrate that the lowest weight gain is achieved by the samples with 0.77 wt% La_2O_3/La addition, while further addition leads to accelerated weight gain. This detrimental effect was attributed to RE elements at higher percentages promoting the anion transport through the protective oxide scale as the rich-RE intermetallic compounds fraction increases.

The use of Y has been shown to increase the T_i of AM50 alloy by Li et al. [69] where the lowest weight gain was observed at the optimum composition of 0.28 wt% Y when the alloy was isothermally held at 450 °C for 60 minutes. The explanations given were the formation of a tight Y_2O_3 with a PBR of 1.39. The authors suggested that the adherence of the oxide scale is improved due to the formation of a continuous Al_2O_3 film at the metal/oxide interface. They also reported that if the content of Y increases beyond 0.28 wt% (e.g., 1.0 wt %) the oxygen transport through

the oxide grain boundaries increases leading to the formation of voids, local stress resulting in cracking and decreasing the adherence of the oxide to the metal.

While the mechanistic explanations are not complete, these studies indicate that there is usually an optimum level of the addition which is governed by the complex interplay of factors ranging from to the nature of the scale, the to surface activity and microstructure. The studies also show the potential effectiveness of rare earth, alkaline earth additions and Be (all surface-active in Mg) on the ignition resistance of commercial alloys.

2.5.3 New alloy development: From Binary to Quinary Systems

2.5.3.1 Binary Systems

Binary systems have been studied mainly to understand the effect of individual alloying elements on the ignition resistance of Mg. Ca was investigated by Sakamoto et al. [70], who reported that the T_i of pure Mg, increased up to 727 °C with the addition of 5 wt% Ca. At high temperatures, an oxide layer composed by MgO and CaO formed on the surface with the CaO being in the outermost layer. The increase of T_i was attributed to the reduction in the Mg vaporization. It was also suggested that the Ca on the surface could reduce the MgO at temperatures close to the melting point of the alloy.

Another alkaline earth element, Sr, has also been used to increase the T_i of Mg. In the investigation conducted by Aydin et al. [71], the T_i of Mg is increased up to 851 °C with 6 wt% of Sr that was attributed to the surface-active nature of Sr. For a bulk alloy composition of 6wt %, Sr was observed to reach 30 wt% at the surface forming an oxide layer that would reduce Mg evaporation. For the same composition, isothermal holding at 700 °C (liquid state) for 3 hours exhibited cracking in the surface. However, the Sr enriched liquid below the oxide scale continued

to form SrO at these fissures, reducing the MgO formation. The oxidation kinetics of Mg + 6 wt% Sr system is presented in another publication by Aydin et al. [72], where the weight gain of the alloy is higher than pure Mg, however the change from parabolic to linear trend is delayed significantly, meaning that the protective behavior is prolonged through the addition of Sr.

Aydin et al. [73] demonstrated that the addition of low percentages of Nd to Mg that forms dilute single-phase α-Mg(Nd) solid solution alloy where the T_i increases up to 770 °C; the formation of a Nd_2O_3 scale at the metal/oxide interface that reduces the MgO formation at the outermost layer was reported to be the main factor in the increase of ignition resistance. When the Nd percentage is increased and a two-phase alloy forms, a heterogeneous oxide scale is seen where the surface of the Nd-rich compounds is mainly covered by Nd_2O_3, while the Mg matrix is covered by a mixture of Nd_2O_3 and MgO [74]. This change leads to a change of the T_i to 766 °C with the addition of 2.5 wt% Nd. Further addition shows little effect on the ignition temperature, reaching 773 °C with 6 wt% Nd [75]. The Y addition to pure Mg has been investigated by Fan et al. [38], who reported that the T_i rises above the 900 °C with 10.6 wt% Y. However, the author suggests that the use of this amount of Y would not be economically viable due to the high cost of Y. The authors demonstrated that it is possible to take advantage of the third element effect, showing that the combined addition of 0.8 wt% Ca and 3.5 wt% Y to Mg yielded a T_i above 900°C.

2.5.3.2 Quaternary and Quinary systems

To reach an optimum combination of mechanical properties, and ignition resistance, some new quaternary and even quinary Mg systems have been developed. An example of these alloy is presented by Yu-Juan et al. [76], where the ignition temperature and the mechanical resistance of a quaternary system Mg-Gd-Ag-Zr are evaluated. The authors report an increase in the T_i to around 935 °C, due to the formation of a protective Gd_2O_3 oxide layer. The tensile strength of the alloy is

421 MPa, and the tensile yield strength is 309 MPa. Wua et al. [77] also studied the use of Gd to increase both T_i and mechanical resistance. Their alloy is a quinary Mg-Gd-Y-Zn-Zr system. The alloy was heated for 120 minutes inside a furnace at 730 °C, without noticeable ignition. This resistance is attributed to the better stability of Gd_2O_3 and Y_2O_3 oxides over the surface. The decomposition pressures of these oxides are lower than the decomposition pressure of MgO, resulting in substitution reactions that could reduce the Mg on the surface, preventing the interaction between this metal and oxygen. In other words, the formation of Gd_2O_3 and Y_2O_3 is more energetically favorable as their Gibbs energy of formation tends to be more negative when compared to MgO.

2.6 Ignition and Flammability Tests in Magnesium Alloys

In this section, the different tools, technics, and factors affecting the measurement of the ignition and flammability resistance of Mg and its alloys are presented as described in the existing literature.

2.6.1 Factors Controlling the Ignition Temperature and Measurement Approaches

The ignition temperature of Mg can be defined as the point where a white flame accompanied by a sharp increase in temperature is observed. However, ignition temperature is not an intrinsic parameter and might be modified by some experimental factors. Furthermore, it might take place even before the metal reaches the liquid state [78]. The reported ignition temperature for bulk Mg lies around 630 °C [79]. The determination of this temperature is controlled by several factors that range from the heating method to the airflow and sample geometry that can affect the temperatures measured in different studies.

The atmosphere: The atmosphere [2] was seen to have an effect of oxygen partial pressure and moisture in the burning of Mg, where it was concluded that burning time decreases up to ten times as the oxygen concentration increases from 17% to 100% and that the presence of moisture would reduce the burning time by one third with an increased moisture content. The heating rate also plays an important role. In the work presented by Derevyaga et al. [5], lower heating rates (e.g. longer lag times for ignition) decreased the ignition temperature of pure Mg from 768 °C with a lag time of 11 seconds to 650 °C when the lag time is 94 seconds, where the latter equals the melting temperature of pure Mg [80].

Heat dissipation, heating rate: The decrease of area/volume ratio of the specimen also improves the ignition resistance. Small thin-walled specimens represent a higher fire hazard in comparison to large pieces which require large amounts of heat to undergo ignition [81]. Here the thermal conductivity of the alloy is also important in conducting heat away. One extreme of the ignition risk is related to the Mg powder, which ignites at significantly lower temperatures compared to bulk samples. As defined by Khaikin et al. [82], when the oxide scale formation is the controlling factor for ignition, the dependence between particle size and ignition temperature would be inversely proportional. As an example, Mg powder with a particle size of 173 μm ignites at around 487 °C, and this temperature decreases with decreasing particle size [83]. When the particle size reaches ~ 0.3 μm, the powder will spontaneously ignite between 5 and 53 °C independent of other parameters such as oxygen concentration or ambient pressure [84]. Lui et al. [61] point out the difference between the use of an induction furnace and a resistance furnace, which could be attributed to the fact that in an induction furnace, the interior of the sample has a higher temperature compared to the surface. On the other hand, the resistance furnace increases the sample temperature from the surface to the bulk, making the scratches and edges preferential

sites for the onset of ignition due to the formation of irregular oxide scales in the solid-state, which may result in lower ignition temperatures once the alloy reaches the liquid state. If the oxidation rate is fast enough, the resulting heat from the reaction will overbalance the dissipated heat, leading to ignition [85] caused by the local vaporization of the metal. An approach where this factor is considered is presented by Takeno and Yuasa [86]. Here, the ignition temperature is measured as a function of the temperature of an air stream which heats up an Mg disk which indicated that the results are strongly time-dependent. The critical temperature for Mg ignition was established as 606 °C for which the time for ignition is the longest.

2.6.2 Determination of Magnesium Flammability

The flammability resistance could be defined as the resistance of a material to undergo combustion, in the presence of an external flame. Materials can be divided into three main categories according to its flammability resistance [87], considering they possess the dimensions required for its intended application:

- *Fireproof*: A material capable of withstanding fire as well as steel.
- *Fire-resistant:* A material capable of withstanding fire as well as aluminum alloys.
- *Flame resistant:* The material does not propagate flame after the removal of the heat source.
- *Flash resistant:* The material does not burn violently when it starts to ignite.

One of the main differences between the ignition tests and flame resistance resides in the fact that the last is considered time-dependent, which means that the sample is exposed to a flame until it ignites, compared to ignition resistance test where the temperature of self-ignition is the point of interest. However, it is essential to consider that both tests are affected by temperature and time; e.g., samples heated at a slower rate will show a reduce ignition temperature, while samples

exposed to a low-temperature flame, will show a prolonged ignition time, as both processes are governed by the oxide growth [78].

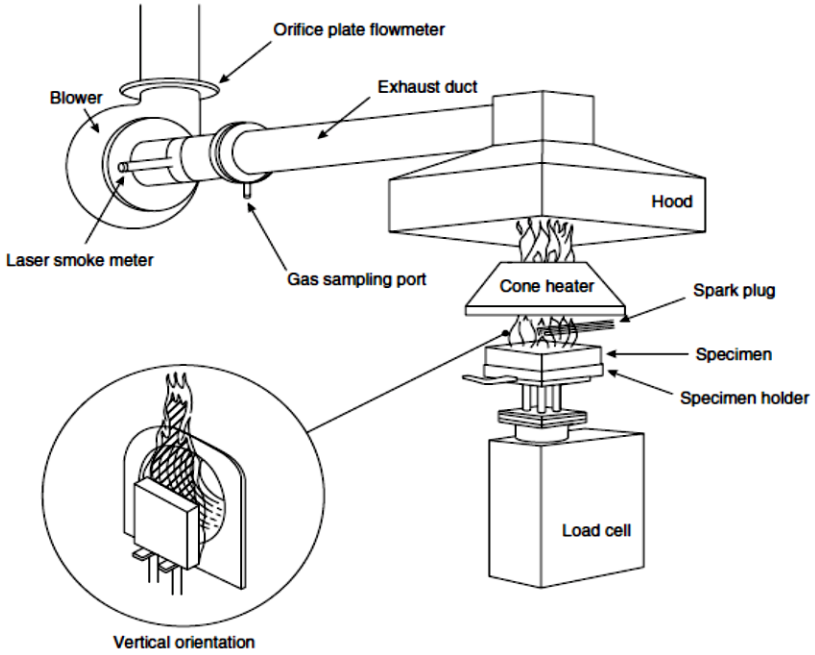

Fig. 2.7. Schematic setup of the cone calorimeter [88].

A method to determine the ignition temperature and the self-extinguishing behavior of some commercial alloys was proposed by Liu et al. [89] with the use of a cone calorimeter (Fig. 2.7) (ZE10, AZ31, and WE43). The cone calorimeter test procedure is standardized in the ASTM 1354-16 [90] and consists of the use of an electrical source of heat, which increases the temperature of the sample until it reaches its ignition point. Then, the heat released can be determined via the oxygen consumption method, as the flame and the gas flow rate are calculated by the flow that crosses an orifice plate in the exhaust duct [88]. Liu reported the ignition temperature of the samples when subjected to a radiant intensity of 65 kW/m^2, as well as the time required for the flame duration, pointing the ZE10 alloy as the one with higher ignition temperature and shorter flame time.

Specific approaches have been proposed for the measurement of magnesium flammability. An experimental setup (Fig. 2.8) to measure the flammability resistance was proposed by Prasad et al. [91], applied to determine the effect of Al and Y on pure Mg flammability and the flammability of several binary systems [92]. In their research, a magnesium rod sample is exposed to the flame of an oil burner while its temperature is measured using two thermocouples positioned at different distances from the contact point. During these tests, the time to ignition was consider along with the existence or not of detached blobs, and the time they required to cease ignition if it occurred at all.

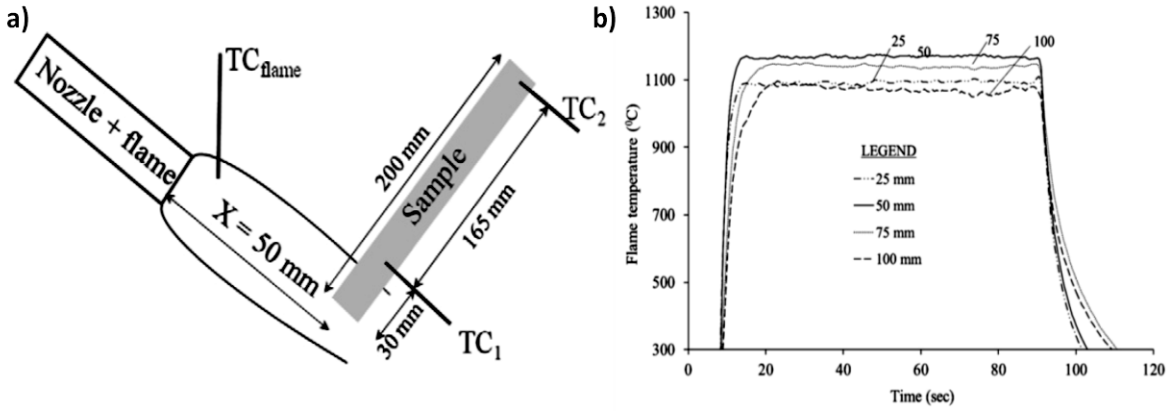

Fig. 2.8. a) Experimental setup for the measurement of flammability resistance in Mg alloys [96], (b) flame temperatures measured at different distances from the end of the nozzle.

Later, the Federal Aviation Administration (FAA), developed both laboratory and full-scale tests. The latter was developed using a 20 ft. long steel cylinder which is inserted between two halves of Boeing 707 fuselage, with an opening of 40 by 80 inches which represents a rupture in the fuselage. A square 8 by 10 ft. fuel pan was situated outside the rupture, filled with 55 gallons of JP-8 fuel and ignited to emulate a post-crash fire [93]. The schematic representation of this experimental setup is presented in Fig. 2.9a. The seat frame is exposed to flame for 5 minutes, and then it is allowed to burn for 5 additional minutes before attempting to extinguish it with water

(Fig. 2.9b). The results indicate an excellent performance of WE43 alloy, while AZ31 is qualified as poor performance material [94].

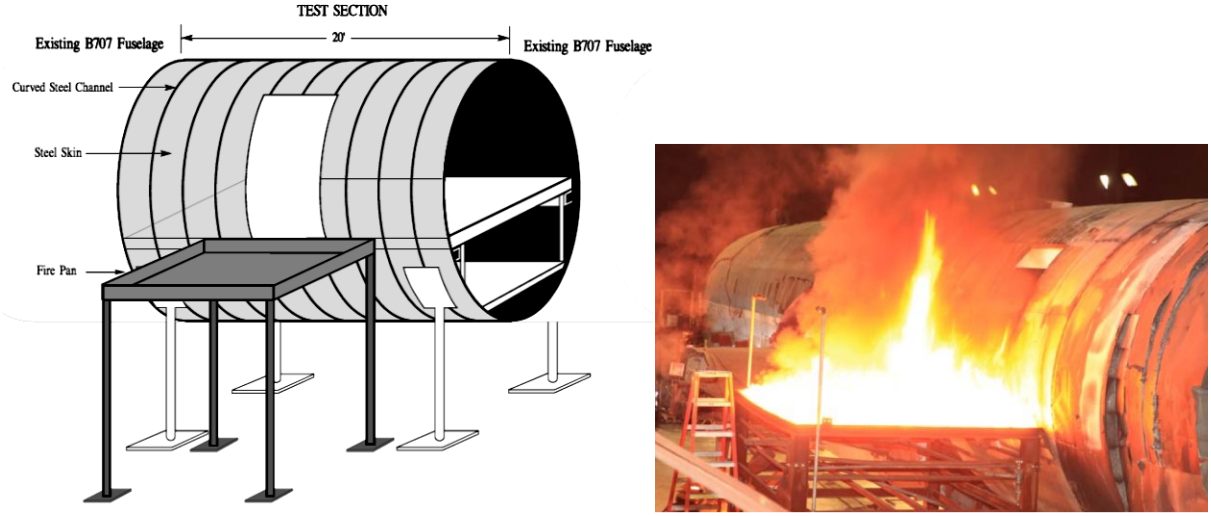

Fig. 2.9. (a) Schematic of the full-scale flammability test for magnesium alloys, where the existence of a post-crash fire entering the cabin is simulated [93]. (b) FAA full-scale tests, where an external fire can enter in contact with the cabin seats through a rupture on the fuselage [94].

To determine a wide range of scenarios where the flammability of magnesium alloys would be tested, a laboratory-scale test was also developed. The experimental setup is presented in the Aircraft Materials Fire Test Handbook [95] developed by the FAA. The chapter 25 of this handbook, describes the use of an apparatus (Fig. 2.10) composed of a gun-type burner fed by kerosene fuel type (Jet A or JP-8), which is pointed towards a plate sample of a thickness of 6.4 mm, height of 38.1 mm and 508 mm length, with one of the faces orientated horizontally at 10.2 cm from the burner cone and 2.5 cm above the burner centerline. It is required that the sample resist at least 2 minutes without ignition while losing less than 10% of its original weight.

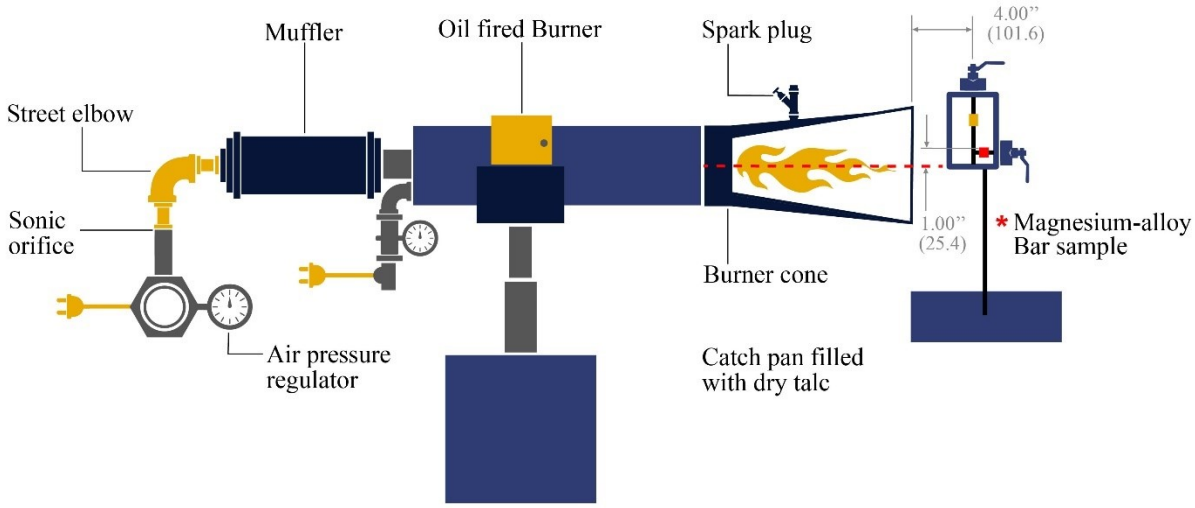

Fig. 2.10. Schematic representation of the burner and sample holder for the FAA flammability test. Redrawn from [95].

2.7 Strategy for Ignition Resistant Mg Alloy development

Considering the factors controlling Mg ignition presented in Section 2.4, certain potential elements for the development of ignition resistant Mg alloys can be selected (Table 2.2). Sr and Ca have the highest surface activity based on Wigner-Seitz Radius (Table 2.1). Ca, Y, Er, and Sc have high oxygen affinity (higher than Ce, La or Nd) as shown in Fig. 2.11; they also have high solid solubility at high temperatures (Table 2.1).

Table 2.2. Potential Elements for Improving the Ignition resistance of Mg

Surface activity (Table 2.1)	**Solid solubility (Table 2.1)**	**High Oxygen Affinity (Fig. 2.11)**
Sr, Ca, Ce, Y, Er	Er, Sc, Y, Ca	Sc, Y, Er, Ca, Ho

Many combinations of alloy chemistries can be considered based on the candidate elements shown in Table 2.2. In the present study, the strategy is to develop Mg alloys without rare earth additions. Due to its potential toxicity, Be is also not selected. The alloying elements selected are consequently Ca because it satisfies all four potential requirements shown in Table 2.2, and Sr is selected for its surface-active behavior.

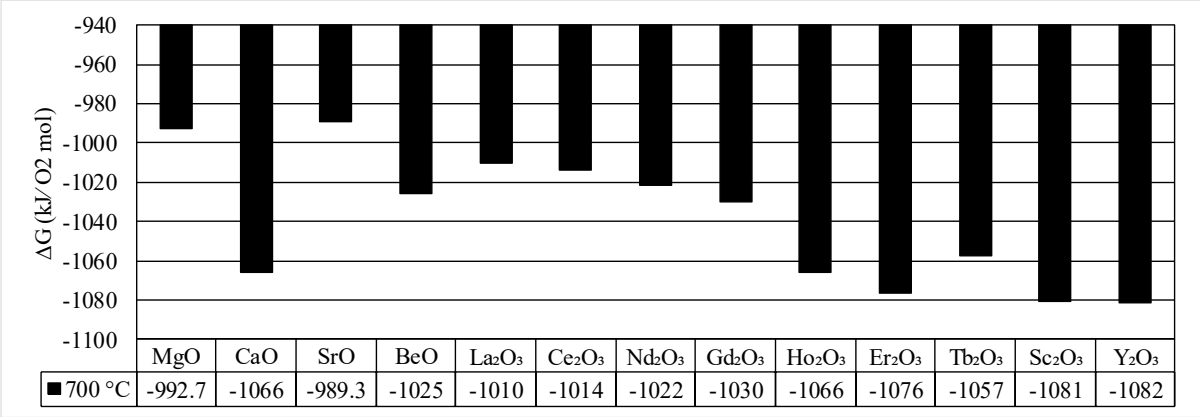

Fig. 2.11. Gibbs energy of formation for alkaline-earth and rare-earth elements at 700 °C. Elements like Y, Sc, Er, and Ho show high oxide stability. Calculated through FactSage™-FTlite database.

2.8 References for Chapter 2

[1] R. Gann and R. Friedman, Principles of Fire Behavior and Combustion. Jones & Bartlett Publishers, 2014.

[2] K. P. Coffin, "Burning times of magnesium ribbons in various atmospheres," 1954.

[3] W. M. Fassell, L. B. Gulbransen, J. R. Lewis, and J. H. Hamilton, "Ignition temperatures of magnesium and magnesium alloys," J. Met., vol. 3, no. 7, pp. 522-528, 1951.

[4] P. R. Hill and D. Adamson, "High-temperature oxidation and ignition of metals," National Aeronautics and Space Administration1956.

[5] M. Derevyaga, L. Stesik, and E. Fedorin, "Critical conditions for the ignition of magnesium," Combust., Explos. Shock Waves, vol. 14, no. 6, pp. 731-735, 1978.

[6] H. H. Uhlig, "Structure and Growth of Thin Films on Metals Exposed to Oxygen," Corros. Sci. , vol. 7, no. 325-339, 1967.

[7] M. G. Fontana, Corrosion Engineering. McGraw Hill Book Company, 1987.

[8] A. Atkinson, "Defects and diffusion in metal oxides," in Selected Topics in High Temperature Chemistry: Defect Chemistry of Solids, vol. 9, Ø. Johannesen and A. G. Andersen, Eds.: Elsevier B.V., 2017, pp. 29-54.

[9] P. Harrop, "Self-diffusion in simple oxides (a bibliography)," J. Mater. Sci., vol. 3, no. 2, pp. 206-222, 1968.

[10] D. J. Young, High Temperature Oxidation and Corrosion of Metals. Elsevier Ltd, 2008.

[11] ASM Handbook - Volume 13: Corrosion Fundamentals. USA: ASM International - The Materials Information Society, 2004.

[12] N. Cabrera and N. F. Mott, "Theory of the Oxidation of Metals," Rep. Prog. Phys., vol. 12, p. 163, 1949.

[13] D. Gilroy and J. E. O. Mayne, "The Oxidation of Iron at High Temperature," Corros. Sci., vol. 5, pp. 55-58, 1965.

[14] F. S. Petit and J. B. Wagner, "Transition from the Linear to the Parabolic Rate Law during the oxidation of iron to wüstite in CO-CO2 mixtures," Acta Metall., vol. 12, no. 35, pp. 35-40, 1964.

[15] ISO Standards Handbook: Quantities and units. 3rd edition. Geneva: International Standards Organization, 1993.

[16] D. R. Gaskell, Introduction to the Thermodynamics of Materials, 4th edition. New York: Taylor & Francis, 2003.

[17] N. Birks, G. H. Meier, and F. S. Petit, Introduction to High Temperature Oxiation. 2nd Edition. New York: Cambridge University Press, 2006.

[18] T.-S. Shih, J.-B. Liu, and P.-S. Wei, "Oxide films on magnesium and magnesium alloys," Mater. Chem. Phys., vol. 104, pp. 497–504, 2007.

[19] J. A. Van Orman and K. L. Crispin, "Diffusion in Oxides," Rev. Mineral. Geochem., vol. 72, no. 1, pp. 757-825, 2010.

[20] H. E. Friedrich and B. L. Mordike, Magnesium Technology: Metallurgy, Design Data and Applications. Berlín: Springer-Verlag, 2006.

[21] F. Czerwinski, "Oxidation characteristics of magnesium alloys," J. Met., vol. 64, no. 12, pp. 1477-1483, 2012.

[22] E. A. Gulbransen, "Kinetic and Structural Factors Involved in Oxidation of Metals," Ind. Eng. Chem., vol. 41, no. 7, pp. 1385-1391, 1949.

[23] R. R. Addiss Jr, "Oxidation of magnesium single crystals and evaporated films," Acta Metall., vol. 11, no. 2, pp. 129-135, 1963.

[24] L. Hirsch and T. Shankland, "Equilibrium point defect concentrations in MgO: Understanding the mechanisms of conduction and diffusion and the role of Fe impurities," J. Geophys. Res.: Solid Earth, vol. 96, no. B1, pp. 385-403, 1991.

[25] D. Alfe and M. Gillan, "Schottky defect formation energy in MgO calculated by diffusion Monte Carlo," Phys. Rev. B, vol. 71, no. 22, p. 220101, 2005.

[26] I. Sakaguchi, H. Yurimoto, and S. Sueno, "Self-diffusion along dislocations in single-crystals MgO," Solid State Commun., vol. 84, no. 9, pp. 889-893, 1992.

[27] I. Sakaguchi, H. Yurimoto, and S. Sueno, "Calcium Diffusion along High-Diffusivity Paths in Single-Crystal MgO," J. Am. Ceram. Soc., vol. 75, no. 3, pp. 712-715, 1992.

[28] H. Hashimoto, M. Hama, and S. i. Shirasaki, "Preferential diffusion of oxygen along grain boundaries in polycrystalline MgO," J. Appl. Phys., vol. 43, no. 11, pp. 4828-4829, 1972.

[29] C. Lea and C. Molinari, "Magnesium diffusion, surface segregation and oxidation in Al-Mg alloys," Journal of Materials Science, vol. 19, no. 7, pp. 2336-2352, 1984.

[30] E. A. Gulbransen, "The Oxidation and Evaporation of Magnesium at Temperatures from 400° to 500° C," Trans. Electrochem. Soc., vol. 87, no. 1, pp. 589-599, 1945.

[31] W. Smeltzer, "Oxidation of An Aluminum-3 Per Cent Magnesium Alloy in the Temperature Range 200°–550° C," J. Electrochem. Soc., vol. 105, no. 2, pp. 67-71, 1958.

[32] F. Czerwinski, "The reactive element effect on high-temperature oxidation of magnesium," Int. Mater. Rev., vol. 60, no. 5, pp. 264-296, 2015.

[33] B. Bobryshev and Y. P. Aleksandrova, "Ignition of magnesium and its alloys," Met. Sci. Heat Treat., vol. 30, no. 3, pp. 219-222, 1988.

[34] N. B. Pilling and R. E. Bedworth, "The Oxidation of Metals at High Temperatures," J. Inst. Met., vol. 29, no. 529, 1923.

[35] C. Xu and W. Gao, "Pilling-Bedworth ratio for oxidation of alloys," (in English), Mater. Res. Innovations, vol. 3, no. 231–235, pp. 231-235, Mar 2000.

[36] P. Roberge, Corrosion Basics: An Introduction, 2nd ed. Houston, TX: NACE International, 2006.

[37] P.-Y. Lin, H. Zhou, W.-P. Li, W. Li, S.-Z. Zhao, and J.-G. Su, "Effect of yttrium addition on the oxide scale of AM50 magnesium alloy," Corros. Sci., vol. 51, no. 1128–1133, 2009.

[38] F. Jianfeng, C. Zhiyuan, Y. Weidong, F. Shuang, and X. Bingshe, "Effect of yttrium, calcium and zirconium on ignition-proof principle and mechanical properties of magnesium alloys," J. Rare Earths, vol. 30, no. 1, 2012.

[39] Z. Na, Z. Zhang, D. Jie, J. Li, and D. Wenjiang, "Selective oxidation behavior of an ignition-proof Mg-Y-Ca-Ce alloy," J. Rare Earths, vol. 31, no. 10, pp. 1003-1008, 2013.

[40] Y. M. Kim, C. D. Yim, H. S. Kim, and B. S. You, "Key factor influencing the ignition resistance of magnesium alloys at elevated temperatures," Scr. Mater., vol. 65, no. 11, pp. 958-961, 2011.

[41] H. Yamauchi, "Surface segregation in jellium binary solid solutions," Phys. Rev. B, vol. 31, no. 12, 1984.

[42] P.-G. Reinhard and E. Suraud, Introduction to Cluster Dynamics. John Wiley & Sons, 2004.

[43] D. S. Aydin, "High Temperature Oxidation and Ignition Behaviour of Magnesium Alloys Containing Strontium (Sr) and Neodymium (Nd)," ed. Montreal, Canada, 2014.

[44] A. Nayeb-Hashemi and J. Clark, "The Be− Mg (Beryllium-Magnesium) system," Journal of Phase Equilibria, vol. 8, no. 1, pp. 57-58, 1987.

[45] ASM Handbook - Volume 3: Alloy Phase Diagrams. USA: ASM International - The Materials Information Society, 2004.

[46] F. Ren, K. Cao, J. Ren, A. A. Volinsky, T. H. Tran, and B. Tian, "Numerical Calculation of the Electron Density at the Wigner–Seitz Radius Based on the Thomas–Fermi–Dirac Equation," J. Comput. Theor. Nanosci., vol. 11, pp. 1- 4, 2014.

[47] P. Politzer, R. G. Parr, and D. R. Murphy, "Approximate determination of Wigner-Seitz radii from free-atom wave functions," Phys. Rev. B, vol. 31, no. 10, p. 6809, 1985.

[48] H. Okamoto, "Er-Mg (Erbium-Magnesium)," J. Phase Equilib., vol. 24, no. 3, p. 278, 2003.

[49] P. Strange, A. Svane, W. M. Temmerman, and Z. Szotek, "Understanding thevalency of rare earths from first-principles theory," Nature, vol. 399, pp. 756-758, 1999.

[50] J. H. Rose, J. R. Smith, F. Guinea, and J. Ferrante, "Universal features of equation of state of metals," Phys. Rev. B, vol. 29, no. 6, pp. 2963-2969, 1984.

[51] C. Giggins, B. Kear, F. Pettit, and J. Tien, "Factors affecting adhesion of oxide scales on alloys," Metall. Mater. Trans. B, vol. 5, no. 7, pp. 1685-1688, 1974.

[52] N. Mebarki, N. V. R. Kumar, J. J. Blandin, M. Suery, and F. Pelloux, "Correlation between ignition and oxidation behaviours of AZ91 magnesium alloy," Mater. Sci. Tech., vol. 21, pp. 1145-1151, 2005.

[53] F. Czerwinski, "The oxidation behaviour of an AZ91D magnesium alloy at high temperatures," Acta Mater., vol. 50, no. 10, pp. 2639-2654, 2002.

[54] J. S. Dunn, "The oxidation of some copper alloys," J. Inst. Met., vol. 46, pp. 25-48, 1931.

[55] C. Wagner, "Passivity and Inhibition during the Oxidation of Metals at Elevated Temperatures," Corros. Sci., vol. 5, no. 751-764, 1965.

[56] J. F. Fan, G. C. Yang, Y. H. Zhou, Y. H. Wei, and B. S. Xu, "Selective Oxidation and the Third-Element Effect on the Oxidation of Mg-Y Alloys at High Temperatures," Metall. Mater. Trans. A, vol. 40, no. 2184, 2009.

[57] N. R. Kumar, J. Blandin, M. Suery, and E. Grosjean, "Effect of alloying elements on the ignition resistance of magnesium alloys," Scr. Mater., vol. 49, no. 3, pp. 225-230, 2003.

[58] M. O. Pekguleryuz, K. Kainer, and A. A. Kaya, Fundamentals of magnesium alloy metallurgy. Elsevier, 2013.

[59] Q. Tan et al., "Improved oxidation resistance of Mg-9Al-1Zn alloy microalloyed with 60 wt ppm Be attributed to the formation of a more protective (Mg, Be) O surface oxide," Corros. Sci., vol. 132, pp. 272-283, 2018.

[60] F. Czerwinski, "The early stage oxidation and evaporation of Mg–9%Al–1%Zn alloy," Corros. Sci., vol. 46, no. 377–386, 2004.

[61] M. Liu, D. S. Shih, C. Parish, and A. Atrens, "The ignition temperature of Mg alloys WE43, AZ31 and AZ91," Corros. Sci., vol. 54, no. 139–142, 2012.

[62] N. V. R. Kumar, J. J. Blandin, M. Suery, and E. Grosjean, "Effect of alloying elements on the ignition resistance," Scr. Mater., vol. 49, pp. 225–230, 2003.

[63] Z. Xiaoqin, W. Qudong, L. Yizhen, Z. Yanping, D. Wenjiang, and Z. Yunhu, "Influence of beryllium and rare earth additions on ignition-proof magnesium alloys," J. Mater. Process. Technol., vol. 112, pp. 17-23, 2001.

[64] Y.-B. Huang, I.-S. Chung, B.-S. You, W.-W. Park, and B.-H. Choi, "Effect of Be Addition on the Oxidation Behavior of Mg-Ca Alloys at Elevated Temperature," Met. Mater. Int., vol. 10, no. 1, pp. 7-11, 2004.

[65] P.-y. Lin, H. Zhou, W. Li, W.-p. Li, N. Sun, and R. Yang, "Interactive effect of cerium and aluminum on the ignition point and the oxidation resistance of magnesium alloy," Corros. Sci., vol. 50, no. 9, pp. 2669-2675, 2008.

[66] Z. Deng, H. Li, W. Zhao, and W. Li, "Effects of Ce concentrations on ignition temperature and surface tension of Mg-9wt.%Al," China Foundry, vol. 10, no. 2, pp. 108-111, 2013.

[67] D. B. Lee, "High temperature oxidation of AZ31 + 0.3 wt.%Ca and AZ31 + 0.3 wt.%CaO magnesium alloys," Corros. Sci., vol. 70, no. 243–251, 2013.

[68] S. Zhao, H. Zhou, T. Zhou, Z. Zhang, P. Lin, and L. Ren, "The oxidation resistance and ignition temperature of AZ31 magnesium alloy with additions of La2O3 and La," Corros. Sci., vol. 67, pp. 75-81, 2013.

[69] P. y. Lin, H. Zhou, W.-p. Li, W. Li, S.-z. Zhao, and J.-g. Su, "Effect of yttrium addition on the oxide scale of AM50 magnesium alloy," Corr. Sci., vol. 51, pp. 1128–1133, 2009.

[70] M. Sakamoto, S. Akiyama, and K. Ogi, "Suppression of ignition and burning of molten Mg alloys by Ca bearing stable oxide film," J. Mater. Sci. Lett., vol. 16, no. 1048-1050, 1997.

[71] D. S. Aydin, Z. Bayindir, and M. O. Pekguleryuz, "The effect of strontium (Sr) on the ignition temperature of magnesium (Mg): a look at the pre-ignition stage of Mg–6 wt% Sr," J. Mater. Sci., vol. 48, no. 23, pp. 8117-8132, 2013.

[72] D. S. Aydin, B. Zeynel, and M. O. Pekguleryuz, "High Temperature Oxidation Behavior of Hypoeutectic Mg–Sr Binary Alloys: The Role of the Two-Phase Microstructure and the Surface Activity of Sr," Adv. Eng. Mater., vol. 17, no. 5, pp. 697-708, 2014.

[73] D. S. Aydin, Z. Bayindir, M. Hoseini, and M. O. Pekguleryuz, "The high temperature oxidation and ignition behavior of Mg–Nd alloys part I: The oxidation of dilute alloys," J. Alloys Compd., vol. 569, no. 35–44, 2013.

[74] D. S. Aydin, Z. Bayindir, and M. O. Pekguleryuz, "The high temperature oxidation behavior of Mg–Nd alloys. Part II: The effect of the two-phase microstructure on the on-set of oxidation and on oxide morphology," J. Alloys Compd., vol. 584, no. 558–565, 2014.

[75] D. S. Aydin, M. Hoseini, and M. O. Pekguleryuz, "Understanding the high temperature oxidation and ignition behaviour of two-phase Mg–Nd alloys and a comparison to single phase Mg–Nd," Philos. Mag., vol. 95, no. 3, pp. 259-274, 2015.

[76] W. Yu-juan, P. Li-ming, Z. Su, L. De-jiang, H. Fei, and D. Wen-jiang, "Ignition-Proof Properties of a High-Strength Mg-Gd-Ag-Zr Alloy," J. Shanghai Jiaotong Univ., vol. 17, pp. 643-647, 2012.

[77] L. Wua and Z. Yang, "Oxidation behaviour of Mg–2.1Gd–1.1Y–0.82Zn–0.11Zr alloy at high temperatures," J. Alloys Compd., vol. 626, pp. 194-202, 2015.

[78] F. Czerwinski, "Controlling the ignition and flammability of magnesium for aerospace applications," Corros. Sci., vol. 86, pp. 1-16, 2014.

[79] N. V. R. Kumar, J. J. Blandin, M. Suery, and E. Grosjean, "Effect of alloying elements on the ignition resistance," Scr. Mater., vol. 49, no. 225–230, 2003.

[80] A. I. H. Committee, Properties and selection: nonferrous alloys and special-purpose materials. Asm Intl, 1990.

[81] P. Boris, "A Study of the Famability of Magnesium," Federal Aviation Agency, Washington, D.C.1964, Available: http://www.dtic.mil/dtic/tr/fulltext/u2/644408.pdf.

[82] B. Khaikin, V. Bloshenko, and A. G. Merzhanov, "On the ignition of metal particles," Combust., Explos. Shock Waves, vol. 6, no. 4, pp. 412-422, 1970.

[83] Y. Chunmiao, H. Dezheng, L. Changc, and L. Gang, "Ignition behavior of magnesium powder layers on a plate heated at constant temperature," J. Hazard. Mater., vol. 246-247, no. 283-290, 2013.

[84] S. Yuasa, M. Kawashima, and T. Sakurai, "Spontaneous ignition of ultra-fine magnesium powder without an original oxide coat at room temperature in O2/N2 mixture streams," Proc. Combust. Inst., vol. 32, no. 1929–1936, 2009.

[85] P. R. Hill, D. Adamson, D. H. Foland, and W. E. Bressette, "High Temperature Oxidation and Ignition of Metals," National Advisory Comitee for Aeronautics, Washington1956.

[86] T. Takeno and S. Yuasa, "Ignition of Magnesium and Magnesium-Aluminum Alloy by Impinging Hot-Air Stream," Combust. Sci. Technol., vol. 21, no. 109-121, 1980.

[87] "Cabin Interior & Cargo Compartment Flammability," Airworthiness Bulletin2011.

[88] V. Babrauskas, "The Cone Calorimeter," in SFPE Handbook of Fire Protection Engineering, Fifth Edition: Springer, 2016.

[89] C. Liu, S. Lu, Y. Fu, and H. Zhang, "Flammability and the oxidation kinetics of the magnesium alloys AZ31, WE43, and ZE10," Corros. Sci., vol. 100, no. 177–185, 2015.

[90] "ASTM E1354-16 - Standard Test Method for Heat and Visible Smoke Release Rates for Materials and Products Using an Oxygen Consumption Calorimeter," ASTM International, West Conshohocken, PA2016.

[91] A. Prasad, Z. Shi, and A. Atrens, "Influence of Al and Y on the ignition and flammability of Mg alloys," Corros. Sci., vol. 55, no. 153–163, 2012.

[92] A. Prasad, Z. Shi, and A. Atrens, "Flammability of Mg–X Binary Alloys," Adv. Eng. Mater., vol. 14, no. 9, pp. 772-784, 2012.

[93] T. R. Marker, "DOT/FAA/TC-13/52 - Development of a Laboratory-Scale Flammability Test for Magnesium Alloys Used in Aircraft Seat Construction," Federal Aviation Administration, New Jersey2014.

[94] T. Marker, "FAA Overview on Testing of Magnesium Alloys for Use in an Aircraft Cabin," Atlantic City, October 27, 2010: FAA 6th Triennial Cabin and Fire Safety Conference.

[95] "Aircraft Materials Fire Test Handbook," ed. [99] T. Marker, "FAA Overview on Testing of Magnesium Alloys for Use in an Aircraft Cabin," Atlantic City, October 27, 2010: FAA 6th Triennial Cabin and Fire Safety Conference.

Chapter 3 - Experimental Methods

In this chapter, the experimental procedures followed to obtain the results presented in this thesis are described. The casting process followed to synthesize the samples is presented in section 3.1, the ignition temperature setup is shown in Section 3.2, Section 3.3 shows an overall description of the characterization techniques used, and finally, Section 3.4 addresses possible sources of error.

3.1 Casting Process

The samples were produced via a permanent mold casting process, using a Norax induction furnace (20 kW/5 kHz) to melt Mg at 690 °C under a protective SF_6/CO_2 protective atmosphere and a graphite crucible to contain the melt (Fig. 3.1). The mold used for the casting was constructed in H13 tool steel and was coated with a boron nitride solution.

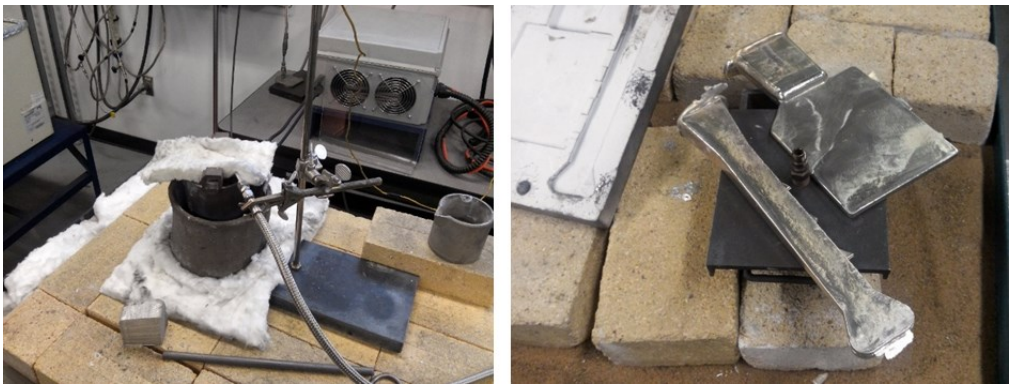

Fig, 3.1. To the left, the casting process using the Norax induction furnace and the protective CO_2/SF_6 atmosphere. To the right, the spruce and plate specimens at the end of the process.

Alloying additions to be made into a pure Mg initial charge were calculated to make a total charge of between 500 and 600 grams. Pure Mg (99.5% purity). was supplied by Magnesium Elektron Limited; pure Sr was provided by Timinco Metals LTD and Ca was added using a Mg-30 wt% Ca master alloy provided by Timinco Metals LTD. Recovery rates of 85 % for Sr and 80 % for Ca were considered to compensate for the additional losses during the casting process.

Pure Mg was placed in the graphite crucible and heated at 690 °C until molten; the slag was removed from the surface and the alloying elements were added to the melt, stirring vigorously to attain adequate mixing. The melt was held for 15 minutes to achieve a proper incorporation, and then the slag was removed again. The temperature of the melt was raised to 715 °C prior to casting into the steel permanent mold which was preheated at 400 °C using an SPX Blue M Electric Mechanical Convection Furnace and sealed using steel clamps. The casting piece was composed of a plate 6 mm thickness, a sprue, and a riser, as presented in Fig. 3.1.

3.2 Continuous Heating Test: Determination of Ignition Temperature and Interrupted Heating Tests

Coupon samples of 15 x 15 x 6 mm were machined from the plate castings for the ignition tests. The samples were ground with 800 grit SiC paper on all the faces. The samples for the interrupted ignition tests were also polished on their wide face down to 0.05 μm with colloidal silica to prepare the surface for microscopic characterization. A hole of 1.98 mm (5/64 inches) in diameter was drilled in one of the narrower faces to attach a K-type thermocouple covered with a 316L stainless steel sleeve (required to protect the thermocouple at ignition). The thermocouple was used to measure the temperature at the center of the sample. The temperature changes were recorded using a Grant Squirrel data logger (2020 series).

For complete ignition tests, the samples were placed in a Lindberg Blue vertical resistance furnace and heated continuously at two different rates of 25°C/ min (Low Heating Rate – LHR) and 45°C/ min (High Heating Rate – HHR) under a constant flow of extra dry air at a rate of 0.9 L/min. For the experiments on the Mg-Sr-Ca system (Chapter 4), only the HHR rate was used in the ignition tests. The FAA test presented in Section 2.6.2, suggest that samples are exposed to a very high heating rate. To correlate this to the ignition test presented in this work, we can assume that a sample could potentially comply with FAA standards by reaching an ignition temperature of ~750 °C using an HHR which is the temperature of the WE43 alloy, as previously mentioned in Table 1.1. This alloy is deemed as flammable-resistant by the FAA. The experimental set up is shown schematically in Fig. 3.2.

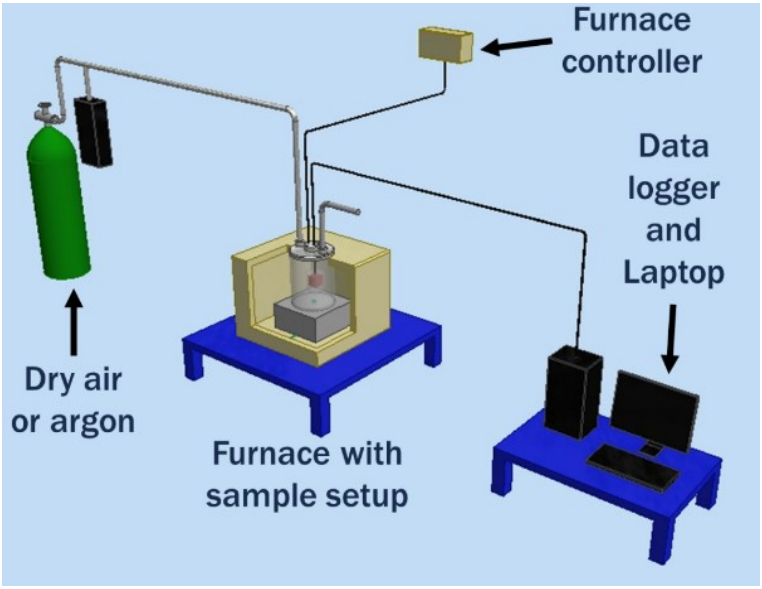

Fig. 3.1. Ignition temperature/interrupted ignition test setup.

During ignition tests, the temperature was increased continuously using a target temperature of 1150 °C. The test was stopped when a sharp increase of temperature was observed, that was identified when a change of more than 5 ºC was detected between an interval of 2 seconds. Usually, once Mg reaches ignition, the detected temperature can increase up to 1200 °C.

For the interrupted ignition tests, the samples were marked using a Vickers micro-hardness tester in the as-cast state so that the evolution of the oxide formation and microstructural change could be monitored. The samples were heated under identical conditions; however, once the target temperature of the interrupted test was reached, the furnace chamber was flushed with Ar to quickly reduce the sample temperature and finally remove it from the furnace. For the samples in Chapter 4, ignition tests were performed 3 times for each sample. For chapters 5 and 7, ignition tests were repeated twice to confirm the observed results over the composition range of the alloys tested.

3.3 Sample Characterization

Several characterization techniques were used to investigate the underlying mechanisms behind the ignition of the Mg alloys. Chemical analysis of the alloys was obtained via Inductive Coupled Argon Plasma, and Atomic Emission Spectroscopy (ICAP-AES) conducted by the NADCAP certified laboratory Genitest Inc. The ICAP-AES technique requires the digestion of Mg chips into an acid solution to dissolve them and then vaporize them using a plasma torch. This transforms the solution into excited atoms and ions in the gaseous state, which emit photons as a relaxation effect to return to the ground state. The characteristic wavelength of these photons is detected by the instrument, and their detection frequency is then used to determine their concentration in the dissolved material [1].

3.3.1 X-Ray Diffraction (XRD)

XRD was used to determine the intermetallic compounds in the as-cast alloy samples. The samples were placed inside an X-ray Bruker diffractometer equipped with a Cu Kα radiation source of λ= 1.54060 Å; between 15º and 110º for 2θ. The phase-detection through XRD in the materials analyzed in this work is limited by two important factors. First, the phase volume fraction

present in the material must be above 3% to be properly detected. Hence the presence of smaller volume fraction phases present in the material becomes virtually impossible using this technique. This drawback can be overcome using a Transmission Electron Microscope (TEM) and then perform Selected Area Diffraction (SAED), which will be further explained in Section 3.3.3. Second, the signal detected by XRD come from a volume within the hundreds of micrometers from the surface of the material. This becomes a limitation for the analysis of thin oxide films, which are typically in the order of a few micrometers or less. This can be solved by using Grazing Incidence X-Ray Diffraction (GIXRD), which consist in analyzing the sample using a low glancing angle (lower than 10°), which will result in information being collected from a region closer to the surface due to the modification of the Bragg-Brentano geometry [2].

3.3.2 Scanning Electron Microscopy (SEM)

The oxidized top surfaces were analyzed using a Hitachi SU-3500 Scanning Electron Microscope equipped with Energy Dispersive X-ray Spectroscopy (SEM/EDS). A Backscattered Electron (BSE) detector was used to analyze the microstructural features of the samples in the as-cast state and after the high-temperature oxidation processes (interrupted ignition tests and isothermal holdings). An accelerating voltage of 15 kV was used for general observation except for the cases where overlapping features would make the observation difficult, in which case an acceleration voltage of 10 kV would be used. However, as in XRD, the analysis of thin oxides composition may become difficult when an EDS detector is used due to the mixed signal coming from the large interaction volume caused by the electron beam interacting with the sample. The EDS analysis is still helpful to analyze some features in a longitudinal direction to the surface, however, for a more detailed compositional analysis in the transversal direction, X-ray Photoelectron Spectroscopy (XPS) was employed, as described in Section 3.3.4.

The use of a higher resolution SEM was required for certain analyses when extraction of phases for TEM analysis was required. A Helios Nanolab 660 Dual-beam (H660) equipped with Focused Ion Beam (FIB) was used for this purpose, which uses Ga as liquid metal ion source. The microstructural features were identified by using a Secondary Electrons (SE) detector prior to extracting the samples. The sample containing the phase of interest was further analyzed using Transmission Electron Microscope (TEM) (Fig. 3.3).

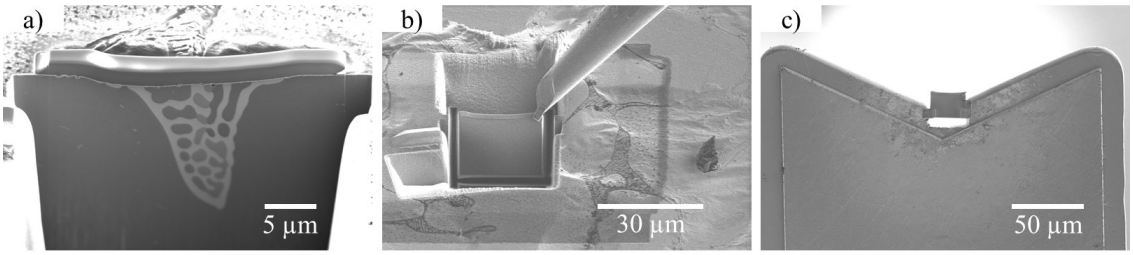

Fig. 3.2. (a) Secondary phase to be extracted from a Mg-3 Ca alloy using a tip (b) to extract it after the ion beam separates it from the bulk alloy. The sample is then placed in a TEM holder (c) for further analysis.

3.3.3 Transmission Electron Microscopy (TEM) and Scanning Transmission Electron Microscopy (STEM)

A FEI Tecnai G^2 F20 200 kV Cryo-Scanning Transmission Electron Microscope (TEM) was used to investigate features that could not be resolved with the Hitachi SU-3500 SEM. Both Scanning Transmission Electron Microscopy (STEM) and Selective Area Electron Diffraction (SAED) modes were employed. The STEM with EDS mapping mode was used to determine the composition of the oxide scales covering the samples after oxidation tests. The SAED diffraction patterns enabled the determination of the crystal structure and nature of the phase of interest. The patterns obtained were then compared to simulated patterns obtained from the PDF-4+ 2018

diffraction database, making sure that d-spacings, R ratios, and angles corresponding to the pattern observed. The results were confirmed through the CrysTBox-diffractGUI software [3].

3.3.4 X-ray Photoelectron Spectroscopy (XPS)

XPS is a tool that allows the analysis of very thin films, as the depth of analysis is about 10 nm. This advantage makes XPS a valuable tool for the analysis of oxidized surfaces and the creation of composition profiles through the sample.

The basic principle of XPS consists in the use of an X-ray source directed towards a sample, which can be obtained from either a Mg or Al target, to cause a photoemission effect on the surface atoms of a sample. The instrument measures the kinetic energy of the photo-emitted electrons, which is then used to calculate the binding energy of a given element, which will be independent of the X-ray source employed. This binding energy (BE) is determined by the following equation [4]:

$$BE = hv - E_k - W,$$

where hv is the photon energy, $E_k$is the kinetic energy of the photon emitted electron and W is the instrument work function. This excitation will generate a variety of signals [5], but the following are of main interest in the present work:

1. Photoelectron peaks: Peaks resulting from the photoemission process, which are the most intense observed lines in the spectra.
2. Auger peaks: Peaks arising from the Auger photo-emission, which is the result of a vacancy at an inner electron shell, resulting in a relaxation effect where an electron from a higher shell moves to that level, causing the emission of an electron form its former shell.
3. Multiple splitting: Peaks observed in elements with unpaired electrons in the valence band, resulting in two possible states arising from the splitting of the orbital.

An important feature of XPS is the possibility of determining the chemical state of a given element (i.e., Mg, $MgCO_3$, MgO) through an observed chemical shift on its binding energy. In this work, reported values for Mg [6, 7], Ca [8-10], and Sr [8-13] were used to determine the chemical state of each element when required.

The equipment used in this study was a Thermo Electron ESCA 2000 XPS, with an Al Kα (1438 eV) source and a spot size of 400 μm. Pass energy of 200 eV and a step size of 1 eV were used to determine the chemical composition of the oxide scale (also known as survey spectra), while a high-resolution scanning spectrum was collected using a pass energy of 50 eV and a step size of 0.1 eV to perform high-resolution scans. For each state, a single profile was obtained due to the lengthy process of first detecting the metal oxide interface and then adjust the analysis depth to a representative range. The analyzed area, however, is large and hence representative of the surface characteristics of each sample.

A compositional depth profile of the surface was obtained by gradually removing layers of the surface via an Ar ion beam, with a rate of 0.68 nm/second when Ta_2O_5 is etched, which is the reference material of the instrument for the removal process. The compounds present in our oxide scales have a lower hardness than Ta_2O_5. Hence the actual depth might be larger. The samples were etched until a Mg metallic component was detected at the deepest etching levels. The detection of the Mg metallic component allows the determination of an approximate position for the oxide/metal interface, considering that oxygen would always be present during the analysis despite the etching, due to the low decomposition pressure of Mg, Ca and Sr. The Mg KLL region was collected to determine the depth where the Mg photoemission occurs in both metal and oxide states, i.e., an approximate region of the metal/oxide interface. The use of the Mg KLL peaks ensures the detection of the metallic component without the need for peak deconvolution due to

the large chemical shift observed in Mg Auger transitions. The data was analyzed using the Advantage -Thermo Fisher Scientific software. In case of charging, the spectra were corrected by aligning the binding energy scale with the C1s elemental peak (285 eV). In case the C signal was too low at deeper etching levels, the position of the metallic Mg substrate peak would be aligned at 49.6 eV.

3.4 Sources of Error

The initial possible source of error in the ignition test is the furnace employed. Most of the ignition temperatures reported in the literature were measured through continuous heating tests, but the method used to heat the sample can lead to different outcomes. Lui et al. [14] point out the difference between the use of an induction furnace and a resistance furnace. In an induction furnace, the interior of the sample has a higher temperature compared to the surface, while a resistance furnace increases the sample temperature from the surface to the bulk. It is inferred that the scratches and edges become preferential sites for the onset of ignition due to the irregular oxide film formed, resulting in lower ignition temperatures. In this work, a resistance furnace was used, as explained in Section 3.2. To avoid the influence of surface finishing in the full ignition tests, all samples were ground down to an 800-grit paper finishing on the six faces right before the ignition test was conducted.

Another source of error comes from the attachment of the thermocouple of the sample. The hole where the thermocouple is attached must be consistently at the middle of the sample body, which is close to 7.5 mm from one of the narrow faces surface. Otherwise, the thermocouple could move if the hole is too shallow once the sample reaches the liquid state, resulting in either a false temperature reading or an early ignition due to the breakage of the covering oxide scale.

Particularly in XPS, the work with reactive metals such as Mg, Ca, and Sr would result in complications during the analysis. This is because of the high oxygen affinity of these elements; the sample surface oxidizes even inside the test chamber between etching steps (during the analysis stage) when a depth profile is performed. The vacuum inside the chamber is around ~$1x10^{-8}$ bar, which is not enough to prevent completely Mg, Ca or Sr oxidation. Hence, it was important to perform the collection only of the peaks of main interest for each test, avoiding excessive delays between etching steps. Another problem encountered in XPS analysis was the differential charging through the oxide scale. Despite the use of a flood gun, there was a displacement of ~-0.45 eV in the depth profile spectra. However, this displacement sometimes would not be the same for every oxide layer in the same sample. This required a detailed charging analysis of every layer if a high-resolution spectra deconvolution was required.

The quantification of Ca present in the alloy surface required special considerations. The Ca2p doublet peaks usually collected interfere with the Mg KLL Auger region in the range between 360 and 344 eV, leading to complications for both compositional analysis and chemical state assessment. Hence, the Ca2s peak was considered for the compositional analysis, using a relative sensitivity factor (RSF) of 2.106 to determine an approximate amount of Ca present in the surface. The Ca2s peak was collected using a high-resolution scan to confirm the chemical state of this element.

3.5 References for Chapter 3

[1] X. Hou, R. S. Amais, B. T. Jones, and G. L. Donaty, "Inductively Coupled Plasma Optical Emission Spectrometry," in Encyclopedia of Analytical Chemistry, 2016, pp. 1-25.

[2] M. Bouroushian and T. Kosanovic, "Characterization of thin films by low incidence X-ray diffraction," Cryst. Struct. Theory Appl, vol. 1, no. 3, pp. 35-39, 2012.

[3] M. Klinger, "More features, more tools, more CrysTBox," J. Appl. Crystallogr., vol. 50, no. 4, 2017, doi: https://doi.org/10.1107/S1600576717006793.

[4] J. F. Watts and J. Wolstenholme, "An introduction to surface analysis by XPS and AES", Wiley-VCH, May 2003., p. 224, 2003.

[5] J. F. Moulder, W. F. Stickle, P. E. Sobol, and K. D. Bomben, Handbook of X-ray photoelectron spectroscopy: a reference book of standard spectra for identification and interpretation of XPS data. Eden Prairie, MN: Physical Electronics, 1995.

[6] V. Fournier, P. Marcus, and I. Olefjord, "Oxidation of magnesium," Surf. Interface Anal., vol. 34, no. 1, pp. 494-497, 2002.

[7] S. Ardizzone, C. Bianchi, M. Fadoni, and B. Vercelli, "Magnesium salts and oxide: an XPS overview," Appl. Surf. Sci., vol. 119, no. 3-4, pp. 253-259, 1997.

[8] J.-C. Dupin, D. Gonbeau, P. Vinatier, and A. Levasseur, "Systematic XPS studies of metal oxides, hydroxides and peroxides," Phys. Chem. Chem. Phys., vol. 2, no. 6, pp. 1319-1324, 2000.

[9] H. v. Doveren and J. T. Verhoeven, "XPS spectra of Ca, Sr, Ba and their oxides," J. Electron Spectrosc. Relat. Phenom., vol. 21, no. 3, pp. 265-273, 1980.

[10] M. Sosulnikov and Y. A. Teterin, "X-ray photoelectron studies of Ca, Sr and Ba and their oxides and carbonates," J. Electron Spectrosc. Relat. Phenom., vol. 59, no. 2, pp. 111-126, 1992.

[11] R. P. Vasquez, "SrCO3 by XPS," Surf. Sci. Spectra, vol. 1, no. 1, pp. 112-116, 1992.

[12] V. Young and T. Otagawa, "XPS studies on strontium compounds," Appl. Surf. Sci., vol. 20, no. 3, pp. 228-248, 1985.

[13] R. Vasquez, "X-ray photoelectron spectroscopy study of Sr and Ba compounds," J. Electron Spectrosc. Relat. Phenom., vol. 56, no. 3, pp. 217-240, 1991.

[14] M. Liu, D. S. Shih, C. Parish, and A. Atrens, "The ignition temperature of Mg alloys WE43, AZ31 and AZ91," Corros. Sci., vol. 54, pp. 139–142, 2012.

Chapter 4 - The Ignition Behavior of a Ternary Mg-Ca-Sr Alloy

In this Chapter, an initial approach to develop ignition resistant Mg-Sr-Ca alloys is presented. As mentioned in Section 2.7, both Sr and Ca are elements that have desirable characteristics to increase the igntion resistance of Mg, with the additional advantage of avoiding the use of rare-earth elements present in current commercial igntion-resistant alloys such as WE43 or EZ21. The proposed additions made are 2.5 wt% Sr and 1.0 wt% Ca according to criteria explained in section 4.1.

This paper was published in "Villegas-Armenta, L.A. and Pekguleryuz, M.O. (2020), The Ignition Behavior of a Ternary Mg–Sr–Ca Alloy. Adv. Eng. Mater.. doi:10.1002/adem.201901318".

Abstract

In this work, a Mg–Sr–Ca alloy is evaluated for ignition resistance. The simultaneous use of Sr and Ca results in an ignition temperature increase of 110 °C compared to pure Mg. This is attributed to the formation of a compact oxide scale due to the modification of the native MgO scale. A new parameter, the effective Pilling–Bedworth ratio (EPBR), which is the molar volume ratio between the oxide formed and the substrate alloy, is developed. The EPBR of the composite oxide forming on the Mg–Ca–Sr alloy is found to be greater than 1, resulting in a protective scale due to the increased volume occupied by the oxide at the surface. In the solid state, the oxide scale is rich in CaO, with the SrO contribution being minimal. In the liquid state, SrO contribution increases.

4.1 Introduction

The use of Mg alloys for cabin components in commercial aircraft represents an option to decrease the overall weight of the airplane to reduce fuel consumption. However, the flammability of Mg has been an impediment to its wide usage. The MgO formed on the surface is loose and porous [1] and cannot prevent further contact between oxygen and Mg after the initial oxidation stage. It is reported that the local heating produced by the oxidation reaction would vaporize Mg, due to its high vapor pressure [2,3]. The eventual interaction between oxygen and Mg gas would result in ignition [4], consuming the metal with an intense white flame [5]. The main concern for the use of Mg components in civilian aircraft is the risk of fire in a postcrash scenario. The presence of fire dramatically reduces the survival probability of the passengers. The Federal Aviation Administration (FAA) report “Evaluating the Flammability of Various Magnesium Alloys During Laboratory and Full-Scale Aircraft Fire Tests DOT/FAA/AR-11/3” describes a full-scale flammability experiment [6]. Commercial alloys such as AZ91 and AM50 have even lower

ignition temperatures than pure Mg, and their use would mean an increased risk of postcrash fire [6] as the addition of Al and Zn reduces the ignition resistance of Mg [7]. The ignition resistance of Mg is considered to be composition dependent [8], as the addition of different alkaline earth (AE) and rare earth (RE) elements increases the ignition resistance of Mg and its alloys [9]. Mg has a higher oxygen affinity than other metals such as Fe and Al and, therefore, it would be oxidized preferentially, resulting in the formation of a porous MgO scale [10]. The use of high-oxygen-affinity elements can reduce the interaction of Mg with oxygen, through their selective oxidation, forming a compact oxide scale or the reduction of MgO formed; for example, Ca partially reduces MgO due to its particularly high oxygen affinity, creating a more compact oxide scale [11]. There are several other factors involved in selecting alloying elements to improve the ignition resistance of Mg [12,13], such as matrix solubility, oxygen affinity, and oxide characteristics. It has been suggested [14,15] that the use of alloying elements that have an oxide with a Pilling–Bedworth ratio (PBR) higher than 1 creates a protective oxide scale on the alloy and therefore increases the magnesium ignition resistance. The PBR represents a ratio between oxide molar volume over the pure metal molar volume [16]. In the case of alloys, this value can be affected by both crystal structure and lattice constants, where differences between the characteristics of the pure metal and the alloy would lead to a significant difference in PBR [17]. Another approach is the use of surface-active elements to reduce the amount of Mg available for oxidation on the surface. Yamauchi [18], through a density functional theory approach, stated that the Wigner–Seitz (WS) radius of an element predicts the surface-active behavior of the element in an alloy. A solute element with a WS radius larger than that of the solvent would be surface active. In the case of Mg, elements such as Y (3.78),[19] Ce (3.81),[20] Be (3.92),[21] Ca (4.12),[22] and Sr (4.5)[23] would be surface active due to their larger WS radius compared with that of Mg (2.66)

[21]. Recent years have seen several studies devoted to developing ignition-resistant Mg alloys with alloying additions [22–45]. Those studies focused on the addition of alloying elements to Mg commercial alloys, the testing of binary Mg alloys, or the development of higher order systems using a variety of AE and/or RE

In this work, the combined use of Sr and Ca is proposed to potentially increase the ignition resistance of Mg. Aydin et al. [31] have reported significant improvement in ignition resistance with a Mg–6 wt% Sr alloy. This was attributed mainly to the surface enrichment of Sr and the subsequent formation of SrO that can decrease the amount of MgO formed and, therefore, reduce the drastic increase in surface temperature, thereby reducing the evaporation and ignition of Mg.

In this study, a ternary Mg-Sr-Ca alloy with the composition of Mg-2.5 wt% Sr-1.0 wt% Ca is proposed. The addition of 2.5 wt% Sr is based on previous studies [29, 31] where an increase of the ignition temperature to 786 °C is seen at this level of Sr, with only small improvement at higher Sr levels. On the other hand, Ca shows a solid solubility in Mg of 1.34 wt% at 516.5 °C. The solid solubility of Ca is an advantage because the dissolution of eutectic phases at elevated temperatures and the generation of a single-phase alloy can create a homogeneous oxide layer at the metal-oxide interface [45]. Hence, a 1.0 wt% Ca addition was selected. The objective of our current research was to understand the role of Ca and Sr on the ignition resistance of Mg. The long-term objectives would include the evaluation and optimization of the alloys for mechanical performance in structural applications.

4.2 Experimental Procedure

The alloy was synthesized using a Norax Induction Furnace (20 kW/5 kHz), under a protective SF_6/CO_2 atmosphere. Pure Mg supplied by Magnesium Elektron Limited with a purity

of 99.9 %, Mg-30 wt% Ca master alloy provided by Timinco and pure Sr provided by the same company were used. Pure Mg was melted at 690° C under a CO_2/SF_6 protective atmosphere using a graphite crucible; commercially pure Sr and Mg- 30 wt% Ca master alloy were added, and melt was held for 15 minutes to allow the dissolution of the alloying elements. The alloy was poured at 730 °C in an H13 tool-steel mold coated with boron nitride which was preheated to 400 °C to produce a plate casting 6mm in thickness. The composition of the alloy was obtained through Inductively Coupled Plasma Argon Plasma and Atomic Emission Spectroscopy (ICP-AES), performed at the NADCAP certified laboratory Genitest Inc. The alloy composition resulted in 2.47 wt% Sr and 1.04 wt% Ca, along with impurities such as Fe, Mn and Si that together represented only 0.049 wt%.

Samples with dimensions of 15x15x6 mm were cut from the plates for ignition testing, placed in a Lindberg Blue resistance furnace and heated continuously with a heating rate of ~45 °C/min, blowing extra dry air inside the furnace at a rate of 0.9 L/min. The presence of water vapour was reported to increase the oxidation rate of magnesium (experiments take place well beyond water vaporization temperature) [53]. The samples were held inside a steel crucible with a K-type thermocouple attached in a hole of 1.98 mm of diameter drilled in the sample. The temperature change was monitored with a Grant Squirrel data logger (2020 series).

For the isothermal heating tests, samples of 15x5x6 mm were cut from the plates. Two temperatures, 500 ºC (solid-state) and 670 ºC (liquid state) were used. For isothermal heating tests in the solid-state, an SPX Blue M Electric Mechanical Convection Furnace was used. The furnace was preheated to 500 °C, then the samples were placed in the furnace and held for 15, 60, and 180 minutes. The isothermal heating tests in the liquid state were performed in a Norax induction furnace (20 kW/5 kHz), using a current between 4 and 8 A. The samples were heated with a rate

of 12 °C/min up to 670 °C to reach the liquid state and were held for 15 minutes. Further holding would result in the ignition of the sample.

The oxidized surfaces of the samples were analyzed via a Hitachi SU3500 Scanning Electron Microscope and Energy Dispersive X-ray Spectroscopy (SEM/EDS). An accelerating voltage of 15 kV was employed to obtain the images and for the EDS analysis. The samples were indented using a Vickers hardness tester to follow up the changes taking place in the solid sample heated isothermally at 500 °C.

Thermo Scientific K-Alpha X-Ray Photoelectron Spectroscopy (XPS) was used to analyze the oxide scale formed on selected samples from the interrupted ignition tests. A pass energy of 200 eV and a step size of 1 eV were used to determine the chemical composition of the oxide scale (also known as survey spectra), while a high-resolution scanning spectrum was collected using a pass energy of 50 eV and a step size of 0.1 eV to identify the chemical state of an element when needed. A 400 μm diameter region was utilized to obtain a compositional depth profile of the surface by gradually removing layers of oxide scale via an Ar ion beam, with a rate of 0.72 nm/second when Ta_2O_5 is etched, which is the reference material of the instrument for the removal process. The compounds present in our oxide scales have a lower hardness than Ta_2O_5. Hence the actual depth might be more extensive. The sample was etched until a metallic component of the Mg alloy was detected at the deepest etching levels. C was removed from the elemental quantification for clarity of the results. Due to the high oxygen affinity of Mg, the sample surface oxidizes even inside the test chamber between etching steps when a depth profile is performed (vacuum inside the chamber is around ~$1x10^{-8}$ bar). Hence, the detection of the Mg KLL metallic component in the survey scans was used to determine the oxide/metal interface, considering that oxygen would be present during the analysis. The chemical shift of Mg in this region makes it

easier to detect the metallic component [54]. The region where this component was detected is indicated with a red dotted line in the XPS depth profiles. In case of charging, the spectra were corrected by aligning the binding energy scale with the C1s hydrocarbon contamination peak to 285 eV. Certain factors had to be considered to determine the amount of Ca present in the alloy surface. The Ca2p doublet peaks interfere with the Mg $KL_1L_{2,3}$ Auger peak in the range between 360 and 344 eV [55], leading to complications for both compositional analysis and chemical state assessment when Mg content is high at a specific etching level. Hence, the Ca2s peak was considered for the compositional analysis in the survey scans, using a relative sensitivity factor (RSF) of 2.106 to determine the amount of Ca present in the surface. For the high-resolution scans, if the region analyzed was rich in Ca and Mg content was low, the habitual Ca2p region was deconvoluted.

4.3 Results

4.3.1 Thermodynamic Simulation and SEM/EDS Analysis of the Cast Alloy

In Fig. 4.1, an isopleth calculated using FactSage-FTlite™ with a constant composition of 1.0 wt% Ca and variable Sr wt% is shown. The dotted line represents the composition of the alloy where the phase selection below 500 °C is predicted to be the intermetallics Mg_2(Ca, Sr) and $Mg_{17}Sr_2$ along with the α-Mg matrix. The solidus temperature of the alloy is 514 ºC, and the liquidus temperature is 636 ºC. At 520 °C, there is a narrow region where Mg_2(Ca, Sr) phase dissolves into both the matrix and $Mg_{17}Sr_2$ intermetallic compound. Due to its eutectic nature, the Mg_2(Ca, Sr)/α-Mg eutectic micro constituent and $Mg_{17}Sr_2$ are predicted to melt at 561 ºC, leaving behind only a fraction of the α-Mg matrix until the alloy reaches a fully molten state.

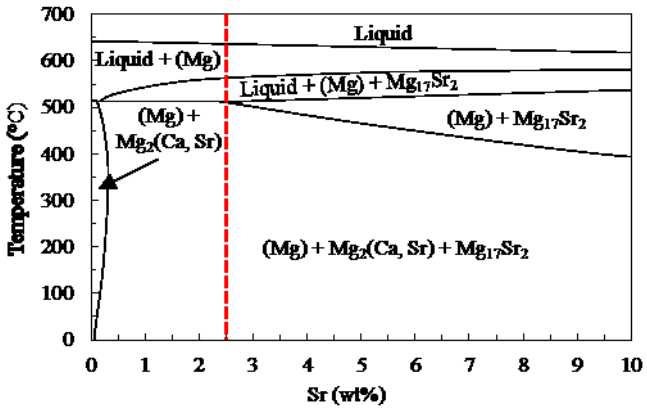

Fig. 4. 1. Mg-XSr-1.0Ca isopleth (calculated using FactSage-FTlite™ with a constant composition of Mg-1.0 wt% Ca and variable Sr wt%). The dotted line represents the composition of the alloy which is predicted to have below 500°C the intermetallics $Mg_2(Ca,Sr)$ and $Mg_{17}Sr_2$ and α-Mg.

The SEM micrographs of Mg-2.5Sr-1Ca alloy are shown in Fig. 4.2. The alloy possesses the α-Mg matrix containing a low amount of Ca in solid solution (marked A in Fig. 4.2). This is a result of supersaturation due to the fast solidification of the alloy in the permanent mold. The eutectic α-Mg/Mg_2Ca (C14, $MgZn_2$ type) predicted by thermodynamic simulations is also seen in Fig. 4.2 (marked B), exhibiting a lamellar cooperative growth morphology. This intermetallic compound (Mg_2Ca) contains a certain amount of Sr, which can occupy the same sublattice positions as Ca due to their similar characteristics. [46] The intermetallic will be referred to as $Mg_2(Ca, Sr)$ from here on. A bulky interdendritic phase gives Mg, Sr and minor Ca peaks (marked C in Fig. 4.2) which are attributed to the $Mg_{17}Sr_2$ (hP38, $Ni_{17}Th_2$ type) phase predicted by thermodynamic simulations. This intermetallic has been reported to have limited Ca solubility [47] and will be designated as $Mg_{17}Sr_2(Ca)$ from here on.

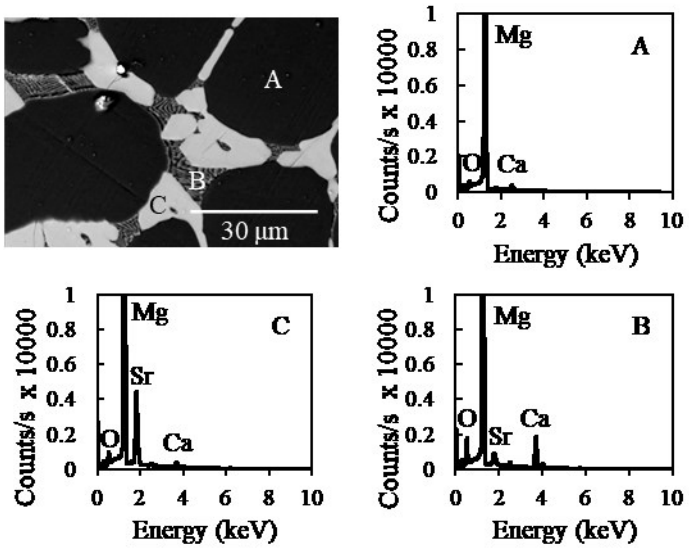

Fig. 4. 2. SEM/BSE micrograph of as-cast Mg-2.5Sr-1Ca alloy. (A) A small amount of retained Ca is present in the matrix due to fast solidification of the permanent-mold casting. (B) A Mg-Mg_2Ca eutectic micro constituent is present; this compound has some Sr solubility as well. (C) Sr is concentrated mostly at the $Mg_{17}Sr_2$ intermetallic, which has a little solubility of Ca.

4.3.2 Ignition Temperature (T_i)

The T_i of the alloy was measured to be 747 ± 16 °C, while the T_i of pure Mg is 634 ± 2 °C. This indicates an increase of ~110 ºC. An example of the heating curves generated is presented in Fig. 4.3. The 45 °C/min heating rate corresponds to the initial linear temperature increase observed at the start of the Time vs Temperature curve in Fig. 4.3. It is important to note that the measured temperature corresponds to the center of the Mg sample in the middle of the furnace, hence, other factors such as melting (heat of fusion), and heat dissipation would continuously modify the curve slope in later stages of the experiment.

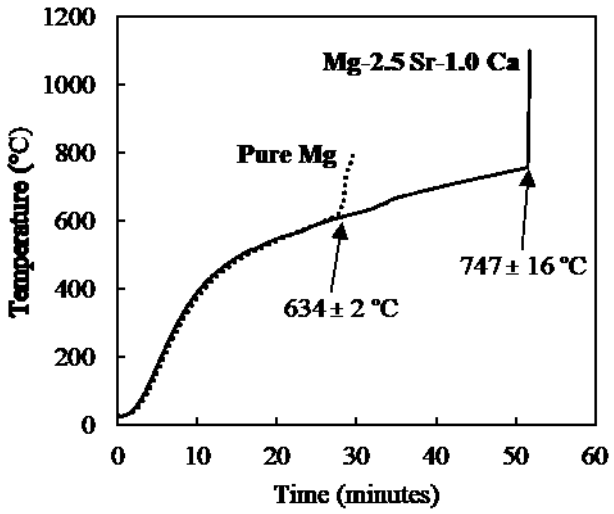

Fig. 4. 3. Example of the temperature vs. time curves obtained during ignition tests. The ignition point is characterized by a sharp increase in temperature.

4.3.3 Isothermal Holding Tests

Isothermal holding tests at 500 °C were conducted on the alloy to monitor the evolution of the oxide scale at 15, 60, and 180 minutes. An isothermal holding test was also conducted at 670 °C for 15 minutes to observe the oxide scale formation on the molten alloy.

4.3.3.1 Oxide evolution on the solid alloy at 500 ºC

The SEM-backscattered electrons (BSE) micrographs in Fig. 4.4 show the microstructure evolution of the cast Mg-2.5Sr-1Ca alloy during isothermal holding at 500 °C. Figure 4.4a is the alloy in the as-cast condition. After 15 min of isothermal heating at 500 °C (Figure 4.4b), the $Mg_2(Ca,Sr)$ eutectic micro constituent starts losing its lamellar morphology and undergoes spheroidization. The $Mg_{17}Sr_2(Ca)$ intermetallics do not seem to alter. As the isothermal holding time increases to 60 minutes (Figure 4.4c), a larger fraction of the lamellar eutectic micro constituent $Mg_2(Ca,Sr)$ continues spheroidizing. Small, round, and bright particles are also seen

near the lamellar region. After 180 minutes holding at 500 °C (Figure 4.4d), Ca-rich particles precipitate out from the supersaturated matrix. The EDS analysis shown in Figure 4.4f indicates that Sr is present mainly at the interdendritic region, while Ca is present in the matrix, concentrating as well in the round particles.

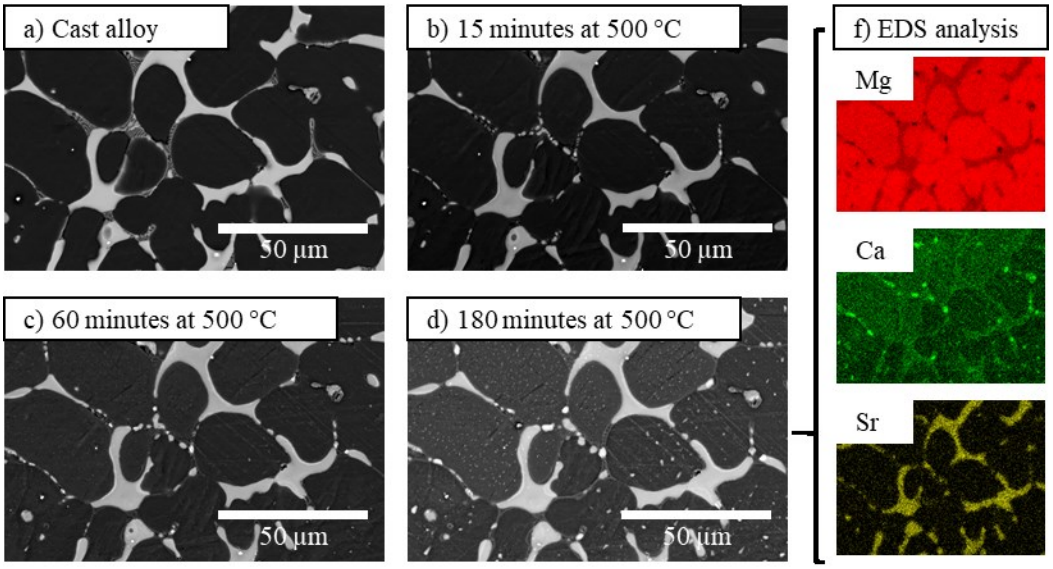

Fig. 4. 4. Microstructure of (a) cast Mg-2.5Sr-1Ca alloy and after isothermal holding at 500°C for (b) 15 minutes, (c) 60 minutes and (d) 180 minutes, e) EDS analysis of the Mg–2.5Sr–1Ca alloy after isothermal holding at 500 C for 180 min.. The same sample was used for each step; it was placed back in the furnace to continue the isothermal heating. The same region marked using a Vickers hardness indenter was analyzed.

The surface analysis performed through XPS at each isothermal holding step is presented in Figure 4.5. It is seen that, as the holding time increases, the oxide thickness increases from ~250 nm at 15 minutes to ~500 nm after 180 min, as deduced from the appearance of the Mg metallic component in the Mg KLL region. The oxide scale is composed mainly of Ca and Mg. The scale is rich in Ca at the gas/oxide interface after 15 minutes indicating the selective oxidation of Ca in the early stages. After 60 and 180 minutes, it is seen that Ca reaches the highest level at the mid-

thickness of the oxide. The Ca level at the outermost surface reaches a maximum of 20 at% throughout the duration of the isothermal holding. On the other hand, the Mg level at the outermost surface decreases from 10 at% (15 min.) to 7 at% (60 min.) and finally towards 0.5 at% (180 min.). In summary, Figure 4.5 indicates that the oxide scale becomes richer in Ca than in Mg in times in excess of 60 minutes of holding. Sr remains at quantities close to zero at the outermost surface even at 60 minutes, increasing only to 1.8 at% after 180 minutes.

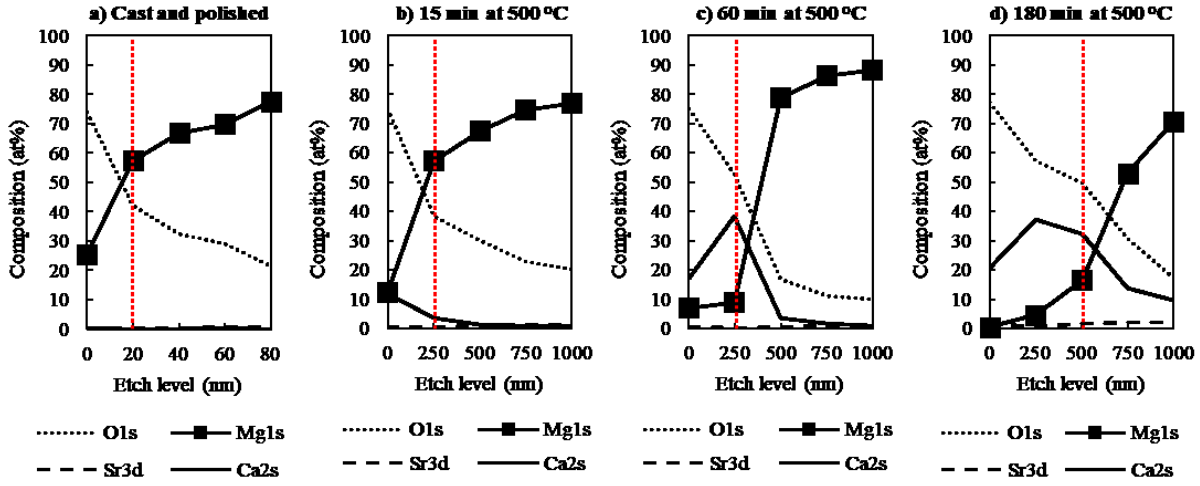

Fig. 4. 5. XPS depth profiles of a) Mg–2.5Sr–1Ca cast alloy after b) 15 min, c) 60 min, and d) 180 min of isothermal holding at 500 C. The red dotted line indicates the level at which the Mg metallic component is clearly visible in the Mg KLL region, marking an approximate position for the metal/oxide interface. The Mg percentage in the outermost surface reduces over time, whereas the Ca content tends to increase.

The shift in binding energy of the XPS high-resolution peaks was analyzed from a region 250 nm below the outermost surface (mid-thickness) of the samples isothermally heated at 500 °C for 180 minutes (Figure 4.6). This was done to identify the precise chemical state of the elements in the oxide scale during oxidation. This region is the middle point in the oxide scale thickness. The Binding Energy and Full Width Half Maximum (FWHM) values for each peak were compared

to the ones found in the literature [48-50]. It is known that alkaline earth metal oxides are prone to undergo hydroxylation and/or carbonation when in contact with the atmosphere [51], hence, the presence of different carbonates and/or hydroxides was expected through the analysis. For the Sr 3d5/2 region, we can observe a peak at 133.7 eV (FWHM=1.4), which corresponds to SrO, along with a peak belonging to Sr $(OH)_2$ at 134.9 eV (FWHM=1.6). In both cases, the Sr 3d3/2 peaks are adjusted at their respective pairs at 1.8±0.1 eV. The Ca 2p3/2 region shows the presence of two peaks; CaO at 346.7 eV (FWHM=1.7) and Ca $(OH)_2$ at 347.7 eV (FWHM=1.7). A small contribution from a peak at 345.4 eV (FWHM=1.65) was assigned to the metallic Ca component. The Ca2p peak doublet is separated by 3.4 eV (+0.2-0.1) in all cases. The contribution of the Mg Auger peaks (which usually overlaps with the Ca2p region) was disregarded due to its small contribution when compared to Ca peaks. The O1s region shows a contribution from the O^{2-} species bonded to CaO at 529.8 eV (FWHM=1.8) and MgO at 531.0 eV (FWHM=1.6). The Mg 2p peak intensity is very low compared to the Ca 3s peak detected within its energy range, and it displays a BE of 50.5 eV (FWHM=1.75) which corresponds to MgO. Hence, the oxide scale is composed mainly by MgO, CaO, and a small amount of SrO along with their hydroxides formed due to the exposure to the atmosphere.

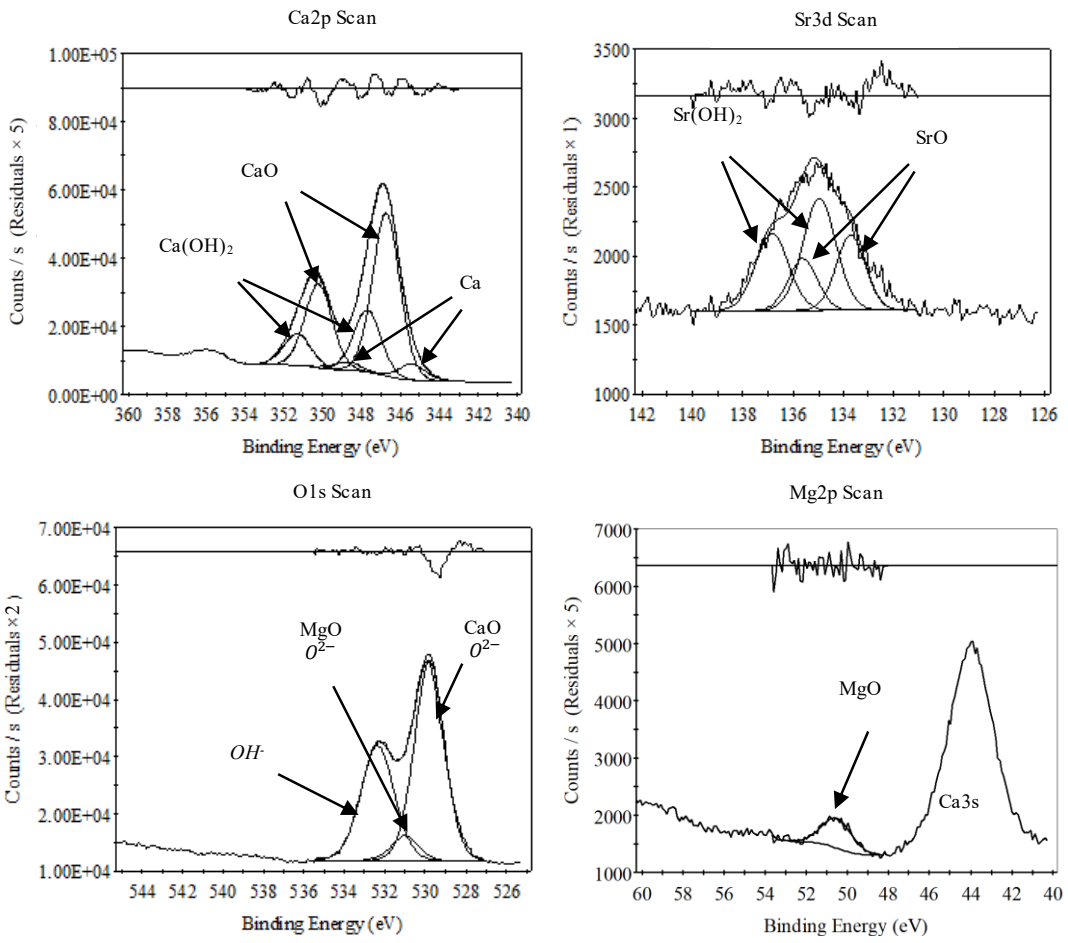

Fig. 4. 6. High resolution XPS analysis of Mg-2.5Sr-1Ca alloy after 180 min at 500 °C at a depth of ~ 250 nm from the surface that is the middle point in the oxide scale thickness. A plot of the fitting residuals is shown above each high-resolution scan.

4.3.3.2 Oxide characteristics on the liquid alloy at 670 ºC

After 15 minutes of isothermal holding at 670 °C (liquid state), the oxide scale displays cracks and small oxide nodules, as presented in the SEM micrograph in Figure 4.7b. The EDS line scan shows that the nodules are rich in Sr, Ca and O (Figure 4.7c). The bright grey regions are re-solidified intermetallic phases over which the amount of Sr is slightly higher. The XPS depth profile (Figure 4.7c) shows a large amount of Ca (~10 at%) in the outermost region of the oxide, as well as a high amount of Sr (~ 18 at%). The amount of Sr is much higher than the level observed

at 500 °C after 180 minutes of isothermal holding (1.8 at%). As the analysis proceeds towards the metal/oxide interface, Sr and Ca content starts to decline and Mg rises.

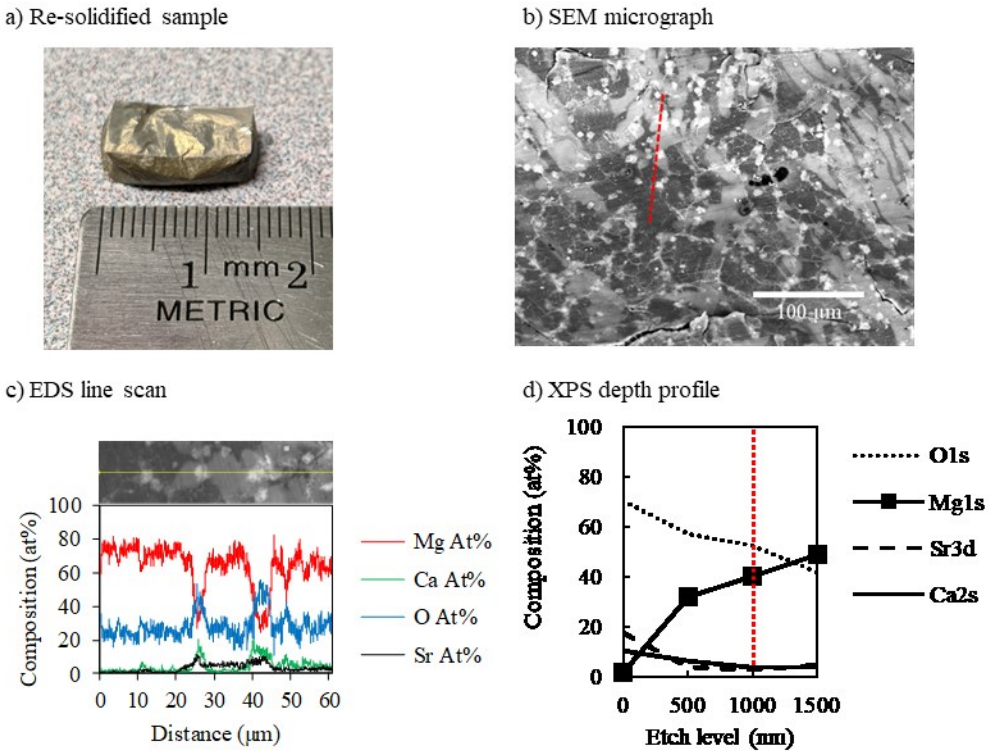

Fig. 4. 7. (a) Mg-2.5Sr-1.0Ca alloy oxidized sample after isothermal holding at 670 °C, showing that the sample swells and partially collapses after 15 minutes of holding. (b) SEM micrograph of the re-solidified alloy surface. (c) EDS line scan of the oxide nodules and the re-solidified intermetallic compounds. The red dotted line in (b) represents the trajectory of the EDS line scan. (d) XPS depth profile of the Mg-2.5Sr-1Ca alloy after isothermal holding at 670 ºC for 15 minutes. Sr content has increased significantly when compared to the isothermal test at 500 ºC.

4.4 Discussion

In this study, the T_i of the ternary alloy Mg-2.5Sr-1Ca was determined to be 747 ± 16 °C which is higher than the T_i of pure Mg which is 634 ± 2 °C using a heating rate of 45 °C/min. Isothermal holding experiments were conducted to understand the oxide-scale formation on the

alloy when it is solid (500 ºC) and when it is liquid (670 °C). The results show that the amount of strontium oxide over liquid Mg alloy is much higher than the amount of strontium oxide over the solid alloy. Aydin et al. [29] have observed the surface activity of Sr in molten Mg-Sr binary alloys that leads to crack healing. However, in their work, higher ignition temperatures are reported for Mg-Sr alloys than the ignition temperatures presented in this work. It is noted that in their work a lower heating rate (20 °C/min) is utilized for ignition testing; for Mg-(1-6) Sr alloys, the ignition temperatures reported range from 748 °C - 854 °C and the oxide scale is found to be rich in SrO at the outermost surface [31]. For Mg-(0.5-5) Ca alloys, a range of ignition temperatures (690-900 oC) has been reported in the literature. [25-27, 52]

Comparing the ignition temperature 786ºC of Mg-2.6 Sr [31] to the ignition temperature 747 °C of ternary Mg-2.5Sr-1Ca alloy of this study, we can see that the Ca addition has not been beneficial in improving the ignition resistance of Mg-2.7 Sr binary alloy.

CaO formation reaction possesses the lowest ΔG (Gibbs energy change) values (CaO → -1107 kJ mol^{-1} O_2) compared to MgO and SrO formation reactions (MgO → -1036 kJ mol^{-1} O_2 and SrO → -1028 kJ mol^{-1} O_2). The close oxygen affinity between Sr and Mg (reflected in their similar oxide formation ΔG) makes SrO formation difficult when Ca is present, as both Sr and Mg would be displaced by Ca's higher oxygen affinity. This explains the large amount of CaO observed in the oxide scale formed during the isothermal holding tests at 500 °C. It is also noted that Ca is present through the matrix and the interdendritic region due to its solubility in Mg, while Sr is confined to the interdendritic region of the alloy. At 670 °C, when the alloy is molten, the oxide scale is richer in Sr at the outermost surface; the oxide/gas interface has a Ca:Mg:Sr ratio of 9:1:5. Sr and Ca oxide nodules are observed. The surface-active behaviour of Sr seems to be more dominant when the alloy is in the liquid stage, allowing the formation of SrO due to its greater

activity. This allows the formation of a combined SrO, MgO and CaO scale. The protective nature of this composite oxide is described as follows.

In previous studies on the oxidation and ignition resistance Mg alloys, the Pilling-Bedworth Ratio (PBR) has not been analyzed in-depth; the studies usually consider the PBR of the oxide over its own metal substrate. Therefore, at first sight, it seems contradictory that CaO would generate a protective oxide despite its PBR of 0.68; Sakamoto et al. [11] stated that CaO does not exhibit a protective behavior over pure molten Ca despite being protective over molten Mg. However, when a composite oxide forms over an alloy, the volume of the composite oxide over the volume of the specific alloy needs to be assessed; as such it is possible to estimate an Effective Pilling-Bedworth Ratio (EPBR), which takes into consideration the formation of a composite oxide over a specific alloy. EPBR is defined as

$$EPBR = \frac{M_{oxide}.\rho_{alloy}}{n\,\rho_{oxide}.M_{alloy}.} = \frac{Molar\ Volume\ Oxide}{Molar\ Volume\ Alloy.} \qquad (I)$$

where, M = atomic mass; ρ = density; and n = number of metal atoms per oxide molecule. The oxide here is either MgO, CaO or SrO or a combination of these oxides. The metal is our ternary Mg alloy. The molar volume of the ternary alloy has been approximated by using a density of 1.8 g cm^{-3} rater than 1.7g cm^{-3} (for pure Mg) for the solid alloy and 1.7 g cm^{-3} for the liquid alloy rather than 1.5 g cm^{-3}. This results in a molar volume of 13.5 $cm^3\ mol^{-1}$ for the solid alloy and 14.29 $cm^3\ mol^{-1}$ once it reaches the liquid state. Considering the molar volumes of CaO (14.99 $cm^3\ mol^{-1}$), SrO (22.04 $cm^3\ mol^{-1}$) and MgO (11.11 $cm^3\ mol^{-1}$) and using equation (1), the EPBR of different oxide/alloy combinations can be calculated. The EPBR of CaO/Mg alloy would be equal to 1.11 in the solid state and 1.05 in the liquid state. SrO/Mg EPBR equals 1.63 in the solid state and 1.54 in the liquid state. SrO forms the most compact oxide scale on the ternary Mg-Sr-Ca alloy

both in the solid and liquid states thanks to its high molar volume. As a comparison, the EPBR of MgO/Mg alloy is 0.82, indicating a non-compact oxide scale.

Table 4. 1. The EPBR of the composite oxide on the Mg-2.5Sr-1Ca alloy at the Metal/Oxide (M/O) and the Gas/Oxide G/O Interfaces at different holding times and temperatures.

500 °C, 15 minutes		**500 °C, 60 minutes**		**500 °C, 180 minutes**	
M/O interface (250 nm)	*G/O interface*	*M/O interface (250 nm)*	*G/O interface*	*M/O interface (500 nm)*	*G/O interface*
MgO:CaO ~1:15 EPBR~0.84	MgO:CaO ~1:1 EPBR ~ 0.97	MgO:CaO ~4:1 EPBR ~1.05	MgO:CaO ~2:1 EPBR ~1.01	CaO:MgO:SrO ~ 32:16:1 EPBR ~1.03	CaO:SrO ~10:1 EPBR ~1.16

670 ºC, 15 minutes		
M/O interface (1000 nm)	*Middle oxide (500 nm)*	*G/O interface*
CaO:MgO:SrO ~ 4:40:3 EPBR ~0.85	CaO:MgO:SrO ~3:16:2 EPBR ~0.89	CaO:MgO:SrO ~5:1:9 EPBR ~1.33

Table 4.1 describes the evolution of the EPBR of the composite oxide based on the XPS depth profile analysis. At 500 °C, in the first 15 minutes, the solid alloy forms a non-protective oxide scale at both the metal/oxide interface and the gas/oxide interface, with EPBR values of 0.84 and 0.97 respectively. This is caused by the low amount of Ca, and Sr present at the surface at this stage. After 60 min, a CaO/MgO scale with EPBR of ~1.05 is formed at the metal/oxide surface and an EPBR of 1.01 at the gas/oxide interface. After 180 minutes, the scale is a CaO/MgO/SrO composite oxide; the EPBR is 1.03 at the metal/oxide interface and 1.16 at the gas/oxide interface. The scale is more compact on the outer surface than on the metal/oxide interface through the isothermal heating at 500 °C, which is more protective than the MgO scale. At 670 °C, the alloy is liquid, and the scale that forms is a CaO/MgO/SrO composite at the metal/oxide interface with an EPBR of ~0.85, which is less compact than the metal/oxide interface when the alloy is solid. However, at the outermost surface, the scale is a compact CaO/SrO composite oxide with an EPBR

of 1.33, thanks to the enrichment of Sr at this stage. It is seen that while the metal/oxide became less protective when the alloy melts, the gas/oxide interface is more compact than when the alloy was solid. XPS indicates only an overall composition and cannot characterize the inhomogeneity of the oxide, however, SEM/EDS results indicate the formation of a Ca rich oxide on the intermetallics and the existence of CaO over the Mg alloy matrix.

Thermodynamic calculations demonstrate that the main three oxide species present in this alloy are MgO, SrO and CaO at high temperatures. No spinel formation is observed or predicted. The EPBR of MgO, SrO, CaO and the composite oxides as determined by the XPS analysis of thin etching layers all show EPBR>1. Both the solid and liquid alloys of CaO/Mg and SrO/Mg show EPBR > 1. If we consider inhomogeneity, the EPBR of CaO/Mg alloy is 1.11 in the solid state and 1.05 in the liquid state. EPBR SrO/Mg equals 1.63 in the solid state and 1.54 in the liquid state. Only the EPBR of MgO/Mg alone is less than 1 (0.82). It can be deduced that the incorporation of Ca and Sr in the alloy leads to a significant increase in the compaction of the oxide scale.

In the solid-state, the contribution of Ca is more noticeable, with Sr existing at very low levels through the oxide scale. Here, the coexistence of Ca and Sr may not be desirable since Ca, due to preferred oxidation and fast diffusion through MgO [52], prevents the formation of an oxide scale rich in SrO in the solid state. We can call this a "negative interaction of Ca and Sr". However, once the liquid state is reached, the contribution of Sr becomes more noticeable due to it surface-active behaviour, enriching the outermost surface of the composite oxide scale. It can be deduced that while Sr improves the ignition resistance of Mg-Ca alloys, Ca may lower the ignition resistance of Mg-Sr alloys. The close oxygen affinity of Sr with Mg plays a detrimental role in the formation of a protective oxide scale when Ca is present in the alloy.

4.5 Conclusions

The ignition resistance of an Mg-2.5Sr-1Ca alloy was tested, resulting in an increase of approximately 100 °C compared to pure Mg. When compared to previous studies, it is possible to observe that while the addition of Sr might be beneficial for Mg-Ca alloys; it seems that the presence of Ca reduces the ignition temperature generally reported for binary Mg-Sr alloys. The following conclusions are drawn based on the analyses of the present work: 1) At 500 °C, in the solid stage, the oxide scale contains mainly CaO, while MgO at the surface decreases over time, leading to the development of a compact oxide scale at the surface. CaO formation is favored over SrO due to the lower energy of formation of the former. 2) At 670 C, when the alloy is molten, the amount of SrO in the oxide scale is higher compared to the solid state. The presence of SrO contributes to the formation of a more compact oxide scale at the oxide/gas interface than at the metal/oxide interface. 3) The combined use of Sr and Ca does not result in a synergistic effect due to the close oxygen affinity of Sr and Mg and due to the fact that Ca, because of its preferred oxidation and fast diffusion through MgO prevents the formation of SrO-rich and more protective scale over the solid alloy. This can be described as the negative interaction of Ca and Sr.

4.6 Acknowledgements

This project was conducted under the financial support of the Natural Sciences and Engineering Research Council of Canada (NSERC) Discovery Grant. The authors would like to thank Dr. Robin R.L. Drew from Concordia Unviersity and Dr. Amir R. Farkoosh from Northwestern University for their valuable discussions and Pierre Vermette (McGill University) for his assistance in alloy making and casting. Luis A. Villegas-Armenta gratefully acknowledges the financial support of CONACYT of Mexico for his scholarship # 410607 and McGill Engineering Doctoral Award program (MEDA).

4.7 References for Chapter 4

[1] T.-S. Shih, J.-B. Liu, and P.-S. Wei, "Oxide films on magnesium and magnesium alloys," *Mater. Chem. Phys.,* vol. 104, pp. 497–504, 2007.

[2] T. Takeno and S. Yuasa, "Ignition of Magnesium and Magnesium-Aluminum Alloy by Impinging Hot-Air Stream," *Combust. Sci. Technol.,* vol. 21, no. 3-4, pp. 109-121, 1980.

[3] W. M. Fassell, L. B. Gulbransen, J. R. Lewis, and J. H. Hamilton, "Ignition temperatures of magnesium and magnesium alloys," *J. Met.,* vol. 3, no. 7, pp. 522-528, 1951.

[4] M. V. Derevyaga, L. N. Stesik, and E. A. Fedorin, "Critical Conditions for the Ignition of Magnesium," *Fiz. Goreniya Vzryva,* vol. 14, no. 6, pp. 44-49, 1977.

[5] P. Boris, "A study of the flammability of magnesium," Defense Technical Information Center1964.

[6] T. R. Marker, "DOT/FAA/TC-13/52 - Development of a Laboratory-Scale Flammability Test for Magnesium Alloys Used in Aircraft Seat Construction," Federal Aviation Administration, New Jersey2014.

[7] B. L. Bobryshev and Y. P. Aleksandrova, "Ignition of Magnesium and its Alloys," *Metalloved. Term. Obrab. Met.,* no. 3, pp. 41-44, 1988.

[8] F. Czerwinski, "Controlling the ignition and flammability of magnesium for aerospace applications," *Corros. Sci.,* vol. 86, pp. 1-16, 2014.

[9] F. Czerwinski, "The reactive element effect on high-temperature oxidation of magnesium," *Int. Mater. Rev.,* vol. 60, no. 5, pp. 264-296, 2015.

[10] N. Birks, G. H. Meier, and F. S. Petit, *Introduction to High Temperature Oxiation. 2nd Edition.* New York: Cambridge University Press, 2006.

[11] M. Sakamoto, S. Akiyama, and K. Ogi, "Suppression of ignition and burning of molten Mg alloys by Ca bearing stable oxide film," *J. Mater. Sci. Lett.,* vol. 16, no. 1048-1050, 1997.

[12] Y. M. Kim, C. D. Yim, H. S. Kim, and B. S. You, "Key factor influencing the ignition resistance of magnesium alloys at elevated temperatures," *Scr. Mater.,* vol. 65, no. 11, pp. 958-961, 2011.

[13] N. Mebarki, N. V. Ravi Kumar, J. J. Blandin, M. Suery, and F. Pelloux, "Correlation between ignition and oxidation behaviours of AZ91 magnesium alloy," *Mater. Sci. Eng.,* vol. 21, no. 1145-1151., 2005.

[14] P.-Y. Lin, H. Zhou, W.-P. Li, W. Li, S.-Z. Zhao, and J.-G. Su, "Effect of yttrium addition on the oxide scale of AM50 magnesium alloy," *Corros. Sci.,* vol. 51, no. 1128–1133, 2009.

[15] J.-s. Rao, H.-j. Li, and H.-s. Xue, "Ignition-proof mechanism of ZM5 magnesium alloy added with rare earth," *J. Cent. South Univ. Technol.,* vol. 17, no. 1, pp. 28-33, 2010.

[16] N. B. Pilling and R. E. Bedworth, "The Oxidation of Metals at High Temperatures," vol. 29, no. 529, 1923.

[17] C. Xu and W. Gao, "Pilling-Bedworth ratio for oxidation of alloys," (in English), *Mater. Res. Innovations,* vol. 3, no. 231–235, pp. 231-235, Mar 2000.

[18] H. Yamauchi, "Surface segregation in jellium binary solid solutions," vol. 31, no. 12, 1984.

[19] P. Politzer, R. G. Parr, and D. R. Murphy, "Approximate determination of Wigner-Seitz radii from free-atom wave functions," *Phys. Rev. B,* vol. 31, no. 10, p. 6809, 1985.

[20] J. H. Rose, J. R. Smith, F. Guinea, and J. Ferrante, "Universal features of equation of state of metals," *Phys. Rev. B,* vol. 29, no. 6, pp. 2963-2969, 1984.

[21] E. S. Paul-Gerhard Reinhard, *Introduction to Cluster Dynamics*. John Wiley & Sons, 2004.

[22] D. S. Aydin, Z. Bayindir, M. Hoseini, and M. O. Pekguleryuz, "The high temperature oxidation and ignition behavior of Mg–Nd alloys part I: The oxidation of dilute alloys," *J. Alloys Compd.,* vol. 569, no. 35–44, 2013.

[23] J. F. Fan, G. C. Yang, Y. H. Zhou, Y. H. Wei, and B. S. Xu, "Selective Oxidation and the Third-Element Effect on the Oxidation of Mg-Y Alloys at High Temperatures," *Metall. Mater. Trans. A,* vol. 40A, pp. 2184-2189, 2009.

[24] S. K. Kim, J.-K. Lee, Y.-O. Yoon, and H.-H. Jo, "Development of AZ31 Mg alloy wrought process route without protective gas," *J. Mater. Process. Technol.,* vol. 187, pp. 757-760, 2007.

[25] B. S. You, W. W. Park, and I. S. Chung, "The effect of calcium additions on the oxidation behavior in magnesium alloys," *Scr. Mater.,* vol. 42, pp. 1089–1094, 2000.

[26] T.-S. Shih, J.-H. Wang, and K.-Z. Chong, "Combustion of magnesium alloys in air," *Mater. Chem. Phys.,* vol. 85, no. 2, pp. 302-309, 2004.

[27] S.-Y. Chang, M. Matsushita, H. Tezuka, and A. Kamio, "Ignition prevention of magnesium by simultaneous addition of calcium and zirconium," *Int. J. Cast Met. Res.,* vol. 10, no. 6, pp. 345-351, 1998.

[28] B.-H. Choi, B.-S. You, W.-W. Park, Y.-B. Huang, and I.-M. Park, "Effect of Ca addition on the oxidation resistance of AZ91 magnesium alloys at elevated temperatures," *Met. Mater. Int.,* journal article vol. 9, no. 4, pp. 395-398, 2003.

[29] D. S. Aydin, Z. Bayindir, and M. O. Pekguleryuz, "High Temperature Oxidation Behavior of Hypoeutectic Mg–Sr Binary Alloys: The Role of the Two-Phase Microstructure and the Surface Activity of Sr," *Adv. Eng. Mater.,* vol. 17, no. 5, pp. 697-708, 2015.

[30] J.-K. Lee, H.-H. Jo, and S. K. Kim, "Effet of CaO addition on ignition behavior in molten AZ31 and AZ91D magnesium alloys," *Rare Met.,* vol. 25, no. Special Issue, pp. 155-159, 2006.

[31] D. S. Aydin, Z. Bayindir, and M. O. Pekguleryuz, "The effect of strontium (Sr) on the ignition temperature of magnesium (Mg): a look at the pre-ignition stage of Mg–6 wt% Sr," *J. Mater. Sci.,* vol. 48, no. 23, pp. 8117-8132, 2013.

[32] L. Jin-Kyu, "Effect of CaO composition on oxidation and burning behaviors of AM50 Mg alloy," *Trans. Nonferrous Met. Soc. China,* vol. 21, pp. 23-27, 2011.

[33] D. B. Lee, "High temperature oxidation of AZ31 + 0.3 wt.%Ca and AZ31 + 0.3 wt.%CaO magnesium alloys," *Corros. Sci.,* vol. 70, no. 243–251, 2013.

[34] Y.-B. Huang, I.-S. Chung, B.-S. You, W.-W. Park, and B.-H. Choi, "Effect of Be Addition on the Oxidation Behavior of Mg-Ca Alloys at Elevated Temperature," *Met. Mater. Int.,* vol. 10, no. 1, pp. 7-11, 2004.

[35] A. Prasad, Z. Shi, and A. Atrens, "Influence of Al and Y on the ignition and flammability of Mg alloys," *Corros. Sci.,* vol. 55, pp. 153-163, 2012.

[36] X. Zeng *et al.*, "Study on ignition proof magnesium alloy with beryllium and rare earth additions," *Sci. Mater.,* vol. 43, no. 5, pp. 403-409, 2000.

[37] J. Castle, S. Gregg, J. Antill, and W. Jepson, "The squeeze energy principle and the oxidation of magnesium and of magnox A 12," *J. Nucl. Mater.,* vol. 5, pp. 254-255, 1962.

[38] W. Q. Zeng Xiaoqin, Lu Yizhen, Zhu Yanping, Ding Wenjiang, Zhao Yunhu, "Influence of beryllium and rare earth additions on ignition-proof magnesium alloys," *J. Mater. Process. Technol.,* vol. 112, no. 17-23, 2001.

[39] F. Czerwinski, "The early stage oxidation and evaporation of Mg–9%Al–1%Zn alloy," vol. 46, no. 377–386, 2004.

[40] A. Prasad, Z. Shi, and A. Atrens, "Flammability of Mg–X Binary Alloys," *Adv. Eng. Mater.,* vol. 14, no. 9, pp. 772-784, 2012.

[41] M. Liu, D. S. Shih, C. Parish, and A. Atrens, "The ignition temperature of Mg alloys WE43, AZ31 and AZ91," vol. 54, no. 139–142, 2012.

[42] Q. Tan *et al.*, "Improved oxidation resistance of Mg-9Al-1Zn alloy microalloyed with 60 wt ppm Be attributed to the formation of a more protective (Mg, Be) O surface oxide," *Corros. Sci.,* vol. 132, pp. 272-283, 2018.

[43] S. Tekumalla and M. Gupta, "An insight into ignition factors and mechanisms of magnesium based materials: A review," *Mater. Des.,* vol. 113, pp. 84-98, 2017.

[44] Q. Tan, A. Atrens, N. Mo, and M.-X. Zhang, "Oxidation of magnesium alloys at elevated temperatures in air: A review," *Corros. Sci.,* vol. 112, pp. 734-759, 2016.

[45] D. S. Aydin, M. Hoseini, and M. O. Pekguleryuz, "Understanding the high temperature oxidation and ignition behaviour of two-phase Mg–Nd alloys and a comparison to single phase Mg–Nd," *Philos. Mag.,* vol. 95, no. 3, pp. 259-274, 2015.

[46] M. Aljarrah and M. Medraj, "Thermodynamic modelling of the Mg–Ca, Mg–Sr, Ca–Sr and Mg–Ca–Sr systems using the modified quasichemical model," *Calphad,* vol. 32, no. 2, pp. 240-251, 2008.

[47] V. Raghavan, "Ca-Mg-Sr (Calcium-Magnesium-Strontium)," *J. Phase Equilib. Diffus.,* vol. 30, no. 6, p. 633, 2009.

[48] M. Sosulnikov and Y. A. Teterin, "X-ray photoelectron studies of Ca, Sr and Ba and their oxides and carbonates," *J. Electron. Spectrosc. Relat. Phenom.,* vol. 59, no. 2, pp. 111-126, 1992.

[49] M. Santamaria, F. Di Quarto, S. Zanna, and P. Marcus, "Initial surface film on magnesium metal: a characterization by X-ray photoelectron spectroscopy (XPS) and photocurrent spectroscopy (PCS)," *Electrochim. Acta,* vol. 53, no. 3, pp. 1314-1324, 2007.

[50] R. P. Vasquez, "SrCO3 by XPS," *Surf. Sci. Spectra,* vol. 1, no. 1, pp. 112-116, 1992.

[51] J.-C. Dupin, D. Gonbeau, P. Vinatier, and A. Levasseur, "Systematic XPS studies of metal oxides, hydroxides and peroxides," *Phys. Chem. Chem. Phys.,* vol. 2, no. 6, pp. 1319-1324, 2000.

[52] J. A. Van Orman and K. L. Crispin, "Diffusion in Oxides," *Rev. Mineral. Geochem.,* vol. 72, no. 1, pp. 757-825, 2010.

[53] K.P. Coffin, “Some Physical Aspects of the Combustion of Magnesium Ribbons” *Symp. (Int.) Combust., [Proc.]*, vol. 5, p. 267, 1955.

[54] K. Asami and S. Ono, "Quantitative X-Ray Photoelectron Spectroscopy Characterization of Magnesium Oxidized in Air," *J. Electrochem. Soc.,* vol. 147, no. 4, pp. 1408-1413, 2000.

[55] P. T. M. Van Attekum and J. Trooster, "A plasmon gain satellite in the KLL Auger spectrum of Mg and Al metal," *J. Phys. F: Met. Phys.,* vol. 8, no. 7, p. L169, 1978.

Chapter 5 - The ignition Behavior of Mg-Ca binary alloys; The Role of Heating Rate

According to the results presented in Chapter 4, it was clear that the simultaneous use of Ca and Sr would not result in a significant increase in ignition temperature, caused by the negative interaction between these two elements. Hence, to develop an effective ternary alloy, Chapters 5 and 6 were dedicated to identifying the mechanisms behind the ignition temperature improvement provided by Ca, while Chapter 7 was focused on Sr.

Preliminary results demonstrated that the use of different heating rates could affect the measured ignition temperature of Mg alloys, despite not showing changes when pure Mg was tested under the same conditions. Hence, during the igntion testing of a range of Mg-Ca binary alloys, it was clear that this could be influencing the performance of the previously studied Mg-2.5Sr-1.0Ca alloy. Chapter 5 then presents an exploratory analysis of the microstructure evolution of three Mg-Ca alloys using igntion tests interrupted at the semi-solid and liquid stages, as Mg igntion takes place at the liquid stage. A thermodynamic approach is presented to explain the difference in oxidation behavior of the tested alloys.

Abstract

The ignition temperature of Mg- (1-3) wt% binary alloys have been tested at two different heating rates: a Low Heating Rate (LHR) of 25 °C/min and a High Heating Rate (HHR) of 45 °C/min under a constant flow of extra dry air at a rate of 0.9 L/min. At both heating rates, the ignition temperature increased with Ca in the alloy. For the LHR samples, the ignition temperature increased from 655 °C at 0 wt% Ca to 861 °C at 3 wt% Ca. For the HHR samples, the increase in ignition temperature was lower, from 658 °C to 787 °C as Ca increased from 0 to 3wt%. It was observed that Ca-rich interdendritic regions, when molten in the semi-solid state, resist oxidation more than when they are solid, an effect that can be attributed to the ΔG of CaO formation from the molten and solid phases. Using LHR results in a smooth oxide scale and a higher ignition temperature, which is related to the formation of extensive molten pools, while an HHR yielded irregular oxidation and lower ignition temperature due to the early oxidation of solid intermetallics.

5.1 Introduction

The use of lightweight Mg has currently become essential to meet the challenge of reducing aircraft fuel consumption. The perceived fire risk of Mg alloys had been a major obstacle to their use in several civil aircraft applications, such as several cabin components [1]; however, the recent evaluation conducted by SAE and Boeing have shown that the flammability of Mg alloys is composition dependent. Studies have demonstrated that the use of rare-earths [2,3,12,4–11] and alkaline earth metals such as Be [13–19] and Sr [20,21] have the potential to increase the resistance of Mg to high-temperature oxidation and ignition. Calcium (Ca) is found to be one of the useful alloying elements to increase the ignition temperature of Mg. An early study by Sakamoto et al. [22], indicated that Ca tends to form a protective CaO oxide layer that impedes the contact between oxygen and molten Mg and thereby retarding ignition. Further research has demonstrated

significant improvement in Mg high-temperature oxidation resistance when Ca is added [23]. Researchers [24–27] have reported the effect of Ca in increase the ignition temperature of AZ (Mg-Al-Zn) and AM (Mg-Al-Mn) Mg alloys while other studies [28,29] demonstrated that even small quantities of Ca could eliminate the necessity of SF_6 protective atmosphere required to avoid ignition during Mg casting or processing.

The ignition temperature of Mg alloys is not an intrinsic property [30–32]; several factors such as sample size/geometry or atmosphere can influence their ignition behavior [33] which makes it challenging to elucidate the mechanisms governing the ignition behavior of Mg alloys. In this paper, the effect of another parameter, the heating rate, was observed. The ignition behavior of binary Mg-Ca alloys was evaluated using full-ignition tests and interrupted ignition tests at 560 ºC (semi-solid) and 700 ºC (liquid) under two different heating rates to determine the interactive influence of the heating rate and composition on the ignition temperature.

5.2 Experimental Method

Binary Mg-Ca alloys were synthesized using a Norax Induction Furnace (20 kW/5 kHz) at 690 °C, under a protective SF_6/CO_2 protective atmosphere. The materials used were pure Mg supplied by Magnesium Elektron (purity of 99.8%), and Mg-30 wt% Ca master alloy provided by Timinco Metals LTD. The compositions for the cast alloy (Table 5.1) was determined via Inductively Coupled Plasma – Atomic Emission Spectrometry (ICP-AES), performed by the NADCAP certified laboratory Genitest Inc. All compositions are given in weight % unless otherwise specified.

Table 5.1. Chemical Compositions of the Alloys.

Alloy Designation	**Elements, wt%**							
	Ca	Al	Cu	Fe	Mn	Ni	Si	Mg
Mg – 1 Ca	1.14	0.007	<0.001	0.033	0.016	0.001	0.002	Balance
Mg – 2 Ca	1.77	0.005	<0.001	0.003	0.004	0.001	0.001	
Mg – 3 Ca	2.98	0.006	<0.001	0.002	0.005	0.001	0.001	

Pure Mg was melted at 690 °C prior to adding the Mg-Ca master alloy. Once this was done, the melt was held at the same temperature for 15 minutes to allow mixing. The melt was stirred, and then the slag was removed before pouring it into a 6 mm thick plate-samples using an H13 tool steel permanent mold coated with boron nitride. Samples of 15 x 15 x 6 mm were machined for ignition tests. The samples were ground with 800 grit SiC paper and polished on their wide face down to 0.05 μm with colloidal silica. A hole of 1.98 mm (5/64 inches) in diameter was drilled in one of the narrower faces to attach a K-type thermocouple covered with a 316L stainless steel sleeve (required to protect the thermocouple at ignition). This thermocouple was used to measure the temperature at the center of the sample. The temperature changes were recorded using a Grant Squirrel data logger (2020 series).

For the complete ignition tests, the samples were placed in a Lindberg Blue vertical resistance furnace and heated continuously at two different rates of 25°C/ min (Low Heating Rate – LHR) and 45°C/ min (High Heating Rate – HHR) under a constant flow of extra dry air at a rate of 0.9 L/min. For the interrupted ignition tests, the samples were marked using a Vickers micro-hardness tester in the as-cast state so that the evolution of the oxide formation and microstructural change could be monitored. The samples were then heated under identical conditions to the full

ignition test; however, once the target temperature was reached (560 or 700 °C), the furnace chamber was flushed with Ar to quickly reduce the sample temperature and then removed from the furnace.

The intermetallic compounds present in the alloys were determined via X-ray Diffraction (XRD) using a Bruker diffractometer equipped with a Cu Kα radiation source of λ= 1.54060 Å. The oxidized top surfaces were then analyzed using a Hitachi SU-3500 Scanning Electron Microscope equipped with Energy Dispersive X-ray Spectroscopy (SEM/EDS), using an accelerating voltage of 15 kV. A Backscattered Electron (BSE) detector was used to analyze the microstructural features of the samples at different temperatures of the interrupted ignition test. A dwell time of 300 μs was used for EDS mapping. If a specific microstructural feature could not be observed clearly in the EDS mapping, a detailed line scan analysis was employed.

5.3 Results

5.3.1 Ignition temperature

Pure Mg and three binary compositions; Mg-1.14 Ca (Mg-1Ca), Mg-1.77 Ca (Mg-2Ca) and Mg-2.98 Ca (Mg-3.0 Ca), were continuously heated until ignition to observe the change in ignition temperature with an increasing amount of Ca. Fig.1 shows ignition temperature versus Ca wt% plots for both high heating rate (HHR) and low heating rate (LHR). The Mg-Ca binary phase diagram calculated from FactSage^{TM}-FTlite database is presented in Fig. 5.2, indicating the liquidus temperature for each alloy.

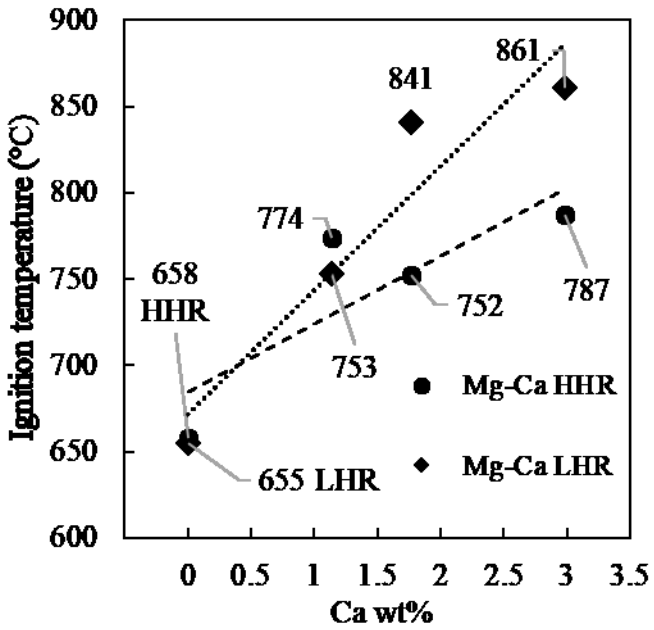

Fig. 5.1. Ignition temperature versus wt% Ca of Mg-Ca binary alloys.

The ignition temperature is defined as the point where a sharp increase in temperature is detected, accompanied by a bright white flame. In our study, the ignition temperature was identified as the point where a sudden and fast increase of temperature was detected, which is when the thermocouple attached to the sample detected a temperature increase of 5 °C within 2 seconds. As seen in Fig. 5.1, the ignition temperature of pure Mg is virtually insensitive to heating rate while the ignition temperature of binary Mg-Ca alloys changes significantly with the heating rate at Ca levels of 1.77% (Mg-2Ca) and 3.0% (Mg-3Ca). These differences suggest that higher Ca content causes a significant difference in ignition temperature.

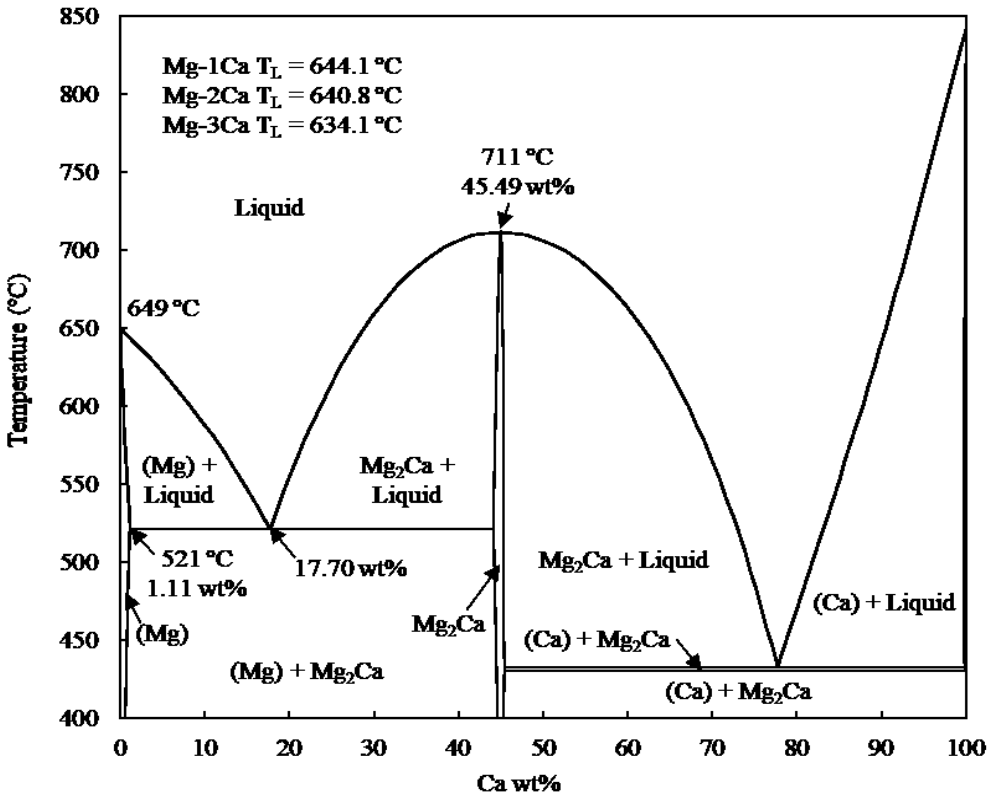

Fig. 5.2. Binary phase diagram for the Mg-Ca system calculated through FactSage^{TM}-FTlite database.

5.3.2 Interrupted ignition Tests: Semi-Solid state at 560 °C

Fig. 5.3 contains the micrographs showing the evolution of a specific region in each alloy (identified with micro-indentation) between the initial as-cast state and after the ignition test was interrupted at 560 °C. The initial microstructure of the three alloys in both sets of experiments (Fig. 5.3 a,c) shows a Mg matrix surrounded by a lamellar eutectic intermetallic, which is formed during the last stages of solidification in the casting process. This intermetallic compound was identified as Mg_2Ca from the XRD spectra (Fig. 5.4) of the Mg-3Ca alloy, which possesses the highest intermetallic fraction suitable for detection using this technique.

When the ignition test is interrupted at 560 °C, the samples are in the semi-solid state (Fig. 5.3 b,d). In the LHR samples, the low-melting-point (521 °C) eutectic microconstituents that are molten during the semi-solid state re-solidify, forming the phases observed in Fig. 5.3b and 5.3d marked as *re-solidified molten pool*. The amount of re-solidified pools increases with increasing Ca. In the HHR samples, it is observed that the amount of the resolidified phase is lower, compared to the LHR samples of the same composition.

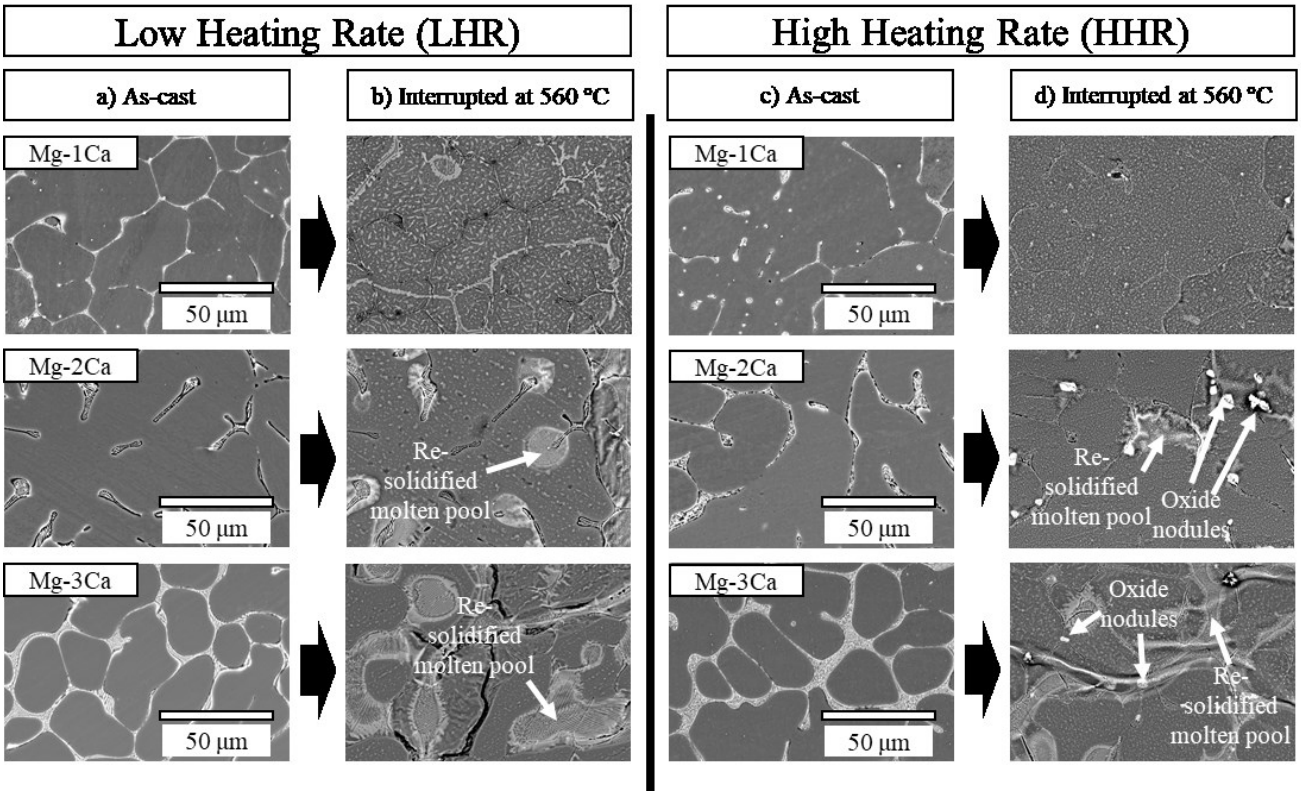

Fig. 5.3. SEM-BSE m*icrographs* of *the samples before and after the interrupted ignition tests at 560 °C using both LHR and HHR. The same region of the sample was followed using micro-indentation.*

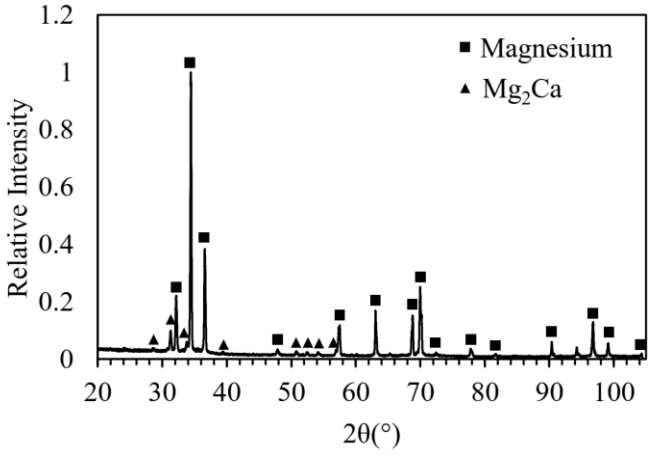

Fig. 5.4. X-Ray diffraction spectra for the Mg-3.0 Ca binary alloy. Both the Mg matrix and the Mg_2Ca intermetallic were detected.

The EDS map analysis of each alloy at 560 °C is presented in Fig. 5.5 for LHR and Fig. 5.6 for HHR samples, respectively. It is observed that the re-solidified pools in the LHR samples (Fig. 5.5) are Ca-rich. As the amount of Ca increases, the surface coverage of this re-solidified Ca-rich phase increases in these samples. The HHR samples, on the other hand (Fig. 5.6), have a low surface coverage of this phase in the Mg-1Ca and Mg-2Ca alloys. Ca-rich nodules are also present in the HHR samples. These nodules are more evident in the Mg-2Ca and Mg-3Ca alloys than in the Mg-1Ca alloy.

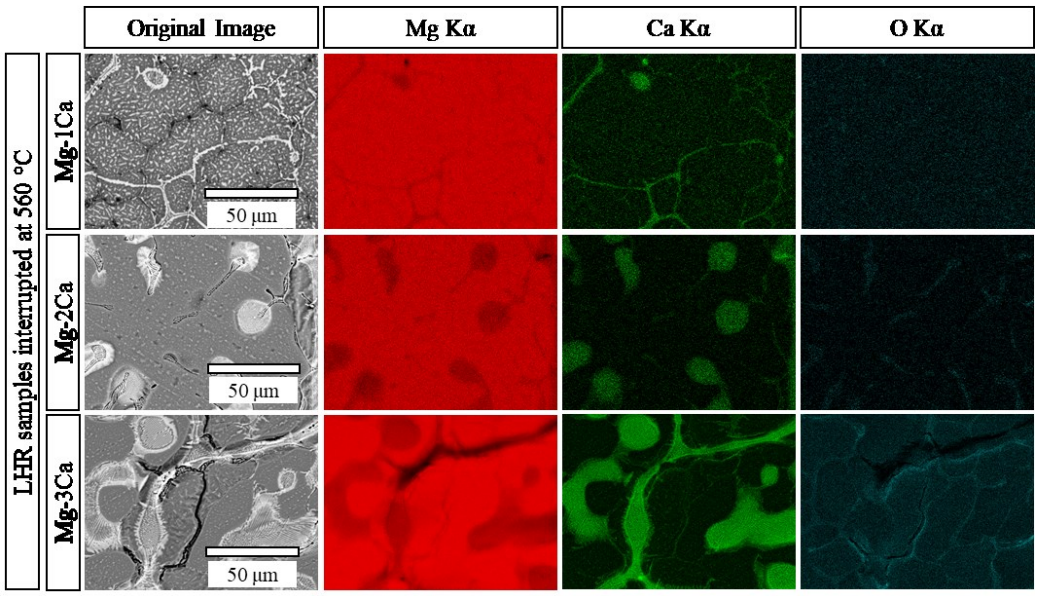

*Fig. 5.5. EDS mapping of the Mg-1Ca, Mg-2Ca and Mg-3Ca alloys after an interrupted ignition test at 560 °C using a*n *LHR. Ca-rich eutectic pools are formed at the metal/oxide interface of the alloy at this stage.*

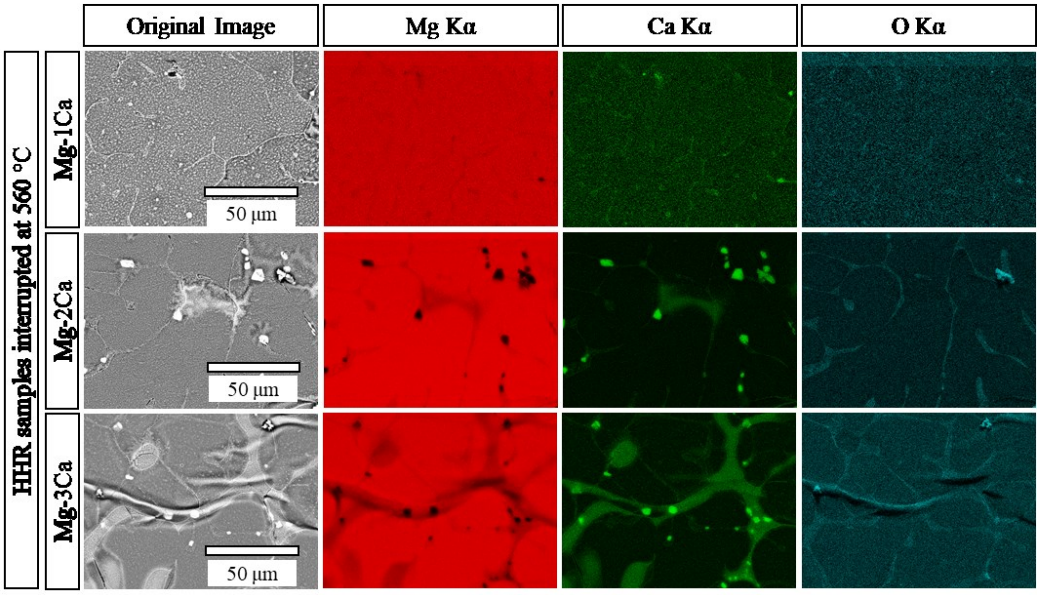

*Fig. 5.6. EDS mapping of the Mg-1Ca, Mg-2Ca and Mg-3Ca alloys after an interrupted ignition test at 560 °C using a*n *HHR. Ca-rich nodules are present along with the Ca-rich eutectic pools also observed in the samples heated using a*n *LHR.*

An additional EDS line scan on the LHR sample re-solidified molten pools (Fig. 5.7a) indicates an amount of approximately 15 at% of Ca (22.5 wt%) over this region. Another line scan was performed on the Ca-rich nodules observed in the Mg-3Ca HHR sample (Fig. 5.7b), which reveals that these particles are composed in almost equal at% amounts of Ca and O, being likely entirely made of CaO. This suggests the occurrence of internal oxidation.

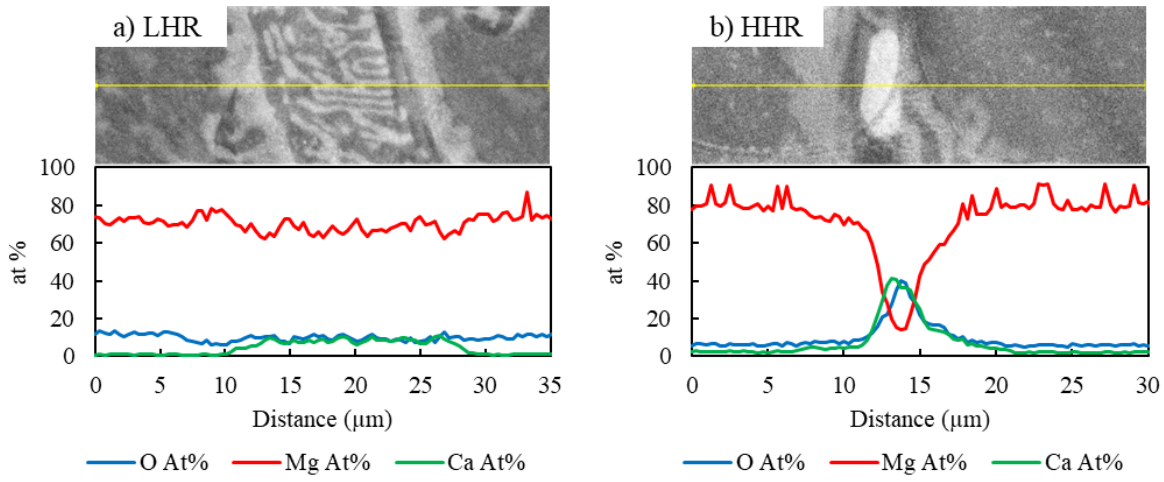

*Fig. 5.7. EDS line scan of (a) the LHR re-solidified molten pool and (b) a*n *HHR sample CaO-rich particle formed at the interdendritic regions of the alloy.*

5.3.3 Interrupted ignition Tests: Liquid state at 700 °C

Fig. 5.8 shows that the HHR sample interrupted at 700 ºC has not reached the fully molten state since it partially maintains its shape while the LHR sample seems to have reached a fully liquid state and collapsed leaving a metal lump once the test is interrupted. At 700 °C, the alloys are liquid according to the phase diagram in Fig. 5.1. A likely explanation is that the thermocouple location is molten while the bulk in the HHR sample has yet not attained full melting due to the

short time elapsed. It is noted that neither the LHR nor the HHR sample has ignited at this temperature.

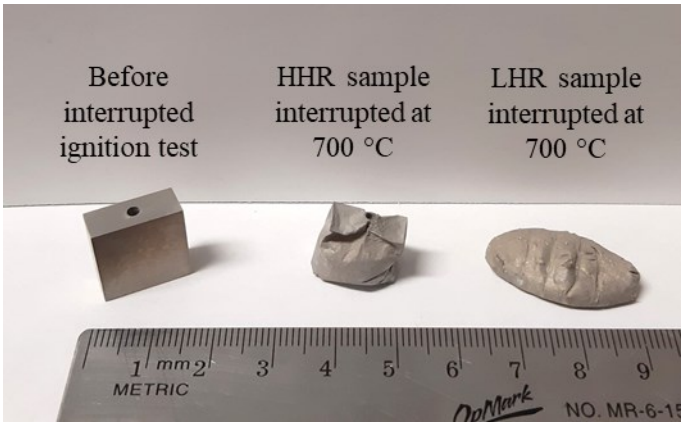

Fig. 5.8. Comparison between Mg-3Ca HHR and LHR samples after the interrupted ignition test at 700 °C.

LHR samples: The BSE images of LHR samples (Fig. 5.9a) show the existence of a resolidified microstructure with an interdendritic phase for the Mg-1Ca and Mg-2Ca alloys. The Mg-3Ca LHR sample has a different appearance with an oxide scale covering the entire surface. All three samples seem to contain some oxide nodules as well; their amount increasing with increasing Ca. The EDS analyses of the LHR samples (Fig. 5.10) reveal that the re-solidified interdendritic phase is Ca-rich in the Mg-1Ca and Mg-2Ca alloys. The oxide nodules observed in these samples are Ca-rich oxides, which are visible in the O mapping. The entire surface of the Mg-3Ca alloy is rich in Ca and O, however, some of the oxide nodules were not detected in the mapping. An additional EDS line scan of one of these nodules is shown in Fig. 5.11, which reveals that they are composed by close amounts of Ca and O, similar to the CaO nodules observed in the HHR samples at 560 °C.

HHR samples: HHR samples (Fig. 5.9b) do not show the re-solidified structure with the interdendritic phase. EDS analysis shows (Fig. 5.12) heavily oxidized surfaces along with

widespread oxide nodules. HHR samples are overall more oxidized when compared to the LHR samples, even when the HHR samples were heated for a shorter time.

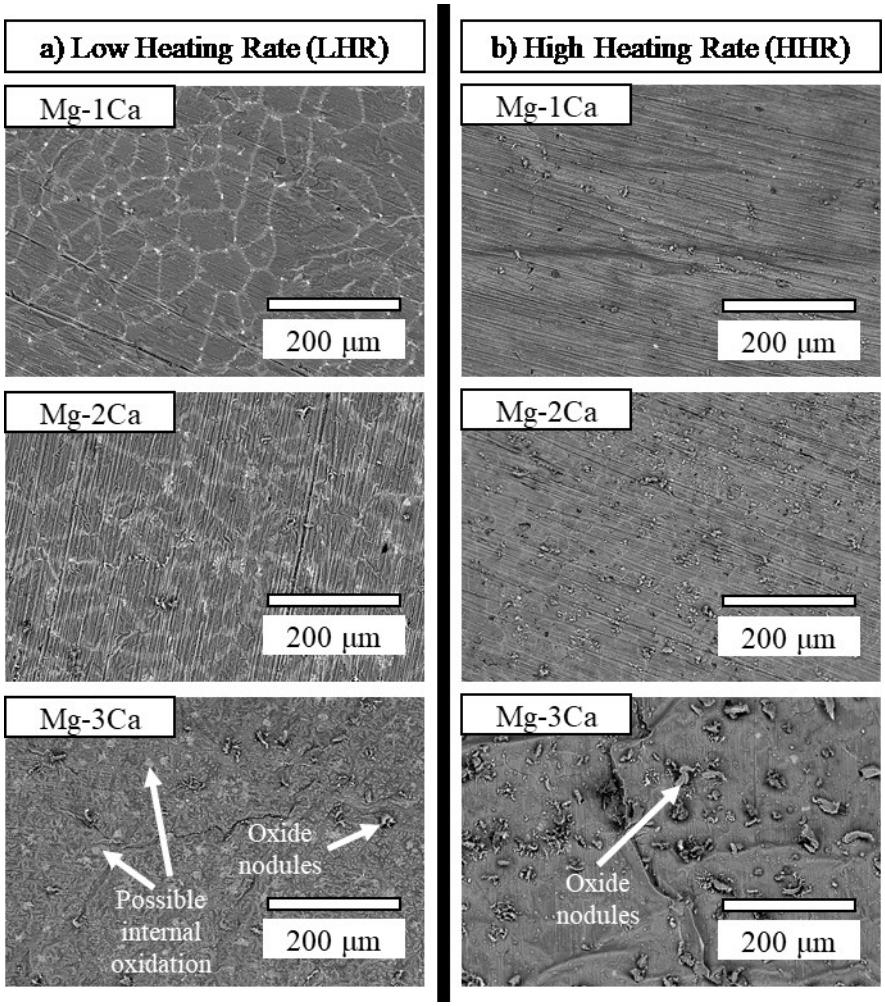

Fig. 5.9. SEM surface micrographs of interrupted ignition test samples at 700 °C.

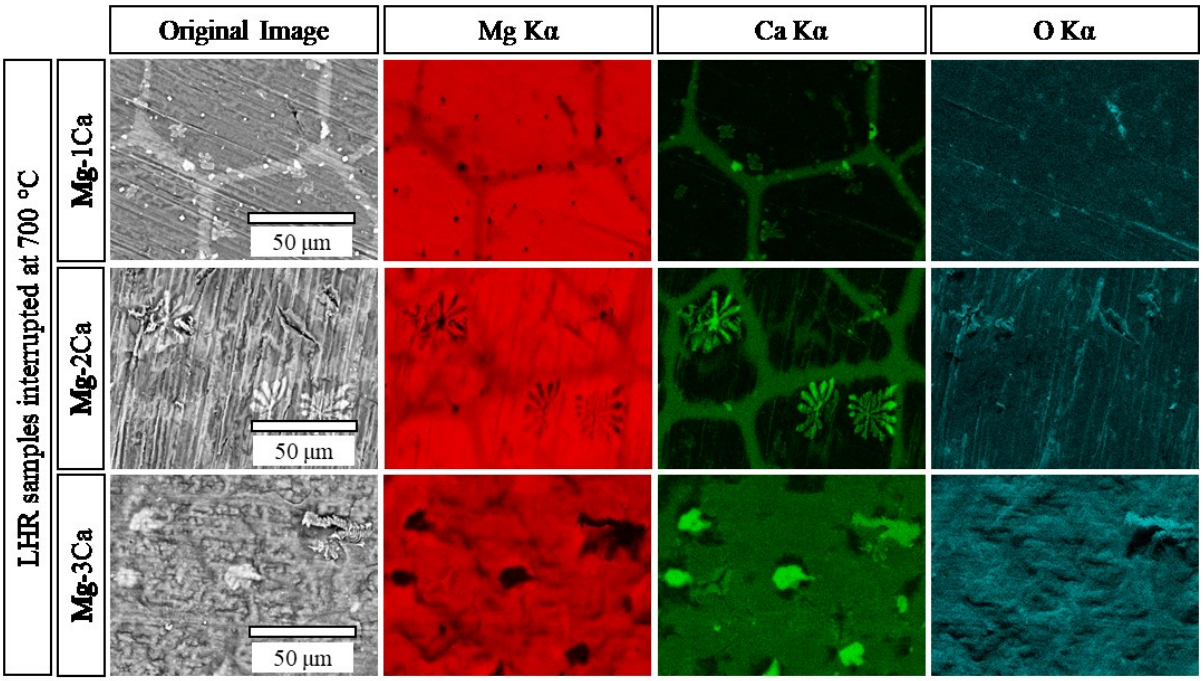

Fig. 5.10. EDS mapping of the Mg-1Ca, Mg-2Ca and Mg-3Ca alloys after an interrupted ignition test at 700°C using an LHR.

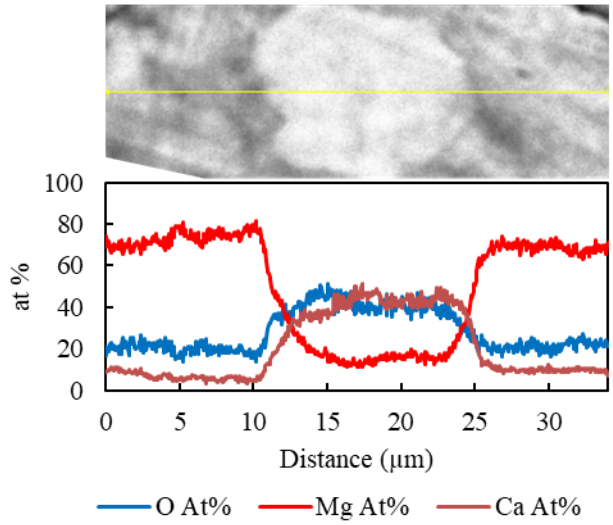

Fig. 5.11. EDS line scan of the Ca-rich particles observed in the Mg-3Ca LHR at 700 °C sample.

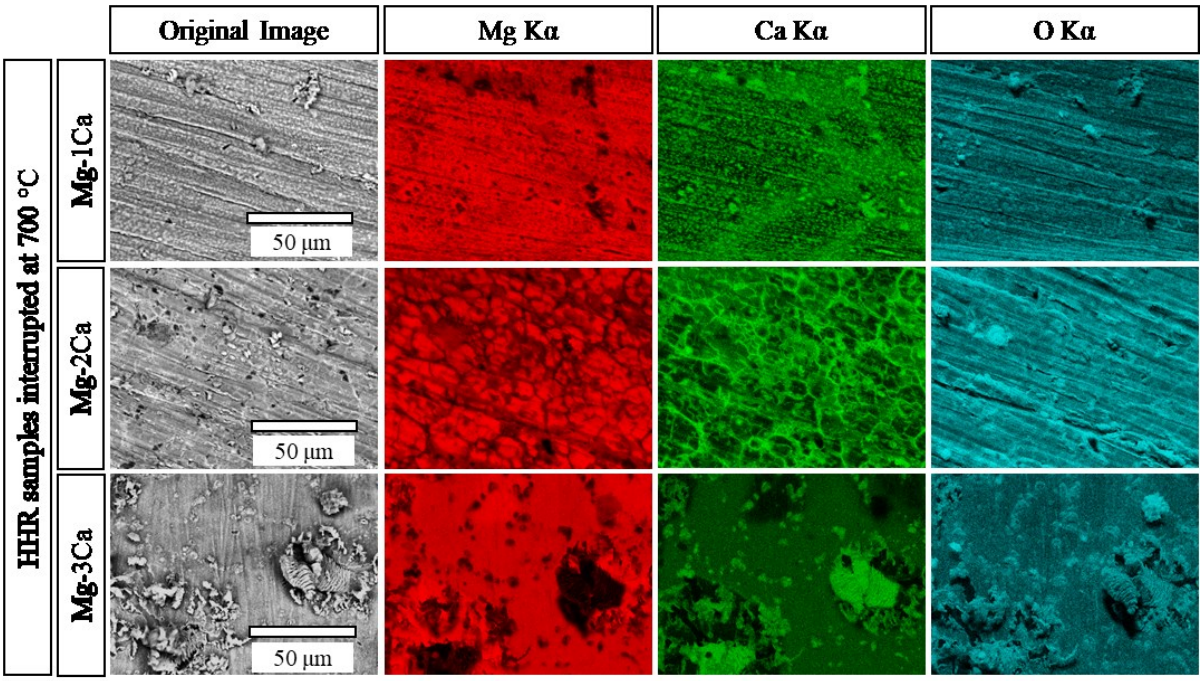

Fig. 5.12. EDS mapping of the Mg-1Ca, Mg-2Ca and Mg-3Ca alloys after an interrupted ignition test at 700°C using an HHR.

5.4. Discussion

This study shows that the ignition temperature of Mg-Ca alloys increases with increasing Ca. However, there is a significant effect on the igntion temperature when a different heating rate is used. Samples heated at a rate of 25 °C/min have an ignition temperature that goes from 655 ºC to 861 °C as Ca increases from 0 to 3 wt%. For the same composition range, using a heating rate of 45 °C/min, the increase in the ignition temperature goes from 658 °C to 787 °C.

Interrupted ignition tests indicate that molten Mg-(1-3)Ca alloys heated using a high heating rate (HHR) up to 700 °C, form a surface scale richer in oxygen than the same alloys heated at a low-heating rate (LHR). It is also seen that the lower tendency for oxide formation on the Mg-1Ca and Mg-2Ca LHR samples, when molten at 700 ºC, is quite striking. When the LHR samples reach 700 °C, the molten alloys seems to be oxidation resistant, having a lower overall O content.

The results indicate that the differences in the behavior of the LHR and HHR samples at 560 °C (in the semi-solid state) are significant. The LHR samples show high amounts of a re-solidified Ca-rich interdendritic phase which is only slightly associated with oxygen (Fig. 5.7a). The HHR samples, unlike the LHR, do not show extensive melting of the interdendritic phase except in the alloy with the highest Ca content; the interdendritic phases seems to have had little time to melt. The solid interdendritic phase, however, is rich in oxygen and exhibits oxide nodule formation, unlike the LHR samples. These particular oxide nodules appear to be formed through internal oxidation rather than through the breakage of the oxide scale. Due to the higher oxygen affinity of Ca, a reduction of the initial MgO scale through the reaction $MgO + Ca = CaO + Mg$ may be taking place at the metal/oxide interface, but these affirmations need to be corroborated through further oxide analysis to confirm the concentration gradient of Ca through the oxide scale. The observations made in the semi-solid state suggest that the molten Ca-rich pools are less prone to oxidation than the solid Ca-rich phase, which forms Ca-rich oxide nodules once the semi-solid state is reached.

Thermodynamic calculations performed using FactSage^{TM}-FTlite (Fig. 5.13), shows that $\Delta G=RTln(P_{O2})$ (Gibbs free energy) for the formation of CaO from the eutectic liquid (Mg-18 wt%Ca) is less negative than ΔG for CaO formation from the solid eutectic Mg_2Ca (Mg-44 wt%Ca). This explains the higher degree of oxidation seen in the solid interdendritic regions of the HHR sample interrupted at 560 °C, compared to the low degree of oxidation seen in the resolidified interdendritic regions of the LHR sample. The solid interdendritic regions of the HHR sample, with a higher tendency for oxidation, would lead to the formation of oxide nodules and an increase in surface temperature. This may result in the development of a thick and brittle oxide scale [34], despite the protective nature of CaO formed over Mg. The increased surface

temperature and the non-protective oxide scale would lead to Mg evaporation which in turn may induce early ignition. The LHR sample, unlike the HHR sample, has a significant amount of molten interdendritic phase that has a lower tendency to oxidation; the LHR samples display an overall lower amount of O at 700 °C, which may result in a lower surface temperature increase (due to MgO/CaO formation) compared to the HHR sample. It is also known that thinner oxides exhibit a lower degree of cracking and are more protective [35]. The low heating rate, therefore, delays the onset of Mg evaporation and ignition.

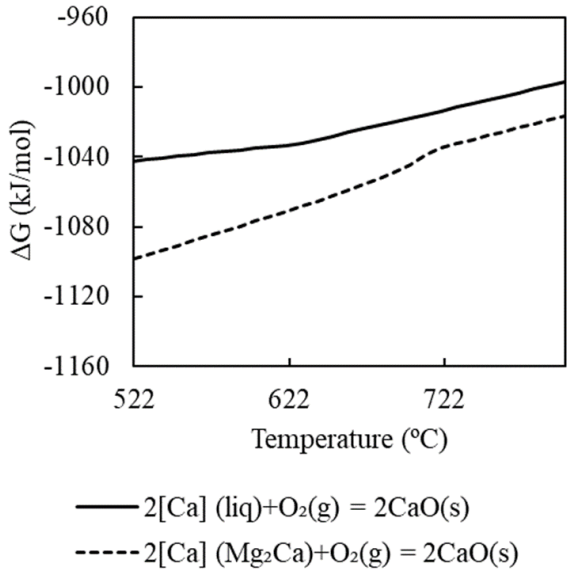

Fig. 5.13. ΔG=RTln(P_{O2}) versus temperature (°C) for the formation of CaO from the eutectic liquid with a composition of Mg-18 wt%Ca (solid line) and from the solid Mg_2Ca with a composition of Mg-44 wt%Ca (dashed line).

This study highlights the important influence of the heating rate and of the differing ΔG for oxide formation of the solid and liquid interdendritic phases in Mg-Ca alloys on the ignition of Mg alloys. It also paves the path to further studies to determine if the heating rate plays a role in Mg alloys with alloying elements other than Ca. It is noted that even under HHR, Ca improves the

ignition temperature of Mg. The characteristics of the formed oxide scale (thickness, composition, etc.) and the re-solidified molten pools, will be discussed in a separate study.

5.5 Conclusions

1. The ignition temperature of Mg-(1-3) wt% binary alloys have been tested using two different heating rates; a low heating rate (LHR) of 25 °C/min and a high heating rate (HHR) of 45 °C/min under a constant flow of extra dry air at a flow rate of 0.9 L/min. For the LHR sample, the ignition temperature increased from 655 °C at 0 wt% Ca to 861 °C at 3 wt% Ca. For the HHR samples, ignition temperature increased from 658 °C to 787 °C as Ca increased from 0 to 3wt%.
2. It was seen that the solid interdendritic regions are more prone to oxidation than the molten interdendritic region. This was explained by the lower ΔG for oxidation from the liquid interdendritic phase compared to the ΔG for oxidation from the solid eutectic Mg_2Ca. This explains the lower degree of oxidation of the eutectic pools in the LHR sample compared to the oxide nodules seen on the solid microconstituents in the HHR samples when interrupted at 560°C.
3. The LHR samples exhibited more eutectic melting in the semi-solid state than the HHR samples. A low heating rate led to lower surface oxidation and to higher ignition temperature, while a high heating rate yielded extensive surface oxidation and lower ignition temperature.

5.6 Acknowledgements

This project was conducted under the financial support of the Natural Sciences and Engineering Research Council of Canada (NSERC) Discovery Grant. The authors thanks Pierre

Vermette from McGill University for his assistance in alloy casting and Sunyong Kwon for his insight in thermodynamics. Luis A. Villegas-Armenta gratefully acknowledges the financial support of CONACYT of Mexico for his scholarship # 410607 and McGill Engineering Doctoral Award program (MEDA).

5.6 References for Chapter 5

[1] F. Czerwinski, "Controlling the ignition and flammability of magnesium for aerospace applications," Corros. Sci., vol. 86, pp. 1-16, 2014.

[2] X. M. Wang, X. Q. Zeng, Y. Zhou, G. S. Wu, S. S. Yao, and Y. J. Lai, "Early oxidation behaviors of Mg–Y alloys at high temperatures," J. Alloys Compd., vol. 460, no. 1-2, pp. 368-374, 2008.

[3] A. Prasad, Z. Shi, and A. Atrens, "Flammability of Mg–X Binary Alloys," Adv. Eng. Mater., vol. 14, no. 9, pp. 772-784, 2012.

[4] P.-y. Lin et al., "Effect of yttrium addition and the powder size on oxide film and powder ignition temperature of AZ91D magnesium alloy," J. Alloys Compd., vol. 481, no. 1-2, pp. 373-378, 2009.

[5] G. Zhang, L. Zhicheng, H. Zhang, and C. Ran, "Ignition-proof mechanism of magnesium alloy added with rare earth La from first-principle study," J. Rare Earths, vol. 30, no. 6, pp. 573-578, 2012.

[6] P.-Y. Lin, H. Zhou, W.-P. Li, W. Li, S.-Z. Zhao, and J.-G. Su, "Effect of yttrium addition on the oxide scale of AM50 magnesium alloy," Corros. Sci., vol. 51, no. 1128–1133, 2009.

[7] P. L.-m. Wu Yu-juan, Zhao Su, Li De-jiang, Huang Fei, Ding Wen-jiang, "Ignition-Proof Properties of a High-Strength Mg-Gd-Ag-Zr Alloy," J. Shanghai Jiaotong Univ., vol. 17, no. 643-647, 2012.

[8] D. S. Aydin, Z. Bayindir, and M. O. Pekguleryuz, "The high temperature oxidation behavior of Mg–Nd alloys. Part II: The effect of the two-phase microstructure on the on-set of oxidation and on oxide morphology," J. Alloys Compd., vol. 584, no. 558–565, 2014.

[9] Z. Na, Z. Zhang, D. Jie, J. Li, and D. Wenjiang, "Selective oxidation behavior of an ignition-proof Mg-Y-Ca-Ce alloy," J. Rare Earths, vol. 31, no. 10, pp. 1003-1008, 2013.

[10] J. F. Fan, C. L. Yang, G. Han, S. Fang, W. D. Yang, and B. S. Xu, "Oxidation behavior of ignition-proof magnesium alloys with rare earth addition," J. Alloys Compd., vol. 509, no. 5, pp. 2137-2142, 2011.

[11] J.-s. Rao, H.-j. Li, and H.-s. Xue, "Ignition-proof mechanism of ZM5 magnesium alloy added with rare earth," J. Cent. South Univ. Technol., vol. 17, no. 1, pp. 28-33, 2010.

[12] D. S. Aydin, Z. Bayindir, M. Hoseini, and M. O. Pekguleryuz, "The high temperature oxidation and ignition behavior of Mg–Nd alloys part I: The oxidation of dilute alloys," J. Alloys Compd., vol. 569, no. 35–44, 2013.

[13] F. Czerwinski, "The early stage oxidation and evaporation of Mg–9%Al–1%Zn alloy," Corros. Sci., vol. 46, no. 377–386, 2004.

[14] X. Zeng et al., "Study on ignition proof magnesium alloy with beryllium and rare earth additions," Sci. Mater., vol. 43, no. 5, pp. 403-409, 2000.

[15] Y.-B. Huang, I.-S. Chung, B.-S. You, W.-W. Park, and B.-H. Choi, "Effect of Be Addition on the Oxidation Behavior of Mg-Ca Alloys at Elevated Temperature," Met. Mater. Int., vol. 10, no. 1, pp. 7-11, 2004.

[16] W. Q. Zeng Xiaoqin, Lu Yizhen, Zhu Yanping, Ding Wenjiang, Zhao Yunhu, "Influence of beryllium and rare earth additions on ignition-proof magnesium alloys," J. Mater. Process. Technol., vol. 112, no. 17-23, 2001.

[17] Q. Tan, N. Mo, B. Jiang, F. Pan, A. Atrens, and M.-X. Zhang, "Combined influence of Be and Ca on improving the high-temperature oxidation resistance of the magnesium alloy Mg-9Al-1Zn," J. Corros. Sci., vol. 122, pp. 1-11, 2017.

[18] Q. Tan et al., "Improved oxidation resistance of Mg-9Al-1Zn alloy microalloyed with 60 wt ppm Be attributed to the formation of a more protective (Mg, Be) O surface oxide," Corros. Sci., vol. 132, pp. 272-283, 2018.

[19] Q. Tan, N. Mo, B. Jiang, F. Pan, A. Atrens, and M.-X. Zhang, "Oxidation resistance of Mg–9Al–1Zn alloys micro-alloyed with Be," Scr. Mater., vol. 115, pp. 38-41, 2016.

[20] D. S. Aydin, Z. Bayindir, and M. O. Pekguleryuz, "The effect of strontium (Sr) on the ignition temperature of magnesium (Mg): a look at the pre-ignition stage of Mg–6 wt% Sr," J. Mater. Sci., vol. 48, no. 23, pp. 8117-8132, 2013.

[21] D. S. Aydin, Z. Bayindir, and M. O. Pekguleryuz, "High Temperature Oxidation Behavior of Hypoeutectic Mg–Sr Binary Alloys: The Role of the Two-Phase Microstructure and the Surface Activity of Sr," Adv. Eng. Mater., vol. 17, no. 5, pp. 697-708, 2015.

[22] M. Sakamoto, S. Akiyama, and K. Ogi, "Suppression of ignition and burning of molten Mg alloys by Ca bearing stable oxide film," J. Mater. Sci. Lett., vol. 16, no. 1048-1050, 1997.

[23] B. S. You, W. W. Park, and I. S. Chung, "The effect of calcium additions on the oxidation behavior in magnesium alloys," Scr. Mater., vol. 42, pp. 1089–1094, 2000.

[24] B.-H. Choi, B.-S. You, W.-W. Park, Y.-B. Huang, and I.-M. Park, "Effect of Ca addition on the oxidation resistance of AZ91 magnesium alloys at elevated temperatures," Met. Mater. Int., journal article vol. 9, no. 4, pp. 395-398, 2003.

[25] L. Jin-Kyu, "Effect of CaO composition on oxidation and burning behaviors of AM50 Mg alloy," Trans. Nonferrous Met. Soc. China, vol. 21, pp. 23-27, 2011.

[26] D.-B. Lee, L.-S. Hong, and Y.-J. Kim, "Effect of Ca and CaO on the high temperature oxidation of AZ91D Mg alloys," Mater. Trans., vol. 49, no. 5, pp. 1084-1088, 2008.

[27] D. B. Lee, "High temperature oxidation of AZ31 + 0.3 wt.%Ca and AZ31 + 0.3 wt.%CaO magnesium alloys," Corros. Sci., vol. 70, no. 243–251, 2013.

[28] J.-K. Lee, H.-H. Jo, and S. K. Kim, "Effet of CaO addition on ignition behavior in molten AZ31 and AZ91D magnesium alloys," Rare Met., vol. 25, no. Special Issue, pp. 155-159, 2006.

[29] S. K. Kim, J.-K. Lee, Y.-O. Yoon, and H.-H. Jo, "Development of AZ31 Mg alloy wrought process route without protective gas," J. Mater. Process. Technol., vol. 187, pp. 757-760, 2007.

[30] N. R. Kumar, J. Blandin, M. Suery, and E. Grosjean, "Effect of alloying elements on the ignition resistance of magnesium alloys," Scr. Mater., vol. 49, no. 3, pp. 225-230, 2003.

[31] F. Czerwinski, "The reactive element effect on high-temperature oxidation of magnesium," Int. Mater. Rev., vol. 60, no. 5, pp. 264-296, 2015.

[32] M. Liu, D. S. Shih, C. Parish, and A. Atrens, "The ignition temperature of Mg alloys WE43, AZ31 and AZ91," Corros. Sci., vol. 54, no. 139–142, 2012.

[33] W. M. Fassell, L. B. Gulbransen, J. R. Lewis, and J. H. Hamilton, "Ignition temperatures of magnesium and magnesium alloys," J. Met., vol. 3, no. 7, pp. 522-528, 1951.

[34] F. Czerwinski, "Oxidation characteristics of magnesium alloys," J. Met., vol. 64, no. 12, pp. 1477-1483, 2012.

[35] Q. Tan, A. Atrens, N. Mo, and M.-X. Zhang, "Oxidation of magnesium alloys at elevated temperatures in air: A review," Corros. Sci., vol. 112, pp. 734-759, 2016.

Chapter 6 - XPS and Electron Microscopy Study of Oxide-Scale Evolution on Ignition Resistant Mg-3Ca Alloy at Low and High Heating Rates

After analyzing the microstructure evolution in a range of Mg-Ca binary alloys through interrupted ignition tests, it was evident that the observed behavior would have an impact in the oxide scale growth and hence the resulting ignition temperature.

In Chapter 6, an in-depth analysis of a Mg-3Ca alloy is presented. Using X-ray Photoelectron Spectroscopy (XPS) and Transmission Electron microscopy (TEM) it was possible to analyze both the growth of the oxide scale formed on the alloy surface and the characteristics of the molten pools observed in Chapter 5.

Abstract

Previous research by the authors has shown that Ca increases the ignition temperature (T_i) of Mg-Ca binary alloys in the 1-3 wt% Ca range with Mg-3Ca exhibiting the highest T_i and revealed the significant effect of heating rate on T_i. In this study, using interrupted tests, X-ray photoelectron microscopy (XPS) and electron microscopy, the evolution of the oxide scale has been investigated on Mg-3Ca alloy heated at a high heating rate (HHR) of 45 °C/min and a low heating rate (LHR) of 25ºC/min towards its ignition temperature. When the alloy is solid, oxidation occurs preferentially from the Mg_2Ca/α-Mg eutectic micro-constituent. In the semi-solid state (560 °C), the solid intermetallic of the HHR sample tends to oxidize internally, forming CaO at the metal/oxide interface. The molten eutectic regions are more oxidation resistant, creating a thin oxide scale of ~100 nm. Due to the shorter time allowed, the less melting occurs in the HHR sample allowing extensive oxidation from the solid eutectic. The LHR, due to its extensive oxidation-resistant melting, leads to the formation of an overall thin oxide scale (~500 nm) that remains protective until ignition at 861ºC. The continued oxidation from the solid eutectic under the HHR leading to an increase in surface temperature and Mg evaporation and a thick non-protective oxide (>1000 nm) results in ignition at a lower temperature of 787 ºC.

6.1 Introduction

The development of magnesium (Mg) alloys for the aerospace industry has gained renewed interest in recent years, due to the lift of the ban imposed on its use for cabin components in commercial aircraft with the update of the SAE aerospace standard AS8049C [1] in 2014. The ban, which was based on the perceived fire risk that these alloys might pose in a post-crash scenario [2], was lifted as a result of an extensive investigation by the Federal Aviation Administration

(FAA) on the flammability of Mg alloys [3]. The results of those investigations showed that the ignition resistance of Mg alloys is highly composition dependent.

Mg is a highly reactive metal which, in its pure form, can ignite at 640 °C with a flame that is difficult to extinguish as it leads to a violent reaction when in contact with water. However, the ignition behavior of Mg can be altered, through the addition of different alloying elements. While aluminum decreases the ignition temperature to 350-450°C, alkaline earth, and rare earth metals are the most promising choices to increase ignition temperature (T_i) of Mg [4-11]. Among these, Ca has been particularly preferred for both commercial and experimental alloys (Table 6.1). On binary Mg-Ca alloys studies, the role of Ca was mainly explained by the formation of a compact and protective oxide scale. It was suggested that the Ca-bearing oxide scale could reduce the diffusion of oxygen towards the molten metal and decrease the volatilization of Mg, thereby increasing the T_i. A previous study by the authors [12], has found that Mg-Ca alloys (2 and 3 wt% Ca) display different ignition temperatures at different heating rates with the Mg-3Ca alloy showing the highest T_i at both heating rates (Table 6.1). In this paper, the evolution and the oxide scale growth of Mg-3Ca alloy during continuous heating at two different heating rates are investigated through X-ray Photoelectron Spectroscopy (XPS) and electron microscopy on samples interrupted at 350 (solid), 560 (semi-solid) and 700 (liquid) °C.

Table 6.1. Summary of Previous studies on the effect of Ca on ignition temperature of Mg alloys

Alloy (wt%)	**T_i (°C)**	**Mechanism**	**Heating rate**	**References**
Mg-4.5Ca	727	Protective oxide scale; outer CaO ; inner MgO-CaO	-	Sakamoto et al. [13]
Mg-0.5Ca	~690	Ca selective oxidation	1.2 °C/s	Chang et al. [14]
Mg-1.9Ca	~800		1.2 °C/s	
Mg-5Ca	727	Increased energy liberation	0.08 °C/s	Shi et al. [15],
*AZ91+5Ca	1000	Protective oxide scale	-	Choi et al. [16]

*AZ91+0.3CaO *AM50+0.3CaO	Increased	Improved stability during casting	-	Lee et al. [17, 18]
*AZ31+0.3(Ca, CaO)	625	Ca ions in the MgO scale and CaO at the surface	Isothermal holding	Lee [19]
*AZ91+2 Ca	819	Oxidation retardation by a dense $CaO+Al_2O_3$ oxide scale	Not specified	Li et al. [20]
*AZ91+6 Ca	869			
Mg-3 Ca	861	The importance of heating rate	0.4 °C/s	Villegas-Armenta et al. [12]
	787		0.7 °C/s	
Mg-2 Ca	841		0.4 °C/s	Villegas-Armenta et al. [12]
	752		0.7 °C/s	

*AZ91 (Mg-9Al-1Zn); AM50 (Mg-5Al-0.3Mn); AZ31 (Mg-3Al-1Zn)

6.2 Experimental Method

A binary Mg-Ca alloy was synthesized using a Norax Induction Furnace (20 kW/5 kHz) at 700 °C, under a protective SF_6/CO_2 protective atmosphere. The materials used were pure Mg supplied by Magnesium Elektron Powders NJ (purity of 99.8%) and Mg-30 wt% Ca master alloy provided by Timinco Metals. The compositions for the cast alloy (Table 6.2) was determined via Inductively Coupled Plasma – Atomic Emission Spectrometry (ICP-AES), performed by the NADCAP certified laboratory Genitest Inc. All compositions are given in weight % unless otherwise specified.

Pure Mg and Mg-Ca master alloy were melted at 690 °C and held at temperature for 15 minutes to allow mixing. The melt was stirred, and the slag was removed prior to casting at 720 °C into 6 mm thick plate-samples using a permanent H13 steel mold coated with boron nitride. Samples of 15 x 15 x 6 mm were machined for ignition tests. The samples were ground with 800 grit SiC paper and polished on the wide face down to 0.05 µm with colloidal silica. A hole of 1.98 mm (5/64 inches) in diameter was drilled in one of the narrower faces to attach a K-type thermocouple covered with a 316L stainless steel sleeve to monitor the temperature in the center

of the sample. The temperature-time profiles were recorded using a Grant Squirrel data logger (2020 series).

Table 6.2. Chemical Composition of the Mg-3Ca alloy

Alloy Designation	**Elements, wt%**							
	Ca	Al	Cu	Fe	Mn	Ni	Si	Mg
Mg – 3 Ca	2.98	0.006	<0.001	0.002	0.005	0.001	0.001	Balance

The samples were then placed in a Lindberg Blue vertical resistance furnace and heated continuously at two different rates of 25°C/ min (Low Heating Rate – LHR) and 45°C/ min (High Heating Rate – HHR) under a constant flow of extra dry air at a rate of 0.9 L/min. For the interrupted ignition tests, once the target temperature was reached, the furnace chamber was flushed with Ar to reduce the sample temperature, and then the sample was removed from the furnace.

The oxidized top surfaces were then analyzed using a Hitachi SU-3500 Scanning Electron Microscope and Energy Dispersive X-ray Spectroscopy (SEM/EDS). A Backscattered Electron (BSE) detector was used to analyze the microstructural features of the samples at different holding times, using an accelerating voltage between 10 to 15 kV. To obtain cross-sections of the oxidized surface, an FIB-SEM Helios Nanolab 660 DualBeam (Focused Ion Beam- Scanning Electron Microscope) was used only to extract the specimens and thin them down to 100 nm. This was done to observe these samples using a FEI Tecnai G^2 F20 200 kV Cryo-Scanning Transmission Electron Microscope (TEM) in both Scanning Transmission Electron Microscopy (STEM) and Selective Area Electron Diffraction (SAED) modes. The results obtained through SAED were compared to simulated diffraction patterns generated in PDF-4+ 2018 diffraction database, making sure that d-

spacings, R ratios, and angles corresponded to the observed pattern, which is obtained from the crystallographic data in [21] for Mg_2Ca. The results were confirmed through the CrysTBox-diffractGUI software [22].

Thermo Scientific K-Alpha X-Ray Photoelectron Spectroscopy (XPS) was used to analyze the oxide scale formed on selected samples from the interrupted ignition tests. A pass energy of 200 eV and a step size of 1 eV were used to determine the chemical composition of the oxide scale (also known as survey spectra), while a high-resolution scanning spectrum was collected using a pass energy of 50 eV and a step size of 0.1 eV to identify the chemical state of an element when needed. A 400 μm diameter region was utilized to obtain a compositional depth profile of the surface by gradually removing layers of oxide scale via an Ar ion beam, with a rate of 0.68 nm/second when Ta_2O_5 is etched, which is the reference material of the instrument for the removal process. The compounds present in our oxide scales have a lower hardness than Ta_2O_5. Hence the actual depth might be more extensive. The sample was etched until a metallic component of the Mg alloy was detected at the deepest etching levels. C was removed from the elemental quantification for clarity of the results. Due to the high oxygen affinity of Mg, the sample surface oxidizes even inside the test chamber between etching steps when a depth profile is performed (vacuum inside the chamber is around $\sim 1 \times 10^{-8}$ bar). Hence, the detection of the Mg metallic component was used to determine the oxide/metal interface, considering that oxygen would always be present during the analysis. Mg KLL region was collected to determine the depth where the Mg photoemission occurs in both metal and oxide states, i.e., an approximate region of the metal/oxide (metal/oxide) interface. The use of the Mg KLL peaks ensures the detection of the metallic component due to the significant chemical shift observed in Mg Auger transitions. The data was analyzed using the Advantage -Thermo Fisher Scientific software. In case of charging, the spectra

were corrected by aligning the binding energy scale with the C1s elemental peak. Certain factors had to be considered to determine the amount of Ca present in the alloy surface. The Ca2p doublet peaks interfere with the Mg KLL Auger region in the range between 360 and 344 eV, leading to complications for both compositional analysis and chemical state assessment. Hence, the Ca2s peak was considered for the compositional analysis, using a relative sensitivity factor (RSF) of 2.106 to determine the amount of Ca present in the surface. The Ca2s peak was collected using a high-resolution scan to confirm the chemical state of this element.

6.3 Results

Interrupted ignition tests were conducted using both an HHR and an LHR for the Mg-3Ca alloy. The tests were interrupted at 350, 560, and 700 °C as these points coincide with the solid, semi-solid, and liquid states of the alloy as per the Mg-Ca phase diagram [23]. Fig. 6.1 presents the full ignition curves of Mg-3.0 Ca at two heating rates and the temperatures at which the tests were subsequently halted during interrupted tests. The evolution of the surface scale was investigated on the as-cast and interrupted-test samples using XPS and SEM/EDS. The surfaces were micro-indented using a Vickers microhardness machine before the interrupted ignition test to follow the evolution of the microstructure.

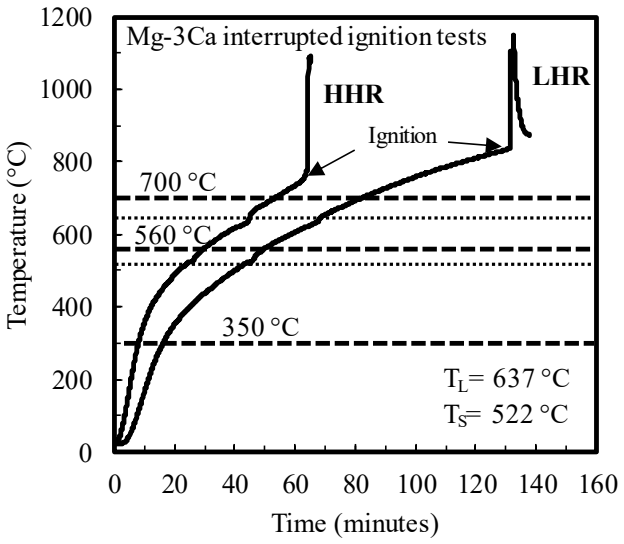

Fig, 6.1. The ignition curves of the Mg-3Ca alloy at HHR and LHR along with the liquidus and solidus temperatures and the interruption temperatures subsequently used.

6.3.1 The Surface Scale of Mg-3Ca Alloy in the As-Cast Condition

SEM image of Fig. 6.2a shows the as-cast top surface of the Mg-3Ca alloy exhibiting α-Mg dendrites and an interdendritic eutectic micro constituent of α-Mg/ Mg_2Ca (C14, $MgZn_2$ type) [22]. The eutectic has lamellar coupled-growth morphology. EDS analysis (Fig. 6.2b) reveals a small amount of Ca present in the α-Mg matrix (~ 0.5 wt% or ~ 0.3 at%) due to the supersaturation of the matrix resulting from the casting process.

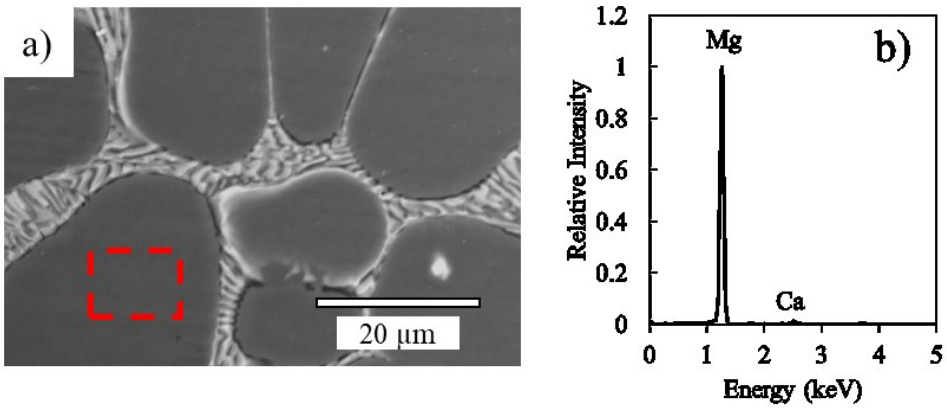

Fig, 6.2. SEM image of the Mg-3Ca cast alloy (a). The red dotted square represents the Mg matrix area analyzed by EDS (b), which contains a small amount of Ca.

XPS depth profiles were performed on the as-cast alloy to determine the initial condition of the alloy surface before the ignition tests. The Mg KLL region for the Mg-3Ca cast sample surface (before any heating) is shown in Fig. 6.3a. Next to these peaks, are the Mg2p region peaks deconvolution for comparison, where the chemical state of Mg is defined through the binding energy of the individual peaks [24]. In Fig. 6.3b, it is possible to observe that, from the first scan up to after an Ar etching of 44 seconds (equivalent to 30 nm on Ta_2O_5), the Mg metallic component is visible at 49.75 eV (FWHM = 0.87) in the cast alloy. Hence, the oxide scale is very thin (~10 nm) and is composed of $MgCO_3$ (BE= 51.83 eV and FWHM = 1.67) at the outermost layer and mostly by MgO (BE = 51.04 eV and FWHM = 1.5) at deeper layers (Fig. 6.3c). Ca content in the cast alloy native oxide scale is negligible. For all the interrupted ignition tests, the Mg KLL region was used to determine the approximate thickness of the oxide scale.

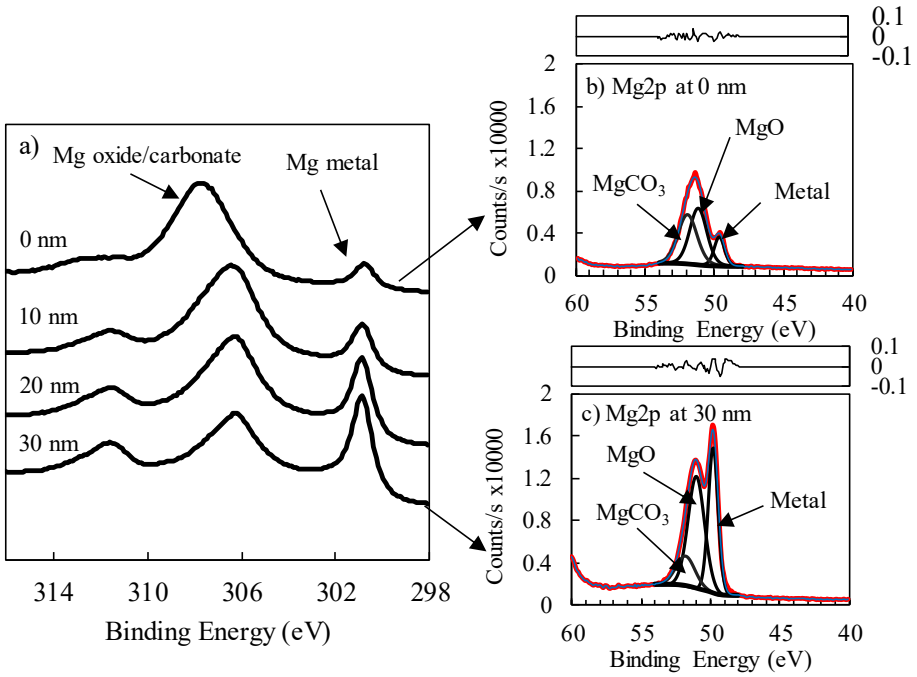

Fig, 6.3. XPS depth profile analysis of the as-cast surface of Mg-3Ca. (a) The Mg KLL transition region and the deconvolution of the Mg2p peak, which indicates the chemical state of Mg at the first (b) and last etching levels (c). The presentation of the Mg KLL peaks allows a more straightforward visualization of the signal coming from the metallic substrate.

6.3.2 The Surface scale of Mg-3Ca Alloy interrupted at 350 °C

Fig. 6.4 shows the microstructures of the LHR (a,b) and HHR (c,d) samples interrupted at 350 °C, along with the initial as-cast surfaces (Fig. 6.4a,c). There is no significant microstructural change between the LHR and HHR samples at this temperature. EDS mapping shows that the eutectic Mg_2Ca is the most oxidized region of the surface in both cases.

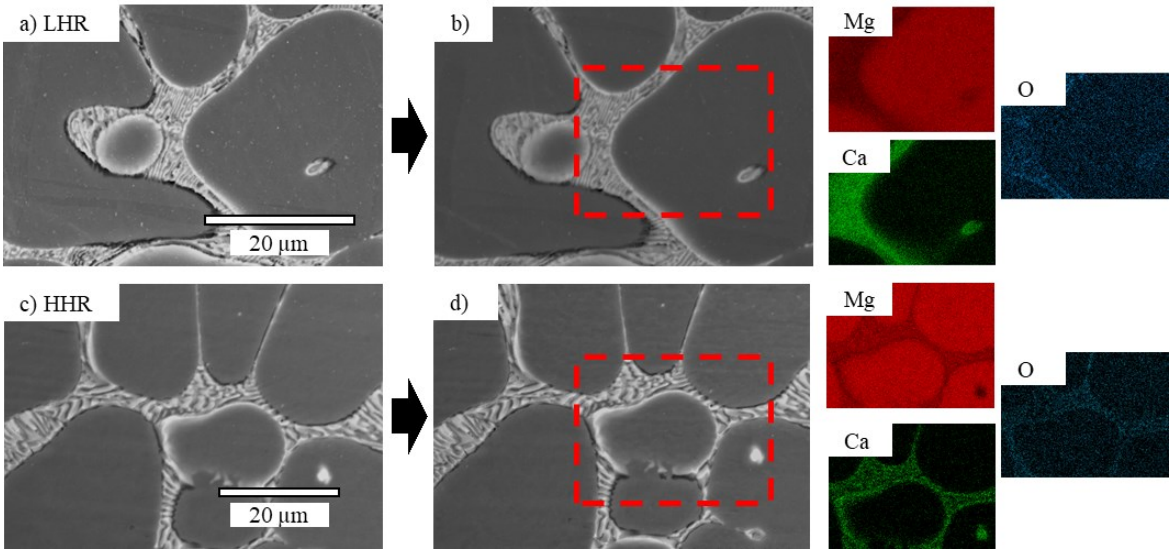

Fig, 6.4. SEM images of Mg-3Ca alloy before (a, c) and after interrupted at 350 °C in ignition test (b, d), comparing LHR and HHR and their EDS analysis.

The XPS analysis of the LHR and HHR Mg-3Ca samples interrupted at 350 °C (Fig. 6.5) indicates the presence of Ca and Mg in the oxide scale. A well-defined metallic Mg peak appears in the LHR depth profile at ~25 nm level, which is the approximate position of the metal/oxide interface. In the HHR sample, the metallic Mg peak has a lower intensity at this level, and the metal/oxide interface in this sample is more likely at the 50-nm level, where a high-intensity Mg metal peak exists. We can see that a thinner oxide scale formed on the LHR when compared to the HHR sample. In both samples, the outermost surface contains a small amount of Ca, but the appearance of the Mg KLL metallic component coincides in both alloys with the highest amount of Ca in the depth profile, indicating that Ca level is higher at the metal/oxide interface than at the outermost surface.

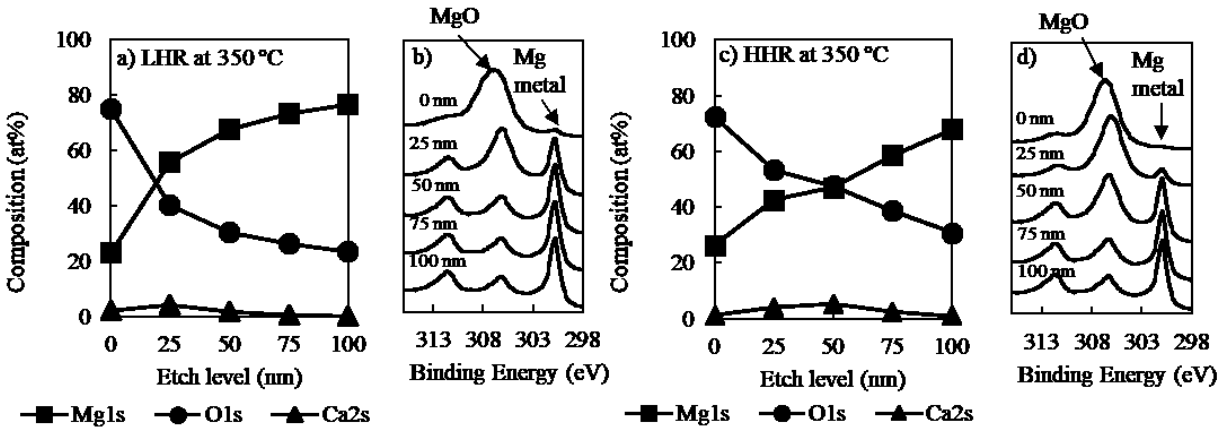

Fig, 6.5. XPS compositional depth profiles on Mg-3Ca sample interrupted at 350 °C. (a, b) LHR and (c, d) HHR. Next to each depth profile is the Mg KLL region, which indicates the etch level where the Mg metallic component is visible.

6.3.3 The Surface Scale of Mg-3Ca interrupted at 560 °C

At 560 °C, the alloy is in the semi-solid state according to the Mg-Ca equilibrium phase-diagram [23] as well as the temperature-time curves in Fig. 6.1. Fig. 6.6 compares the surface of the sample in the as-cast state (a, c) and the re-solidified surface of the same sample interrupted during the ignition test at 560 °C (b, d). The post–interrupted ignition surfaces possess interdendritic regions which appear black and mimic the original cast structure suggesting that the interdendritic phase was selectively oxidized up to this temperature, as observed at 350 °C. The LHR sample exhibits two types of phase morphology on the surface: (a) islands of leaf-like morphology in the interdendritic regions (marked A in Fig. 6b) which indicate that the phase was liquid when the test was interrupted and subsequently re-solidified, and (b) leaf-like features that have serrated edges which are marked B in Fig. 6b. The HHR sample (Fig. 6b) exhibits predominantly the B-type leaf-like features (marked B in Fig. 6d). When observed at lower

magnification through the sample surface, it is found that the coverage of the surface with leaf-like features is more extensive in the LHR sample than in the HHR sample (Fig. 7).

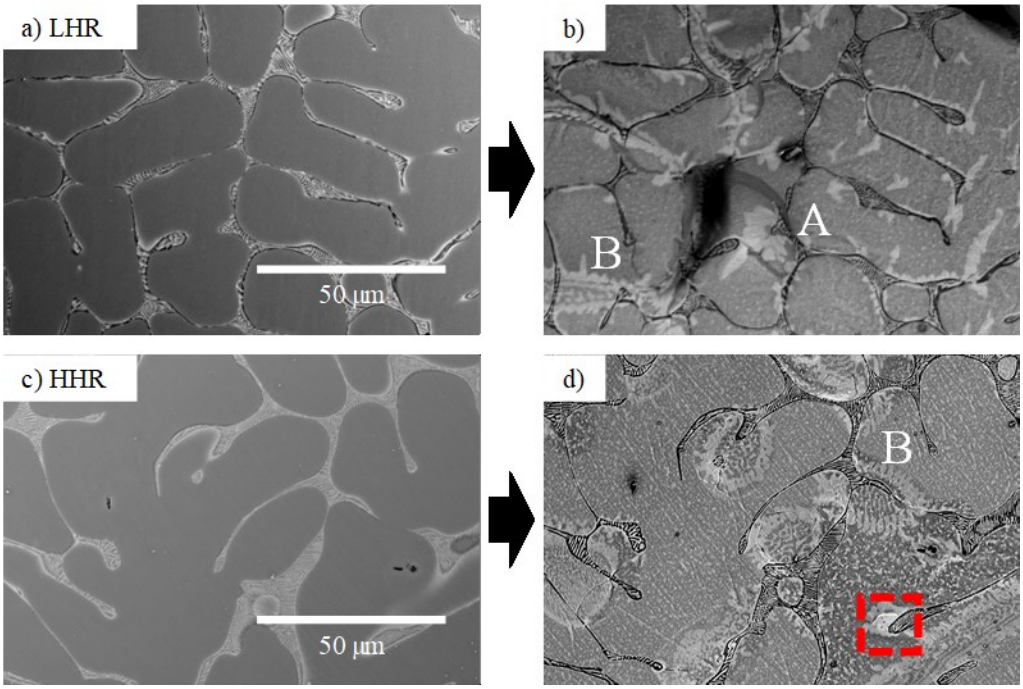

Fig, 6.6. SEM images of Mg-3Ca alloy before (a, c) and after interrupting ignition test at 560 °C (b, d), comparing LHR and HHR. LHR sample has re-solidified island-like phase (labeled A) and leaf-like scaly features (labeled B). The HHR sample exhibits mainly the B-features.

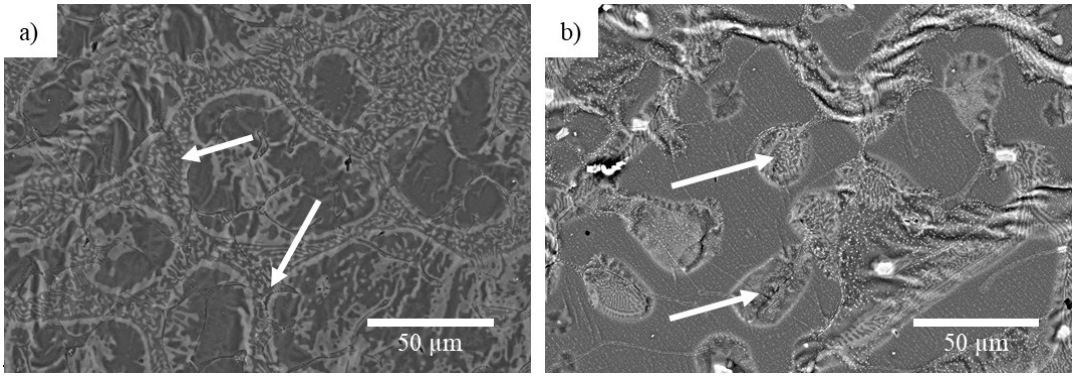

Fig, 6.7. SEM images from the Mg-3Ca LHR and HHR samples interrupted at 560 °C in ignition tests. The leaf-like phase is more evenly distributed on the surface of the (a) LHR sample compared to the (b) HHR sample.

EDS elemental mapping of the LHR and HHR surfaces interrupted at 560 °C are shown in Fig. 6.8. In the LHR sample (Fig. 6.8a), Ca is enriched over both the interdendritic network and over the leaf-like features and oxygen is rich over the Ca-rich interdendritic network (the black features in Fig. 6.6) but not concentrated over the leaf-like Ca phase. In the HHR sample (Fig. 6.8b), Ca is concentrated in the re-solidified phase as well as in Ca-rich particles which are ~3 µm in size. Some of these particles show clear signs of oxidation in the EDS map, indicating that they are oxide nodules. An EDS line scan in Fig. 6.9 shows one of these particles, which is composed mainly by Ca and contain a significant amount of O. The LHR sample does not possess these Ca nodules. These particles were observed in previous work by authors [12], where some of the particles appeared to be signs of internal oxidation, as their well-defined shape is different from the oxide nodules that are clear in the EDS map.

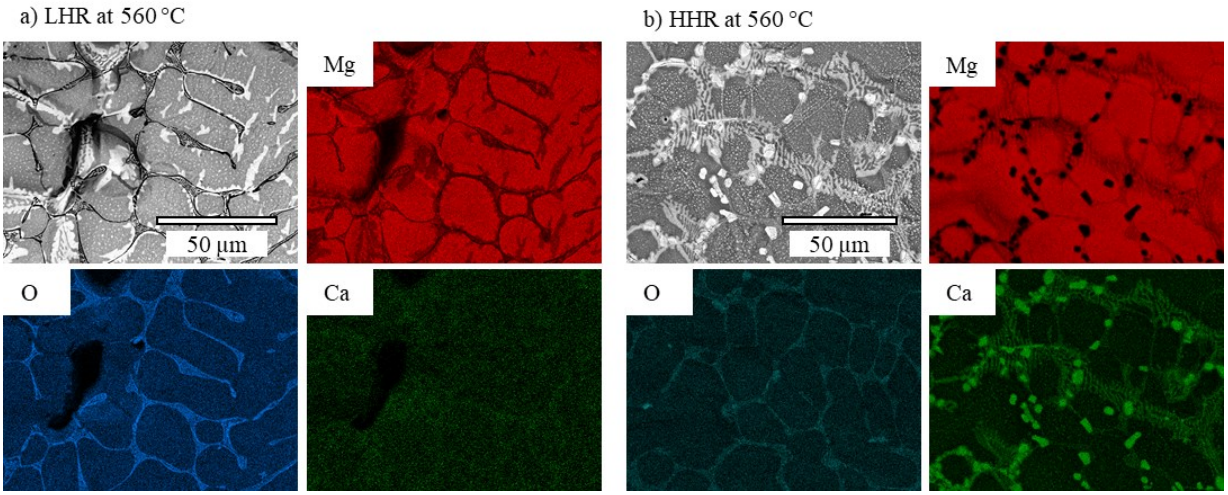

Fig, 6.8. EDS analysis of the (a) LHR sample interrupted at 560°C in ignition test. Ca is present homogeneously over the sample's surface. (b) Fig. 9. HHR sample interrupted at 560°C in ignition test. Several Ca-rich particles are present over the leaf-like phase.

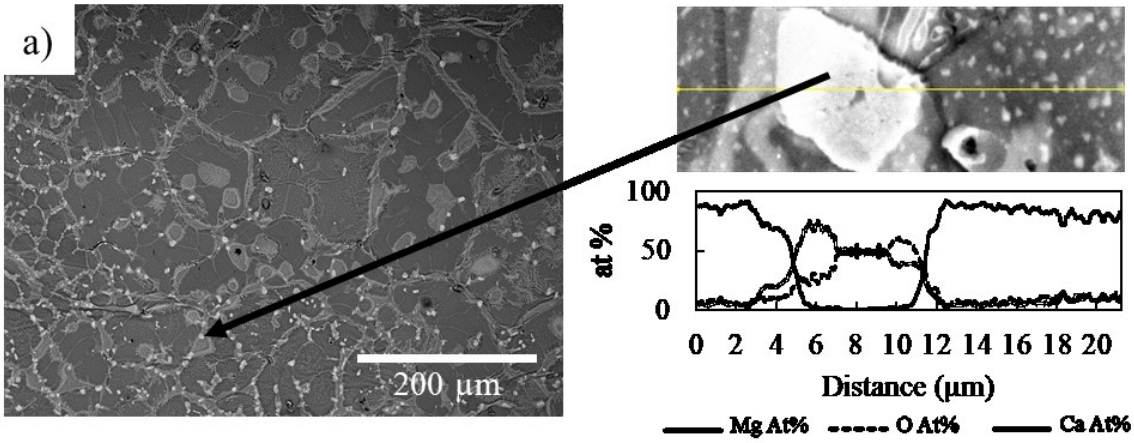

Fig, 6.9. SEM image and EDS line scan over a Ca-rich nodule in Mg-3Ca HHR sample interrupted at 560 °C during the ignition test. The particle contains Ca and O. Some of the particles over the sample appear to be oxidized internally.

The XPS results in Fig. 6.10a show there is a significant increase in Ca through the oxide scale compared to the 350 °C sample. The highest amount of Ca coincides again with the appearance of the Mg metallic component in both samples. At deeper levels in the scale (100-200

nm of etching), the amount of Ca is 50% higher in the HHR compared to the LHR sample. There is no evident difference in the oxide scale thickness at this stage.

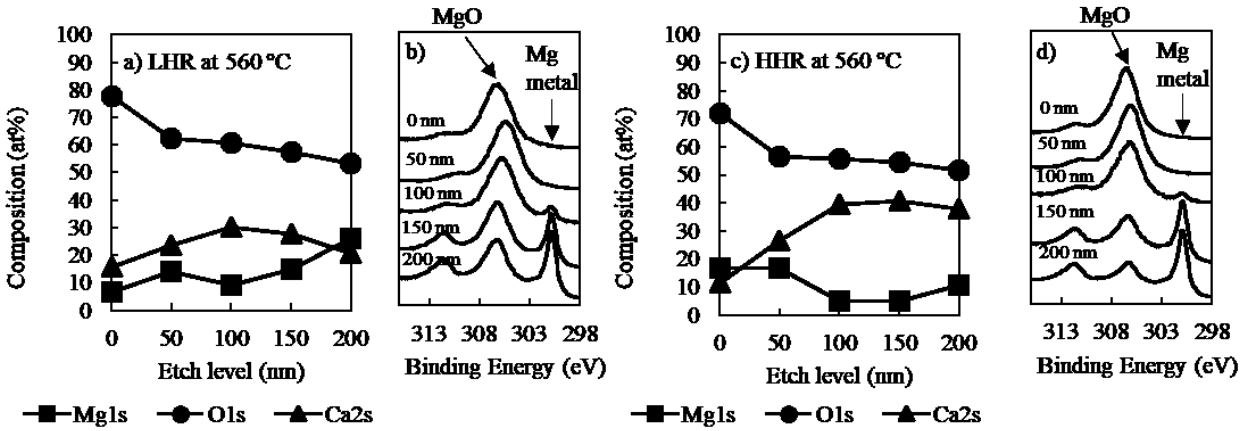

Fig, 6.10. (a-d) XPS compositional depth profiles on Mg-3Ca samples interrupted at 560 °C in ignition test. Next to each depth profile is the Mg KLL region, which indicates the etch level where the Mg metallic component is visible.

To further analyze the re-solidified phases in both sets of samples, cross-sections were extracted from the samples interrupted at 560 °C (Fig. 6.11), using an SEM equipped with a Focused Ion Beam (FIB). Fig. 6.12 shows the TEM bright-field image of the re-solidified phase formed in the (a) LHR sample and the (b) HHR sample. Both samples show some damage caused by the extraction procedure. A point EDS analysis of this phase in both samples shows that the composition is virtually identical, both containing Mg and Ca in the same amounts indicating that the leaf-like phase has the same composition independently of the heating rate. Selected Area Electron Diffraction (SAED) patterns were obtained from both samples (Fig. 6.13) to confirm the identity of the leaf-like phase. For both samples, the phase was identified as Mg_2Ca with an HCP structure (P63/mmc); the phase diffraction patterns were observed at B =$[10\bar{1}0]$ for the LHR sample and B =$[22\bar{4}3]$ for the HHR sample.

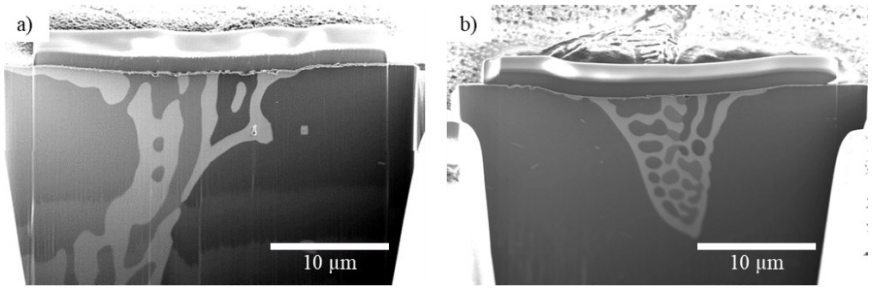

Fig, 6.11. Cross-sections from the Mg-3Ca sample interrupted at 560 °C (a) LHR and (b) HHR, which were extracted using a field emission SEM/FIB.

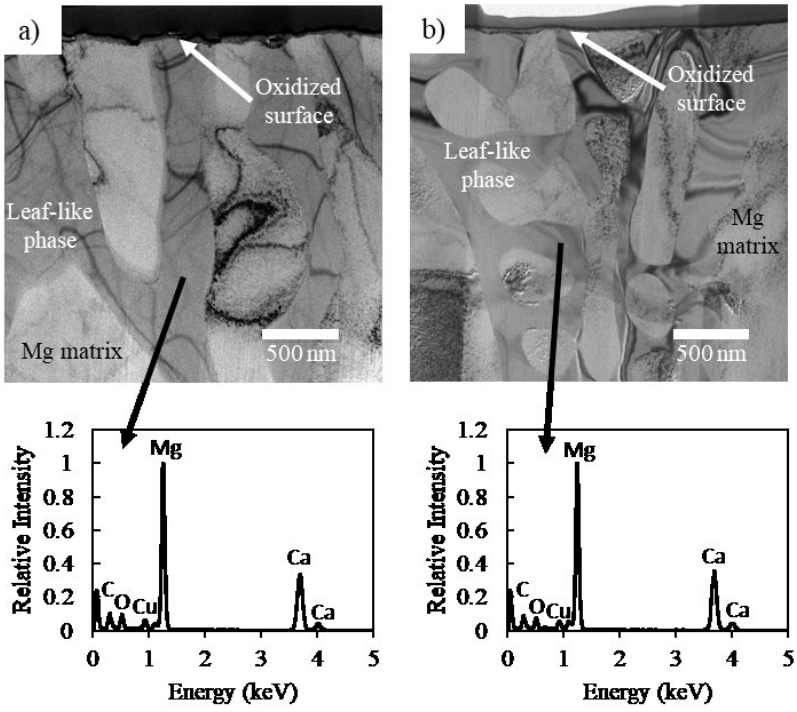

Fig, 6.12. TEM bright-field images of the leaf-like phase observed in the (a) LHR and the (b) HHR sample for the interrupted ignition test at 560 °C. The EDS analysis indicates an identical composition for both phases, suggesting that the same phase is formed in both LHR and HHR samples.

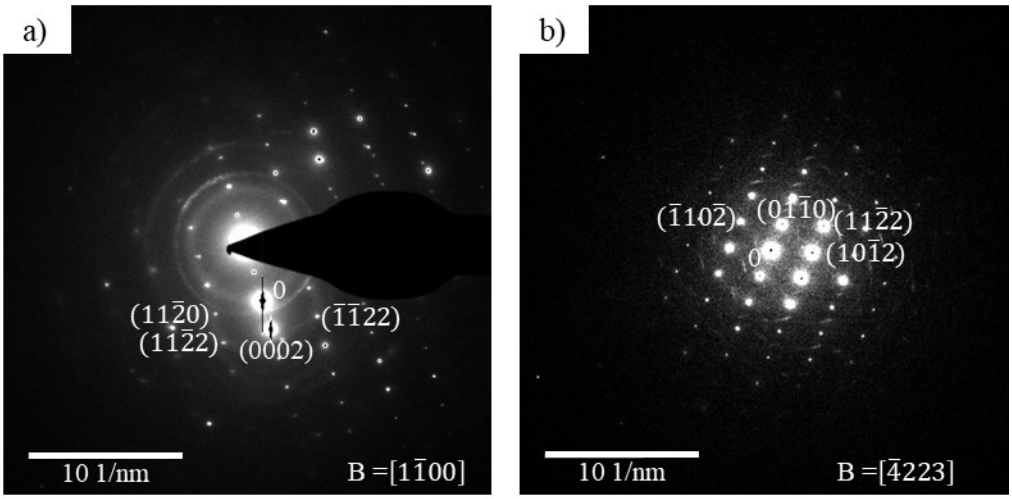

Fig, 6.13. SAED patterns for the leaf-like phase observed in the (a) LHR and the (b) HHR sample for the interrupted ignition test at 560 °C. In both samples, the phase coincides with the Mg_2Ca HCP structure (P63/mmc).

The thickness of the oxide scale formed over this phase is not uniform; it was locally analyzed using STEM/EDS (Fig. 6.14). In the LHR sample (Fig. 6.14a), the oxide scale was ~110 nm in thickness, and in the HHR sample (Fig. 6.14b), it is ~80 nm.

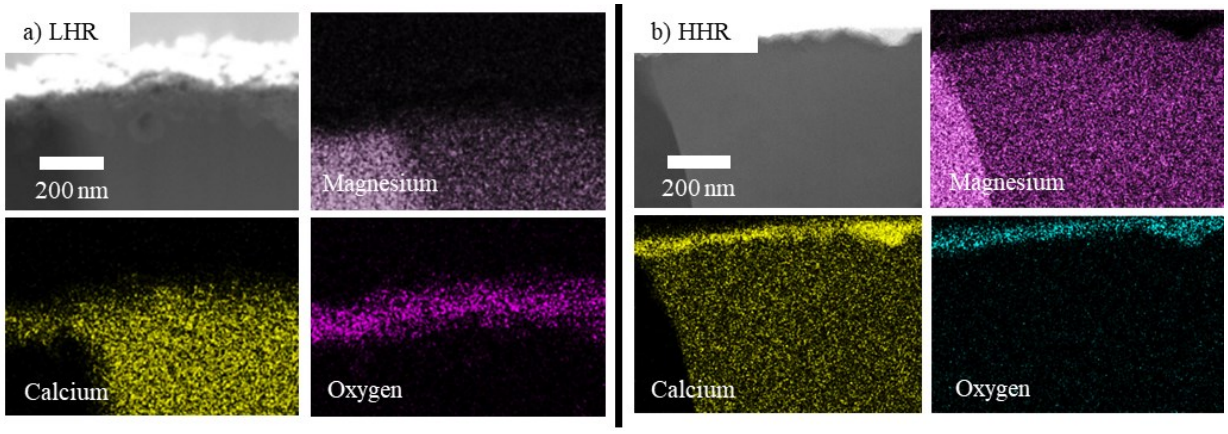

Fig, 6.14. The metal/oxide interface was analyzed using EDS during STEM observation. In both (a) LHR and (b) HHR samples interrupted at 560 °C, the oxide scale formed over the leaf-like phase is rich in Ca.

6.3.4 Mg-3Ca interrupted at 700 °C

At 700 °C, the alloys are liquid according to the phase diagram and the inflection points in the heating curves shown in Fig. 6.1, which also indicates that for both samples, the liquidus has been passed. It is noted that neither the LHR nor the HHR sample have ignited at this temperature. Fig. 6.15 shows the EDS mapping on the surfaces of the LHR and HHR samples, respectively. The surface of the LHR sample is smooth while the HHR sample is rough and full of oxide ridges. The LHR surface (Fig. 6.15a) shows the formation of some internal CaO formation, while both Ca and O are evenly distributed through the surface. On the other hand, the HHR sample shows large CaO ridges that cover the surface, which contains a significant amount of Ca (Fig. 6.15b). The XPS analyses (Fig. 6.16) show that the HHR sample has a much higher amount of Ca than the LHR sample at all levels, confirming the observations made through EDS. Metallic Mg is visible at 500 nm in the LHR sample while it was barely observed at the 1000 nm level in the HHR sample, suggesting a thicker oxide scale compared to the LHR sample.

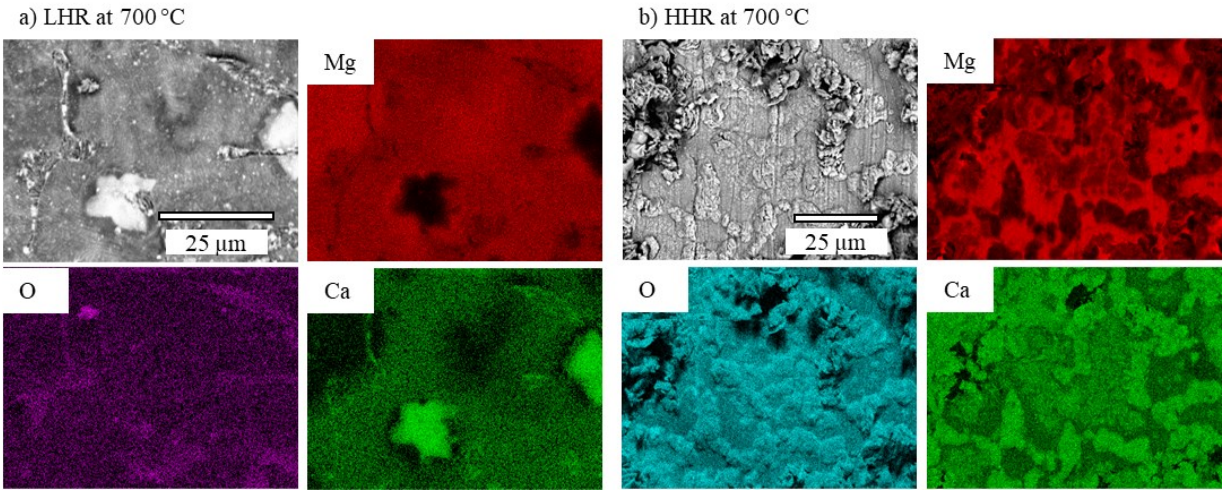

Fig. 6.15. (a) SEM/EDS mapping of Mg-3Ca LHR sample interrupted at 700 °C in ignition test. The leaf-like phase is only partially associated with O on the surface. (b) SEM/EDS mapping of

Mg-3Ca HHR sample interrupted at 700 °C in ignition test. Large oxide ridges are present all over the surface.

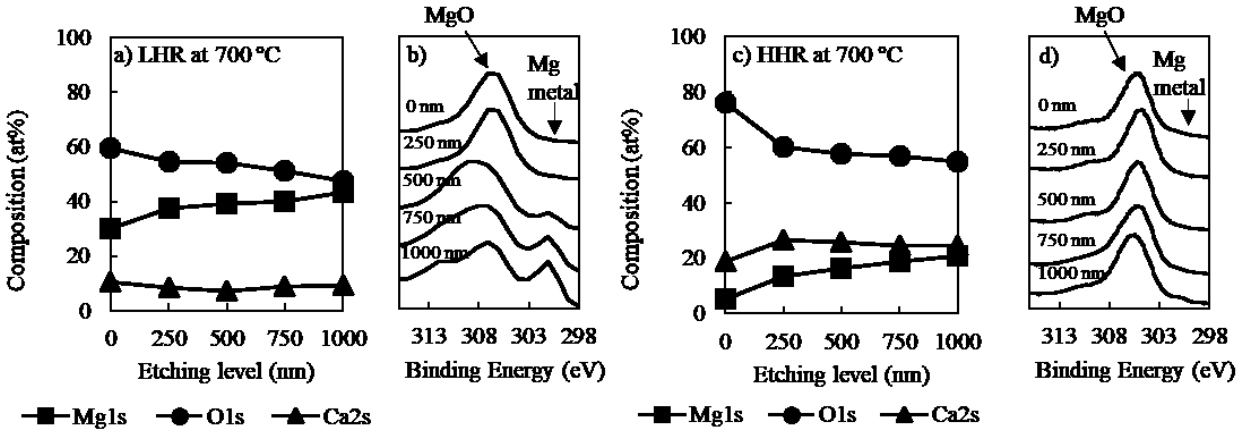

Fig, 6.16. XPS compositional depth profiles from Mg-3Ca LHR (a, b) and HHR (c, d) samples interrupted at 700 °C in ignition test. The Ca level in the HHR scale almost doubles the amount detected using LHR; while the Mg metallic component is not detected in HHR suggesting the formation of a thicker oxide scale.

6.4 Discussion

XPS, SEM/EDS, and TEM analysis revealed differences in the LHR and HHR samples with respect to the evolution of the oxide scale. Table 6.3 summarizes the observations and analyses on the Mg-3Ca LHR and HHR samples after interrupted ignition tests.

Table 6.3. Comparative SEM/EDS, XPS, and TEM results of Mg-3Ca LHR and HHR samples.

Sample		Oxide scale on XPS	Special features
As-cast		10-30 nm thick; $MgCO_3$ top layer, MgO lower layer	
350 °C solid	LHR	25 nm thick, Ca enriched at the metal/oxide interface	
	HHR	50 nm thick, Ca enriched at the metal/oxide interface	

560 °C semi-solid	LHR	100 nm thick, Ca-rich region at the metal/oxide interface	Re-solidified phase
	HHR	100 nm thick, higher Ca at the metal/oxide interface when compared with LHR	Re-solidified phase, CaO nodules
700 °C liquid & near liquid	LHR	500 nm thick, low Ca within the oxide scale	Continuous oxide scale with few CaO nodules
	HHR	Thicker than 1000 nm, high Ca within the oxide scale	CaO ridges on the surface

6.4.1 Solid-state heating interrupted at 350^{o} C

The sequence of oxidation from a 2-phase alloy is usually difficult to predict [25, 26], however, XPS results show that the initial oxide scale is mainly composed of MgO at early stages using either heating rate. XPS results also show that MgO content is more significant at the outermost surface at 350 °C, while the metal/oxide interface is enriched in Ca. The mechanism can be explained as follows: Once the initial MgO scale forms, its growth is controlled by ion diffusion. Diffusion in MgO is extrinsic and depends mostly on the concentration of vacancies, where diffusion of Group II A elements will be inversely proportional to the ionic radius of a given element [27]. Hence, Ca ions will have slower diffusion rates in MgO compared to its cation self-diffusion, causing further oxide growth being dominated mainly by Mg ion diffusion. The slower heating in the LHR sample provides enough time for Ca to distribute through the oxide scale compared to the HHR. XPS results confirm that a higher amount of Ca has accumulated at the metal/oxide interface in the HHR compared to the LHR. Thermodynamically, Ca in the phases of the alloy oxidizes selectively due to the higher oxygen affinity of Ca (ΔG= -1138.65 kJ/O_2 mol for CaO formation at 350 °C) compared to Mg (ΔG=-1068.27 kJ/O_2 mol for MgO formation at 350 °C); where both MgO and CaO form the same rocksalt crystal structure. The even distribution of Ca in the oxide scale would reduce the Mg oxidation at the surface of the LHR sample compared

to the HHR. Profuse MgO formation is enhanced on the HHR surface, leading to a thicker oxide (50 nm) compared to the LHR (25 nm). SEM/EDS also reveals that the Mg_2Ca/α-Mg eutectic micro constituent oxidizes more than the matrix.

6.4.2 Semi-Solid state interrupted at 560 °C

The first region to liquefy in the semi-molten alloy is the low-melting interdendritic eutectic micro constituent (Mg_2Ca + α-Mg) which is rich in Ca (17 wt% Ca). The eutectic melting is evidenced by the leaf-like dendritic morphology formed when the molten eutectic solidifies back into the Mg_2Ca/α-Mg phases upon cooling. Since the interdendritic eutectic region melts first, the remaining solid in the semi-solid alloy is mainly the α-Mg which, is already covered with an oxide scale. Oxidation in the semi-solid surface occurs from three phases: (i) the solid α-Mg, (ii) solid eutectic, and (iii) the eutectic liquid pools.

Our previous results [12] showed that the ΔG for the oxidation from the solid Mg_2Ca is more negative than the ΔG for the oxidation of the eutectic liquid pools (at 18 wt% Ca) in the semi-solid range, as shown in Fig. 6.18. The CaO nodules observed in the HHR sample are indeed internal oxidation caused by the reduction of MgO by Ca, as the XPS results indicate a significant amount of Ca at the metal/oxide interface compared to regions close to gas/oxide interface. Mg has a lower oxygen affinity when compared to Ca. Hence the MgO reduction by Ca is an energetically favorable reaction. This would promote the selective oxidation of the solid Mg_2Ca eutectic phase in the HHR sample. The re-solidified eutectic pool regions possess a very thin oxide scale which is mainly Ca, observed in STEM. Hence despite being also internally oxidized, the amount of Ca at the metal/oxide interface is lower when compared to the HHR sample.

Previous research suggested [28] that the melting of eutectic compounds and consequent formation of liquid pools in the semi-solid stage may lead to an increase in Mg evaporation; this

would imply that the eutectic pools decrease ignition temperature. This is contrary to our results, where these eutectic pools are resistant to oxidation and promote an increase in ignition temperature, especially when the Ca content is above 1.5 wt% [12].

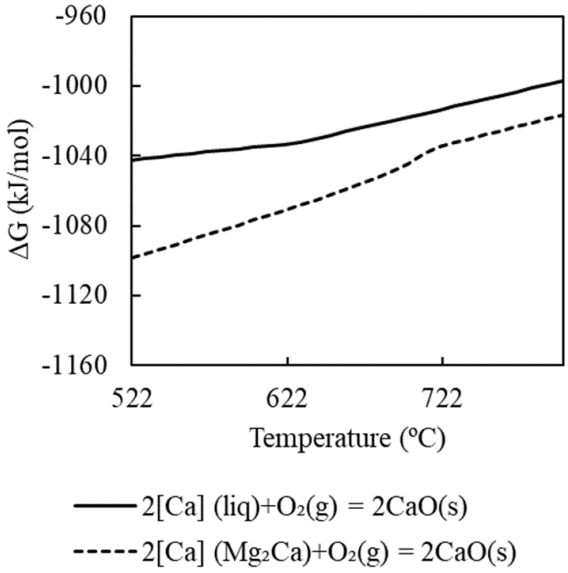

Fig, 6.17. ΔG=RTln(P_{O2}) versus temperature (°C) for the formation of CaO from the eutectic liquid with a composition of Mg-18 wt%Ca (solid line) and from the solid Mg_2Ca with a composition of Mg-44 wt%Ca (dashed line). [12].

6.4.3 Liquid State Interrupted at 700 °C

When the HHR sample reaches 700 ºC, the surface displays a thick mottled oxide. It is reported that a sample having a thicker oxide shows uneven regions on the oxide scale, which are usually found to be at interdendritic phase regions in Mg alloys [29]. A thick oxide also leads to a high surface temperature stemming from the extensive exothermic reaction. Extensive oxidation, despite being caused by the formation of CaO, results in an increase in surface temperature that leads lead to enhanced Mg evaporation; oxide scale cracking would expose the Mg vapor to oxygen, leading then to ignition. The fully liquid LHR sample has a lower degree of oxidation and

by consequence a lower increase in surface temperature. Its thinner oxide scale is compact and leads to higher ignition temperature. XPS shows a higher Ca content in the oxide scale in the HHR sample, but because the scale is thick (1000 nm compared to LHR sample with an oxide scale of 500nm), it provides less protection.

The coverage of the sample surface with the oxidation-resistant eutectic liquid is the main factor improving the ignition resistance of Mg-3Ca alloy. The protective nature of the CaO scale is not the only factor to consider, since when the oxide scale thickens it is prone to cracking, and fails despite a high Ca content. The main driving factor seems to be the competition between oxidation of the solid eutectic micro constituent and its melting. The LHR of 25 °C/min increases the molten Mg_2Ca coverage and increases the ignition temperature to 861ºC, while the HHR (45 °C/min), due to the limited time available for melting, hinders the molten eutectic coverage of the surface and increases the degree of Ca internal oxidation from the solid interdendritic phase which results in a lower ignition temperature of 787 ºC. In other words, faster heating promotes the Mg_2Ca/α-Mg micro constituent oxidation forming a thick, cracked non-protective surface scale, while slow heating promotes the formation of liquid surface which is more resistant to oxidation than the solid surface and to the formation of a thin protective oxide scale.

6.5 Conclusions

Based on previous results of the authors [22], the ignition temperature of the Mg-3Ca alloy is influenced by the heating rate. The ignition temperature is 861°C using a heating rate of 25 °C/min (LHR) and 787 °C using a heating rate of 45 °C/min (HHR). In this study, Mg-3Ca samples from interrupted ignition tests performed using these two heating rates (25 °C/min and 45 °C/min), were analyzed via XPS, SEM/EDS and TEM to understand the evolution of their oxide scales. The interrupted ignition tests allowed to determine the following conclusions:

1. XPS study shows that the HHR sample forms a thicker oxide than the LHR sample. The oxide thickness in the HHR sample increases 50 nm to 1000 nm as the temperature increases to 700 °C. The corresponding increase in oxide thickness of the LHR sample is from 25nm to 500nm. SEM/EDS reveals that the oxide on the HHR sample is not protective, exhibiting a mottled appearance, oxide ridges, and oxide nodules. The LHR sample has a continuous and uniform oxide scale.
2. XPS shows that Ca enriches the metal/oxide interface and that the Ca content of the HHR sample is higher than the Ca level in the LHR sample at 700 °C.
3. SEM/EDS shows that at 560 °C, the coverage of the molten eutectic pools is widespread in the LHR sample; while this coverage is limited in the HHR sample, along with the formation of Ca-rich oxide nodules.
4. The molten eutectic micro constituent forms a thinner oxide compared to the solid eutectic with a thicker oxide and oxide nodules. This is supported by previously presented thermodynamic calculations, that shows that the liquid eutectic has a lower tendency to oxidation than the solid eutectic.
5. The formation of a thick non-protective oxide when an HHR is used, is the main factor that would lead to an increase in surface temperature, Mg evaporation and to a reduced ignition temperature (787 °C) of the Mg-3Ca alloy, compared to the same alloy heated using an LHR which has a higher ignition temperature (861 °C).

6.6 Acknowledgements

This project was conducted under the financial support of the Natural Sciences and Engineering Research Council of Canada (NSERC) Discovery Grant. The authors thanks Pierre Vermette from McGill University for his assistance in alloy making and casting. Luis Angel

Villegas-Armenta gratefully acknowledges the financial support of CONACYT of Mexico for the scholarship 410607 and McGill Engineering Doctoral Award (MEDA).

6.7 References for Chapter 6

[1] Performance Standard for Seats in Civil Rotorcraft, Transport Aircraft, and General Aviation Aircraft, 2015.

[2] Y.-H. Chang and H.-H. Yang, "Aviation occupant survival factors: An empirical study of the SQ006 accident," Accid. Anal. Prev., vol. 42, no. 2, pp. 695-703, 2010.

[3] T. Marker, "Development of a Laboratory—Scale Flammability Test for Magnesium Alloys Used in Aircraft Seat Construction," Federal Aviation Administration, DOT/FAA/TC-13/52, 2014.

[4] D. S. Aydin, M. Hoseini, and M. O. Pekguleryuz, "Understanding the high temperature oxidation and ignition behaviour of two-phase Mg–Nd alloys and a comparison to single phase Mg–Nd," Philos. Mag., vol. 95, no. 3, pp. 259-274, 2015.

[5] F. Jianfeng, C. Zhiyuan, Y. Weidong, F. Shuang, and X. Bingshe, "Effect of yttrium, calcium and zirconium on ignition-proof principle and mechanical properties of magnesium alloys," J. Rare Earths, vol. 30, no. 1, 2012.

[6] J. F. Fan, C. L. Yang, G. Han, S. Fang, W. D. Yang, and B. S. Xu, "Oxidation behavior of ignition-proof magnesium alloys with rare earth addition," J. Alloys Compd., vol. 509, no. 5, pp. 2137-2142, 2011.

[7] P.-y. Lin, H. Zhou, W. Li, W.-p. Li, N. Sun, and R. Yang, "Interactive effect of cerium and aluminum on the ignition point and the oxidation resistance of magnesium alloy," Corros. Sci., vol. 50, no. 9, pp. 2669-2675, 2008.

[8] A. Prasad, Z. Shi, and A. Atrens, "Influence of Al and Y on the ignition and flammability of Mg alloys," Corros. Sci., vol. 55, pp. 153-163, 2012.

[9] S. Zhao, H. Zhou, T. Zhou, Z. Zhang, P. Lin, and L. Ren, "The oxidation resistance and ignition temperature of AZ31 magnesium alloy with additions of La2O3 and La," Corros. Sci., vol. 67, pp. 75-81, 2013.

[10] D. S. Aydin, Z. Bayindir, and M. O. Pekguleryuz, "The effect of strontium (Sr) on the ignition temperature of magnesium (Mg): a look at the pre-ignition stage of Mg–6 wt% Sr," J. Mater. Sci., vol. 48, no. 23, pp. 8117-8132, 2013.

[11] Z. Na, Z. Zhang, D. Jie, J. Li, and D. Wenjiang, "Selective oxidation behavior of an ignition-proof Mg-Y-Ca-Ce alloy," J. Rare Earths, vol. 31, no. 10, pp. 1003-1008, 2013.

[12] L. A. Villegas-Armenta, R. A. L. Drew, and M. O. Pekguleryuz, "The Ignition Behavior of Mg-Ca binary alloys; The Role of Heating Rate," 2019.

[13] M. Sakamoto, S. Akiyama, and K. Ogi, "Suppression of ignition and burning of molten Mg alloys by Ca bearing stable oxide film," J. Mater. Sci. Lett., vol. 16, no. 1048-1050, 1997.

[14] S.-Y. Chang, M. Matsushita, H. Tezuka, and A. Kamio, "Ignition prevention of magnesium by simultaneous addition of calcium and zirconium," Int. J. Cast Met. Res., vol. 10, no. 6, pp. 345-351, 1998.

[15] T.-S. Shih, J.-H. Wang, and K.-Z. Chong, "Combustion of magnesium alloys in air," Mater. Chem. Phys., vol. 85, no. 2, pp. 302-309, 2004.

[16] B.-H. Choi, B.-S. You, W.-W. Park, Y.-B. Huang, and I.-M. Park, "Effect of Ca addition on the oxidation resistance of AZ91 magnesium alloys at elevated temperatures," Met. Mater. Int., journal article vol. 9, no. 4, pp. 395-398, 2003.

[17] J.-K. Lee, H.-H. Jo, and S. K. Kim, "Effet of CaO addition on ignition behavior in molten AZ31 and AZ91D magnesium alloys," Rare Met., vol. 25, no. Special Issue, pp. 155-159, 2006.

[18] L. Jin-Kyu, "Effect of CaO composition on oxidation and burning behaviors of AM50 Mg alloy," Trans. Nonferrous Met. Soc. China, vol. 21, pp. 23-27, 2011.

[19] D. B. Lee, "High temperature oxidation of AZ31 + 0.3 wt.%Ca and AZ31 + 0.3 wt.%CaO magnesium alloys," Corros. Sci., vol. 70, no. 243–251, 2013.

[20] F. Li et al., "Development of non-flammable high strength AZ91+ Ca alloys via liquid forging and extrusion," Mater. Des., vol. 99, pp. 37-43, 2016.

[21] O. Reckeweg, C. Lind, A. Simon, and F. J. DiSalvo, "Reactions of alkaline earth metals and nitrogen in sealed niobium ampoules: the formation of MgZn2 type intermetallic phases in the presence of nitrogen and the new compound Ba5 [NbN4] N," J. Alloys Compd., vol. 384, no. 1-2, pp. 98-105, 2004.

[22] M. Klinger, "More features, more tools, more CrysTBox," J. Appl. Crystallogr., vol. 50, no. 4, 2017.

[23] A. A. Nayeb-Hashemi and J. B. Clark, "The Ca−Mg (Calcium-Magnesium) system," Bull. Alloy Phase Diagrams, journal article vol. 8, no. 1, pp. 58-65, February 01 1987.

[24] V. Fournier, P. Marcus, and I. Olefjord, "Oxidation of magnesium," Surf. Interface Anal., vol. 34, no. 1, pp. 494-497, 2002.

[25] B. Bobryshev and Y. P. Aleksandrova, "Ignition of magnesium and its alloys," Met. Sci. Heat Treat., vol. 30, no. 3, pp. 219-222, 1988.

[26] D. S. Aydin, Z. Bayindir, and M. O. Pekguleryuz, "High Temperature Oxidation Behavior of Hypoeutectic Mg–Sr Binary Alloys: The Role of the Two-Phase Microstructure and the Surface Activity of Sr," Adv. Eng. Mater., vol. 17, no. 5, pp. 697-708, 2015.

[27] J. A. Van Orman and K. L. Crispin, "Diffusion in Oxides," Rev. Mineral. Geochem., vol. 72, no. 1, pp. 757-825, 2010.

[28] Q. Tan, A. Atrens, N. Mo, and M.-X. Zhang, "Oxidation of magnesium alloys at elevated temperatures in air: A review," Corros. Sci., vol. 112, pp. 734-759, 2016.

[29] M. Ascencio, M. Pekguleryuz, and S. Omanovic, "An investigation of the corrosion mechanisms of WE43 Mg alloy in a modified simulated body fluid solution: The influence of immersion time," Corros. Sci., vol. 87, no. Supplement C, pp. 489-503, 2014/10/01/ 2014.

Chapter 7 - The Effect of Heating Rate on the Ignition-Resistance of Mg-Sr Alloys

After analyzing the ignition behavior of Mg-Ca binary alloys, four Mg-Sr binary alloys were tested under the same conditions presented in Chapters 5 and 6. Also, interrupted ignition tests were made to analyze the solid, semi-solid and liquid stages of a Mg-2.4 Sr alloy. The surface of the samples obtained were analyzed using Scanning Electron Microscopy (SEM) and X-ray Photoelectron Spectroscopy (XPS). Transmission Electron Microscopy (TEM) was employed to analyze the cross-section of the samples during the semi-solid state (620 °C), which displayed significant differences when the two heating rates used.

Abstract

The ignition resistance of a series of Mg-Sr alloys (Mg-1.1Sr, Mg-1.5Sr, Mg-2.14Sr, and Mg-2.4Sr) is tested using two different heating rates. The results indicate that the ignition temperature of Mg-Sr alloys is strongly dependant on the heating rate. Samples heated using a high heating rate ignite close the melting temperature of each alloy. On the other hand, the ignition temperature increases between 100 and 150 °C when a low heating rate is used. The formation of Sr-rich molten pools during the semi-solid state promotes the development of a thin and protective oxide scale, thanks to the surface-active behavior of Sr. Without the formation of these pools, the oxide scale grows laterally from the interdendritic region, becoming thicker and generating greater internal stresses. When the liquid state is reached, and the oxide scale fails, molten Mg is exposed to the atmosphere with consequential ignition.

7.1 Introduction

Rare-earth metals and alkaline-earth metals such as Ca or Be have been shown to increase the ignition temperature of Mg alloys [1-25]. Sr, another alkaline earth metal, also has the potential to affect the ignition behavior of Mg. The effect of Sr in Mg ignition resistance and high-temperature oxidation was reported by Aydin et al. [7, 26], where the ignition temperature of pure Mg was increased by ~200 °C when 6 wt% Sr is added. The authors attributed this to the surface-active behavior of Sr in Mg, which reduces the amount of Mg present in the surface, hence slowing down the evaporation and ignition of Mg. This surface-active behavior was previously observed by Ozdemir et al. [27] in molten Al-Mg alloys, where Sr enriched the surface below the first MgO scale; preventing the formation of spinel crystals and hence improving the oxidation resistance. A similar effect was observed by Dennis et al. [28] in molten 356 and 413 Al alloys, where Sr forms protective compounds below the MgO scale. Sr is also a surface-active element in molten Mg due

to its larger Wigner-Seitz Radius (WSR) [29] of 4.5 a.u. [30]. Mg has a WSR of 2.66 a.u. [31] meaning that Sr will display a surface-active behavior similar to the one observed in molten Al.

The ignition temperatures obtained by Aydin et al. [7] indicate a continuous increase in Mg ignition temperature that plateaus between 2.6 wt% (786 °C) Sr and 4 wt% (798 °C) and then reaches a maximum of 854 °C by adding 6 wt % Sr. In the study presented by Kim et al. [23], the reported ignition temperature for an Mg-2 wt% Sr alloy (0.56 at% Sr) is 632 °C, which coincides with the liquidus point for this composition. A summary of their results is presented in Table 7.1, where we can observe that despite this difference, the ignition temperature difference between pure Mg and the Mg-2Sr alloy is virtually the same (127 °C in average).

Ignition temperature is affected by different factors, such as atmosphere [32], sample size [33, 34] or heating rate [35]. Nevertheless, the discrepancies observed between these two studies were observed in both pure Mg and the Mg-2Sr alloy. In a previous study [16], the authors identified an ignition temperature discrepancy caused using two different heating rates, which affected only Mg-2Ca and Mg-3Ca binary alloys, while pure Mg and a Mg-1Ca alloy seemed unaffected. This was attributed to a microstructural difference observed in the semi-solid state between a high and a low heating rate in the three alloys. A second study [25], demonstrated that the formation of oxidation-resistant molten eutectic pools at the semi-solid stage affected the oxide scale growth at the liquid stage of an Mg-3Ca alloy. When samples were heated using a low heating rate (LHR), these pools were widespread over the surface, covering a large portion of the surface. However, when the sample was heated using a high heating rate (HHR), these pools were not equally spread and resulted in the formation of Ca-rich oxide nodules due to an incomplete melting. The pools formed in the LHR sample are more oxidation resistant than the solid eutectic

microconstituents in the interdendritic region, leading to the formation of a thicker oxide scale and early ignition in the HHR sample.

The heating rate is of importance for the final application of the alloy mainly when it is used in commercial aircraft cabin components. The method developed by the FAA to test alloys suitable for this application involves direct contact between the alloy and a kerosene burner flame. The flame must reach a temperature of 927 ±56 C [36], and the alloy must withstand 2 minutes without burning or losing more than 10% of its original weight at the end of the test. A fast heating rate is expected to be closer to the conditions of ignition in both the FAA test and in a possible post-crash situation.

This paper aims to understand the effectiveness of the Sr in preventing the ignition of four binary Mg-Sr alloys (1-2.5 wt% Sr) under high and low heating rates. An in-depth analysis of one of the alloys is presented to explain the mechanism behind the observed discrepancies.

Table 7.1. Reported ignition temperatures for Mg-Sr binary alloys

Sr amount (wt%)		**0**	**0.3**	**0.57**	**1.02**	**1.5**	**2**	**2.6**	**3.17**	**4.17**	**4.98**	**6.08**
Ignition temperature (°C)	Aydin et al. [7]	640	659	672	748	762	766	786	797	798	825	854
	Kim et al. [23]	504					632					

7.2 Experimental Procedure

Binary Mg-Sr alloys were synthesized using a Norax Induction Furnace (20 kW/5 kHz) at 690 °C, under a protective SF_6/CO_2 protective atmosphere. The materials used were pure Mg supplied by Magnesium Elektron Powders (purity of 99.9 %) and Pure Sr provided by Timinco Metals LTD (purity of 99.5 %). Pure Mg and pure Sr were melted at 690 °C and held at temperature for 15 minutes to allow mixing. The melt was stirred, and the slag was removed prior to casting at 715 °C. The alloys were cast into 6 mm thick plate-samples using an H13 steel permanent-mold

coated with boron nitride. The composition of the obtained plates was determined via Inductively Coupled Plasma – Atomic Emission Spectrometry (ICP-AES) (Table 7.2), performed by the NADCAP certified laboratory Genitest Inc. In this paper, the alloy compositions are given in weight % unless otherwise specified.

Table 7.2. Compositions of Mg-Sr alloys in weight percentage (wt%).

Target compositions	**Elements (wt%)**						
	Sr	**Al**	**Cu**	**Fe**	**Mn**	**Si**	**Mg**
Mg – 1.0 Sr	1.05	0.01	<0.001	0.006	0.02	0.008	Balance
Mg – 1.5 Sr	1.50	0.006	<0.001	0.013	0.01	0.002	
Mg – 2.0 Sr	2.14	0.008	<0.001	0.003	0.004	<0.001	
Mg – 2.5 Sr	2.40	0.007	<0.001	0.032	0.01	<0.001	

Samples of 15 x 15 x 6 mm were machined for ignition tests. The samples were ground down to 800 SiC paper, polished on the wide face down to 0.05 µm colloidal silica. A hole of 1.98 mm (5/64 in.) in diameter was drilled in one of the narrower faces to attach a K-type thermocouple protected with a 316L stainless steel sleeve. The temperature was recorded using a Grant Squirrel data logger (2020 series).

For the full ignition tests, the samples were placed into a Lindberg Blue vertical resistance furnace and heated continuously at two different rates of 25°C/ min (Low Heating Rate – LHR) and 45°C/ min (High Heating Rate – HHR) under a constant flow of extra dry air at a rate of 0.9 L/min. For the interrupted ignition tests, the samples were heated up as in the full ignition tests using both heating rates; however, once the target temperature was reached, the furnace chamber was flushed with Ar reduce the sample temperature. Then, the sample was removed from the

furnace. Samples were microidented using a Vickers tester to localize the same region before and after the interrupted ignition test in the solid and semi-solid states. The temperatures selected to interrupt the test were 560, 620, and 740 °C, as these points represent the solid, semi-solid and liquid states of the alloy during the heating process. For the samples heated using HHR, only the first two interrupted test temperatures could be done because no sample could reach 740 °C without ignition.

The oxidized surfaces were then analyzed thoroughly via Scanning Electron Microscope and Energy Dispersive X-ray Spectroscopy (SEM/EDS). Secondary Electron (SE) and Backscattered Electron (BSE) detectors were used to analyze the microstructural features of the samples at different holding times, using an accelerating voltage of 15 kV for general observation and EDS analysis. Al K-alpha radiation X-Ray Photoelectron Spectroscopy (XPS) was used to analyze the oxide scale formed on selected samples after the interrupted ignition test. A pass energy of 200 eV and a step size of 1 eV were used to determine the chemical composition of the oxide scale (also known as survey spectra), while a high-resolution scanning spectrum was collected using a pass energy of 50 eV and a step size of 0.1 eV to identify the chemical state of an element when required. A 400 μm diameter region was utilized to obtain a compositional depth profile of the surface by gradually removing layers of oxide scale via an Ar ion beam, with a rate of 0.68 nm/second when Ta_2O_5 is etched, which is reference material of the instrument for the removal process. The compounds present on our oxide scales posses a lower hardness compared this reference material, hence the actual etching depth may be higher than the one present in this study and the use of nm to define the etching depth (or oxide scale thickness) should be only viewed as a reference. The Mg KLL region peaks were analyzed for each sample to define the approximate position of the metal/oxide interface during depth profile analysis. The significant chemical shift

observed between metallic and oxide components in this region facilitates their identification even when charging effects are present. This method is illustrated in Fig. 7.6, and it was used for each XPS depth profile presented in this work, indicating the approximate metal/oxide interface using a red dotted line. The data obtained was analyzed using the Advantage -Thermo Fisher Scientific software.

A FIB-SEM Helios Nanolab 660 DualBeam (Focused Ion Beam- Scanning Electron Microscope) was used only to extract the oxide cross-section specimens and thin them down to 100 nm. Then, the samples were observed using a FEI Tecnai G^2 F20 200 kV Cryo-Scanning Transmission Electron Microscope (TEM) equipped with a Scanning Transmission Electron Microscopy (STEM) mode to obtain bright field and High-Angular Annular Dark-Field (HAADF) images. XRD was used to determine the intermetallic compounds in the as-cast alloy samples. The samples were placed inside an X-ray Bruker diffractometer equipped with a Cu Kα radiation source of λ= 1.54060 Å; between 15º and 110º for 2θ.

7.3 Results

7.3.1 Ignition temperature

Four binary compositions, Mg-1.1Sr, Mg-1.5Sr, Mg-2.1Sr, and Mg-2.4 Sr, were used to observe the change in ignition temperature with an increasing amount of Sr when compared to pure Mg. The phase diagram (calculated using the FactSage™-FTlite database) for the Mg-Sr system is shown in Fig. 7.1, along with the melting temperatures of each alloy.

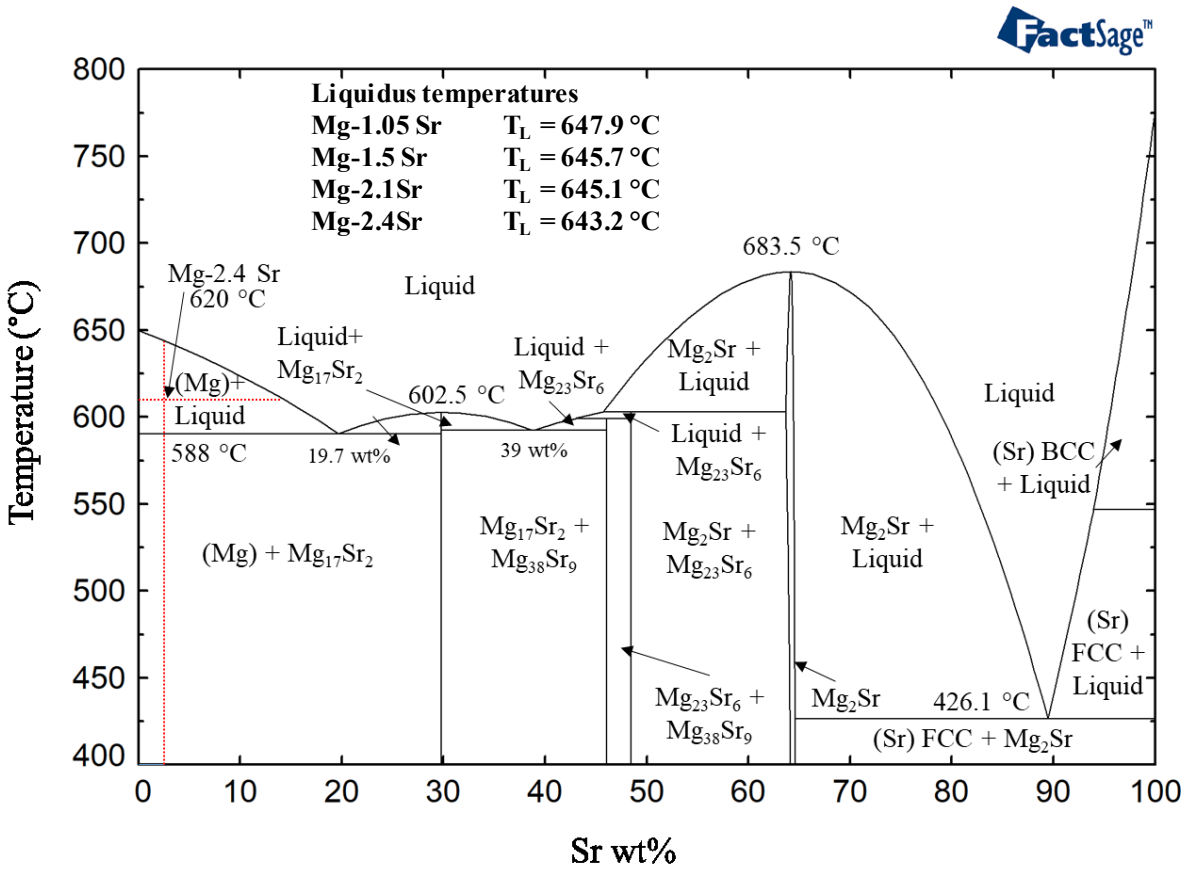

Fig. 7.1. Mg-Sr phase diagram calculated through FactSage™. The liquidus temperatures for the Mg-Sr binary alloys used in this work are indicated on top of the diagram.

The ignition tests results obtained at two heating rates are shown in Fig. 7.2. With a low heating rate (LHR), the ignition temperature increases to 808 ºC with 2.1 Sr. This is higher compared with the previously reported temperature of 766 °C for an Mg-2.0Sr alloy [7]. However, using a high heating rate (HHR), the ignition temperature decreases to 638 °C at 2.4 Sr. The rest of the alloys from 1 to 2.4 wt% Sr show the same trend. The ignition temperature increases with increasing wt% Sr using an LHR; but it drops dramatically when an HHR is used, bringing the ignition temperature close to the melting temperature of each alloy.

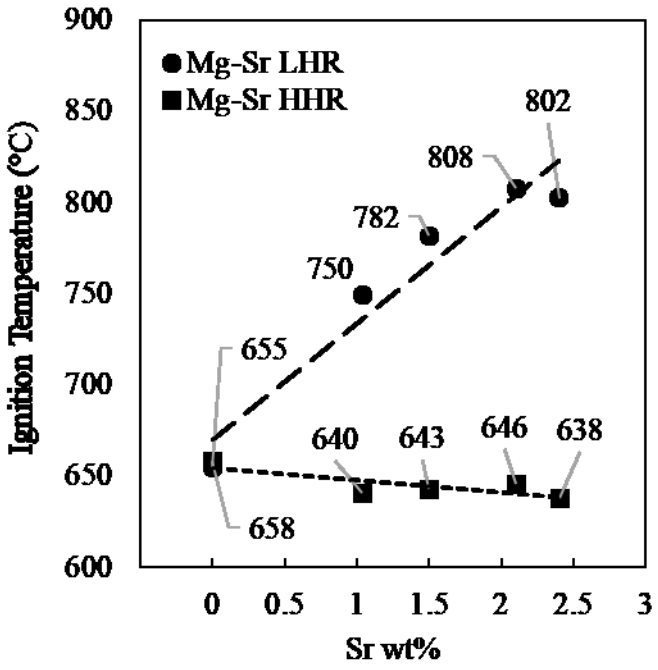

Fig, 7.2. Change in T_i versus Sr wt%. The LHR increases T_i significantly, while the HHR has a less significant effect.

7.3.2 Interrupted Ignition Tests of Mg-2.4Sr: Oxide Scale Evolution

Interrupted ignition tests were carried out on the Mg-2.4 Sr, which demonstrated the most significant difference in ignition temperature between the two heating rates employed and the lowest ignition temperature for the HHR sample. The tests were performed to analyze the microstructural changes in the sample through the heating process, using both heating rates. The curves in Fig. 7.3 represents the temperature inside Mg-2.4 Sr samples heated using both LHR and HHR; the dotted lines indicate the point where the test was stopped.

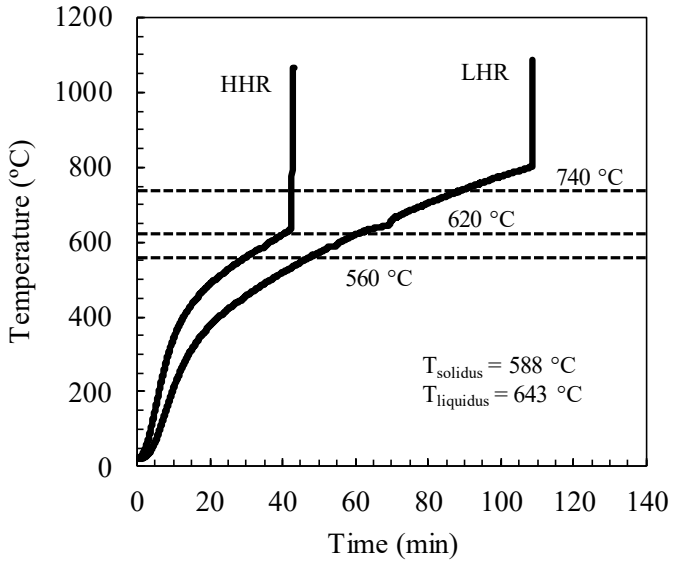

Fig, 7.3. Continuous heating curves for Mg-2.4 Sr alloy at HHR and LHR. The dotted lines show the temperatures were ignition tests were interrupted, which coincides with the solid (560 °C), semi-solid (620 °C) and liquid (700 °C) states.

7.3.2.1 As-Cast alloy

Fig. 7.4a shows the SEM micrographs of the Mg-2.4 Sr alloy, which has a dendritic Mg matrix and an interdendritic intermetallic compound identified as $Mg_{17}Sr_2$ (hP38, $Ni_{17}Th_2$ type) via the XRD spectra shown in Fig. 7.4b.

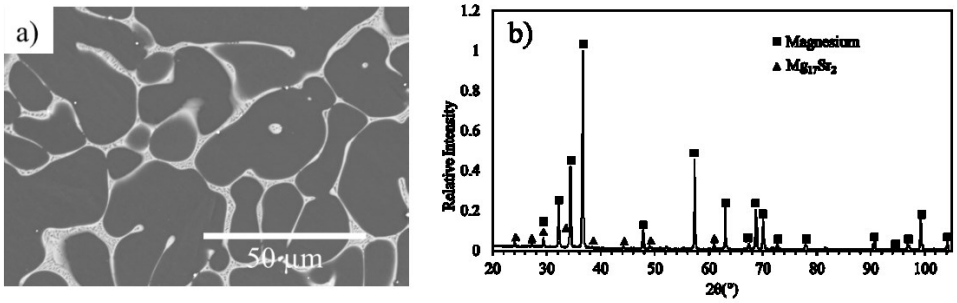

Fig, 7.4. (a) SEM micrograph of as-cast Mg-2.4Sr and (b) XRD spectra for the Mg-2.4 Sr alloy.

EDS indicates that no Sr is retained within the matrix in the as-cast condition (the EDS detector resolution is 0.1wt%), which is expected due to the limited solubility of Sr in Mg even at high temperatures. Sr solubility in Mg reaches a maximum of 0.11 wt% at 585 °C.

The XPS depth profile analysis (Fig. 7.5a), shows that the Sr level is significantly low through the oxide scale in the as-cast state, reaching a maximum of 0.2 at% Sr at the deepest etching level. This is below the bulk composition of 0.68 at% (2.4 wt%). The oxide scale in the cast condition is thin, as the Mg metallic component intensity in the high-resolution Mg KLL region (Fig. 7.5b) gradually increases after just 10 nm etching. According to the binding energy shift in the high resolution scans in Fig. 7.5(c,d), the oxide suffers hydroxylation and carbonation due to the exposure to the atmosphere, resulting in their components shown for Mg2p and O1s. The Mg2p region displays a metallic component at 49.8 eV (FWHM=0.92). The component at 51.0 eV (FWHM=1.8) belongs to MgO, which overlaps right over the $Mg(OH)_2$ component [37, 38]. Finally, a small component belonging to $MgCO_3$ is visible at 52.0 eV (FWHM=1.78). The peak area ratios were compared to the ones deconvoluted in the O1s region to ensure the assigned values have a proper physical meaning. For the O1s region, there are two components visible; the O^{2-} at 531.2 eV (FWHM=1.72), a carbonate component at 533.4 eV (FWHM=1.9 eV) and a high binding energy peak at 533.35 eV (FWHM=1.7), which has been identified in the literature as surface chemisorbed -OH groups [39]. Sr 3d signal was too weak to perform a proper deconvolution, but the peak present at the 30 nm level displayed binding energy of 135.1 eV, suggesting the formation of SrO [40].

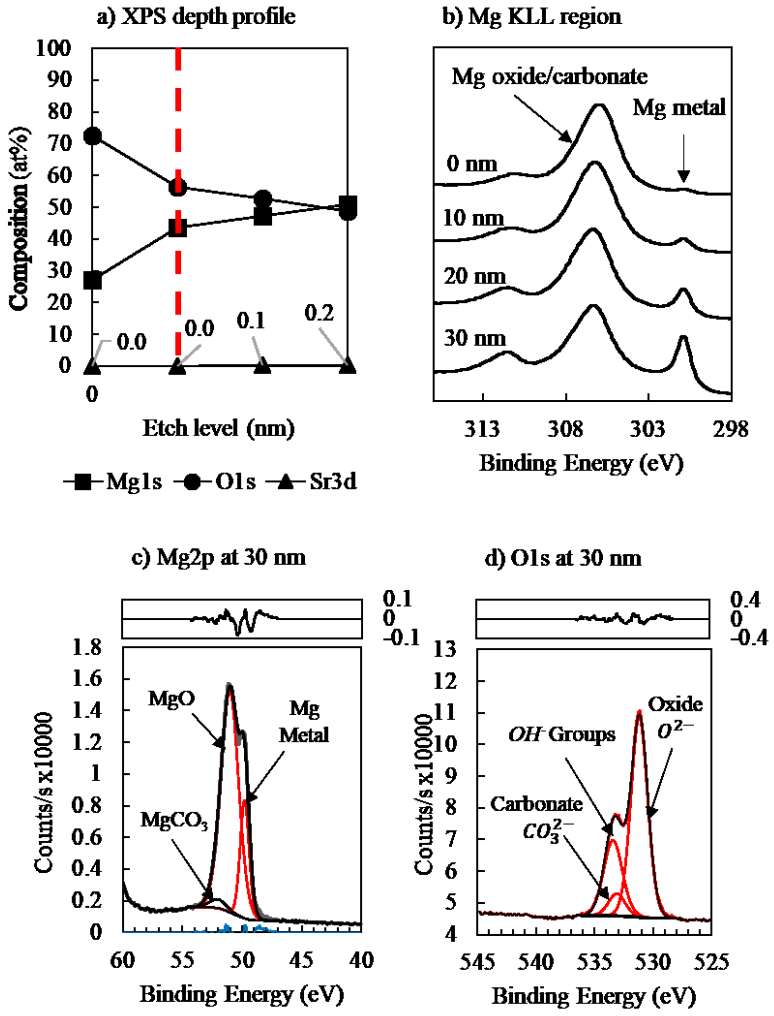

Fig, 7.5. XPS depth profile analysis (a), Mg KLL transitions of Mg-2.4 Sr alloy in the cast condition (b), and the corresponding deconvolution of the level at the deepest level (c,d). The dotted line in (a) shows the depth where the Mg metal peak is first detected in the Mg KLL region spectra.

7.3.2.2 Mg-2.4 Sr after interrupted ignition test at 560 °C

As per Fig. 7.1, the Mg-2.4 Sr alloy is solid at 560 °C, and the LHR and the HHR samples show only a few microstructural changes when heated up to this temperature. The SEM images of the Mg-2.4 Sr alloy before and after the interrupted ignition test are shown in Fig. 7.6, for LHR (a-c) and HHR (d-f). In both samples, the interdendritic region is selectively oxidized. The EDS

line scans of the two samples, presented in Fig. 7.6c and Fig. 7.6f, indicates that the matrix is also oxidized, but the amount of oxygen present in the interdendritic regions is higher. The amount of Sr detected over the Mg matrix using a large analysis area, is consistently 0.8 wt% for the LHR sample and 1.6±0.2 wt% for the HHR sample.

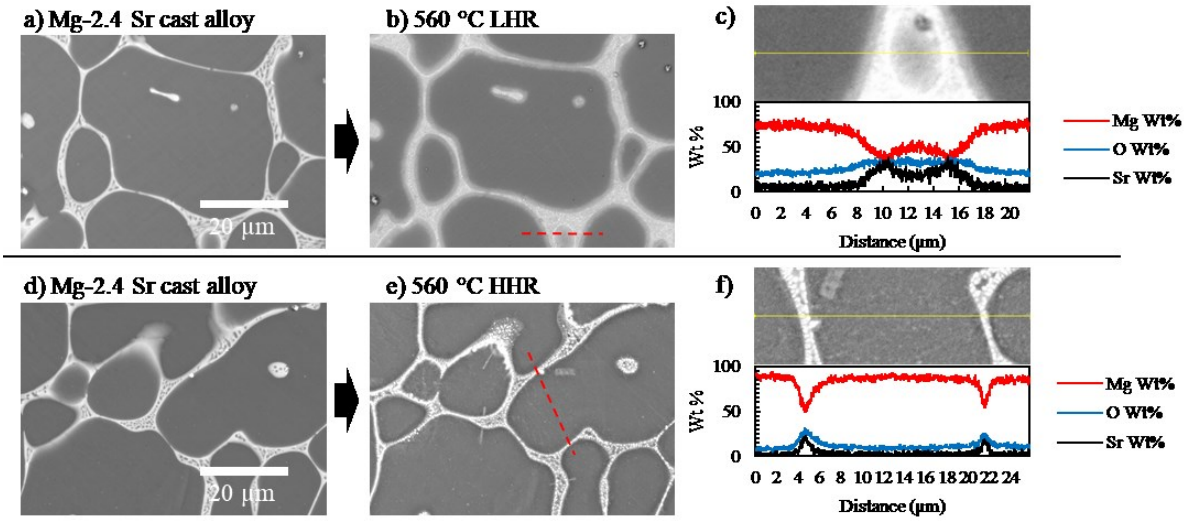

Fig, 7.6. SEM micrographs of selected regions before (a, c) and after (b, d) interrupted ignition tests at 560 °C using both HHR and LHR. The dashed line represents the region analyzed with EDS line scan. (e, f) EDS line scans of the transition between the intermetallic region and the Mg matrix.

The XPS analysis (Fig. 7.7) shows that LHR and HHR samples have similar compositions when a depth profile is performed. Both have a higher amount of Sr at the outermost surface, which declines after the first etching step. In both samples, Mg metallic components are clearly observed at the 500-nm level.

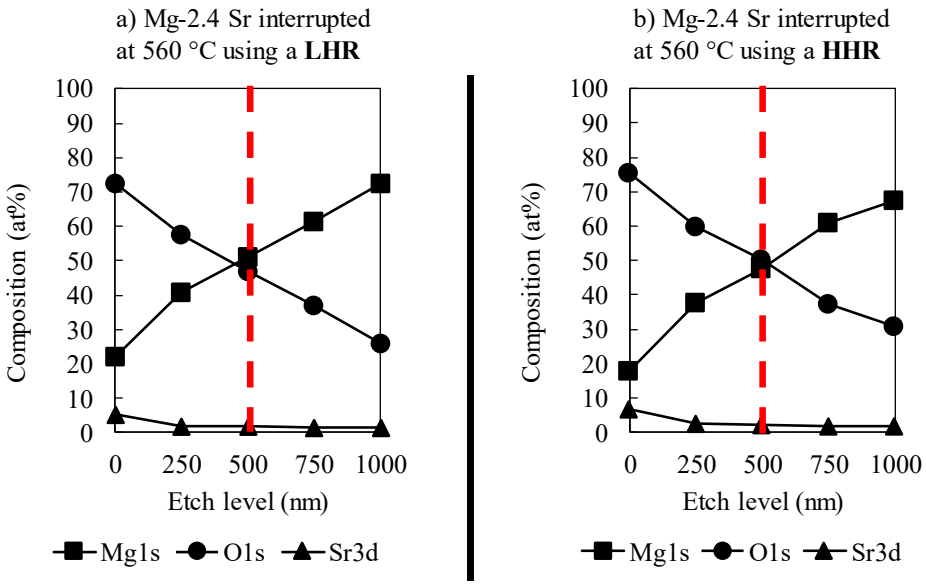

Fig, 7.7. XPS depth profile analysis and Mg KLL transitions of Mg-2.4 Sr alloy after an interrupted test at 560 °C. A higher amount of Sr can be observed on the outermost surface of both samples.

7.3.2.3 Mg-2.4Sr after interrupted ignition test at 620 °C

At 620 °C, ~18% of the alloy reaches the liquid state according to the phase diagram in Fig. 7.1. The SEM images of samples before (Fig. 7.1 a,f) and after the interrupted ignition tests at 620 °C (Fig. 7.1 b,g) and their respective EDS maps reveal significant differences between LHR and HHR samples. The LHR sample (Fig. 7.8 a-e) shows an oxidized region that resembles the as-cast interdendritic region, along with a sizeable Sr-rich phase not associated with oxygen, which is the re-solidified fraction of the alloy that reaches the liquid state. Smaller particles inside the re-solidified Sr-rich phase seem to contain a higher amount of Sr when compared to its surroundings. The HHR sample (Fig. 7.8 f-j) does not show the re-solidified Sr-rich phase observed in the LHR sample. Instead, there are several Sr-rich particles somewhat associated with oxygen. These particles are concentrated in spots rather than extended over the surface. In this sample, the

interdendritic region is heavily oxidized, and it extends towards the matrix with some cracks present (Fig. 7.8g).

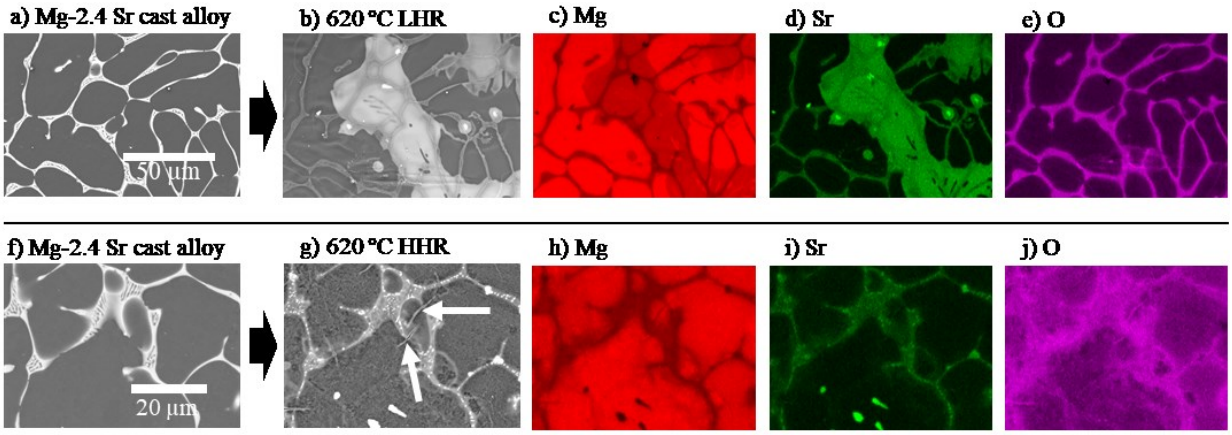

Fig, 7.8. SEM micrographs of selected regions in LHR and HHR Mg 2.4Sr samples before (a, f) and after (b, g) interrupted ignition tests at 620 °C. EDS maps of the Mg-2.4 Sr LHR (c-e) and HHR (h-j) samples are presented. (d) Sr-rich regions can be observed through the surface, which are not strongly associated with oxygen. (d and i) Sr-rich particles are observed.

Oxide cross-sections were extracted from the LHR and HHR samples interrupted at 620 °C using an SEM equipped with a Focused Ion Beam (FIB). The bright-field TEM images obtained are shown in Fig. 7.9. The LHR sample has a re-solidified Sr-rich phase covered by a thin oxide scale. The thickest region of the oxide scale belongs to the position of the original interdendritic region in the cast state and reaches an approximate maximum of 300 nm. Sparsely distributed SrO nodules were present in other interdendritic regions of the LHR sample (as seen in Fig. 7.8d). The HHR sample has a thicker oxide scale close to 700 nm and shows the formation of numerous SrO nodules close to the former interdendritic region, which coincides with the observations made using SEM/EDS.

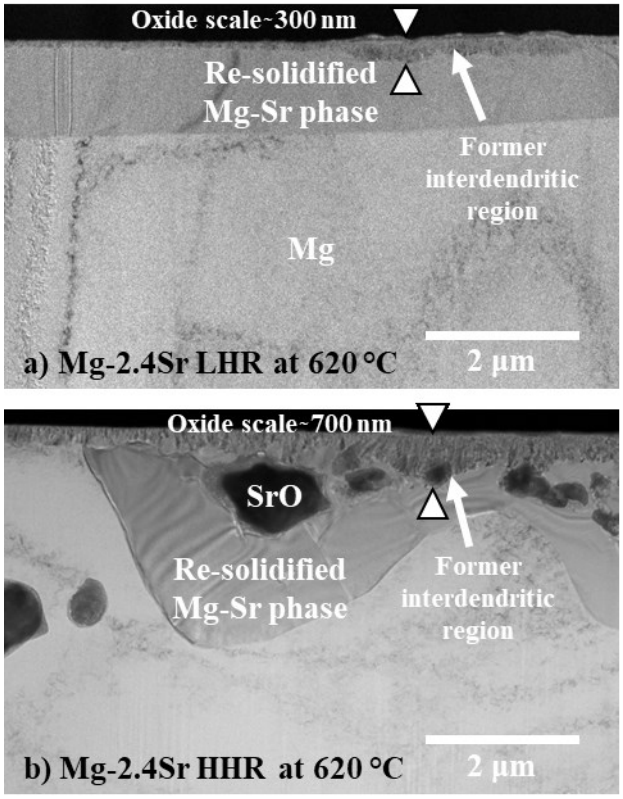

Fig, 7.9. (a) TEM bright-field image of the oxide cross-section extracted through FIB from the Mg-2.4Sr sample interrupted at 620 °C using an (a) LHR and (b) HHR. The thicker oxide regions in both samples correspond to former interdendritic regions; the approximate thickness is indicated.

A High-Angular Annular Dark-Field image (HAADF) of the LHR sample oxide scale is presented in Fig. 7.10. The image belongs to the former interdendritic region indicated in Fig. 7.9a. There is an enrichment of the outermost surface by SrO (A) while the inner oxide is mostly MgO (B) with a small amount of Sr present. Cu signal comes from the sample holder while Ga is a residual from the FIB process used to extract the sample.

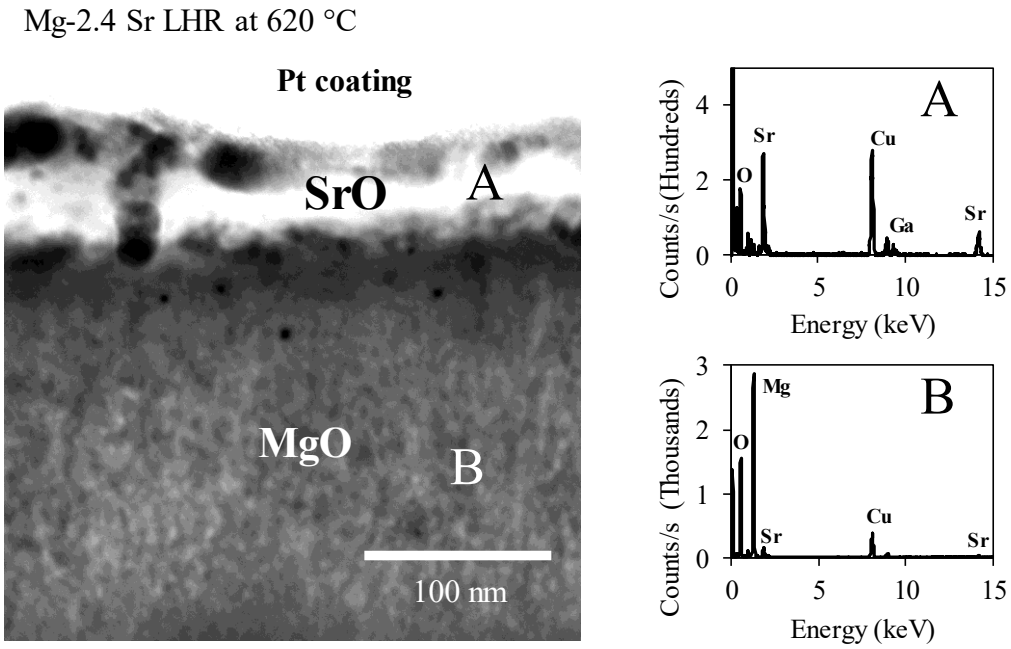

Fig, 7.10. HAADF image of the oxide scale over the $Mg_{17}Sr_2$ intermetallic at the former interdendritic region in the LHR sample interrupted at 620 °C. The outermost surface is covered by SrO (A) while the inner scale is mainly composed by MgO (B) with a small amount of Sr.

The XPS depth profiles of the LHR and HHR samples are shown in Fig. 7.11. It is seen that the thickness of the oxide in the two samples is different; the Mg-metal component in the LHR is visible at 500 nm (which is close to the 300 nm thickness observed in Fig. 7.10a). From this point, the amount of Sr tends to increase towards inner levels of the oxide scale. In the HHR sample, the Mg-metal component is visible at 750 nm, confirming the oxide scale larger overall thickness in the HHR sample.

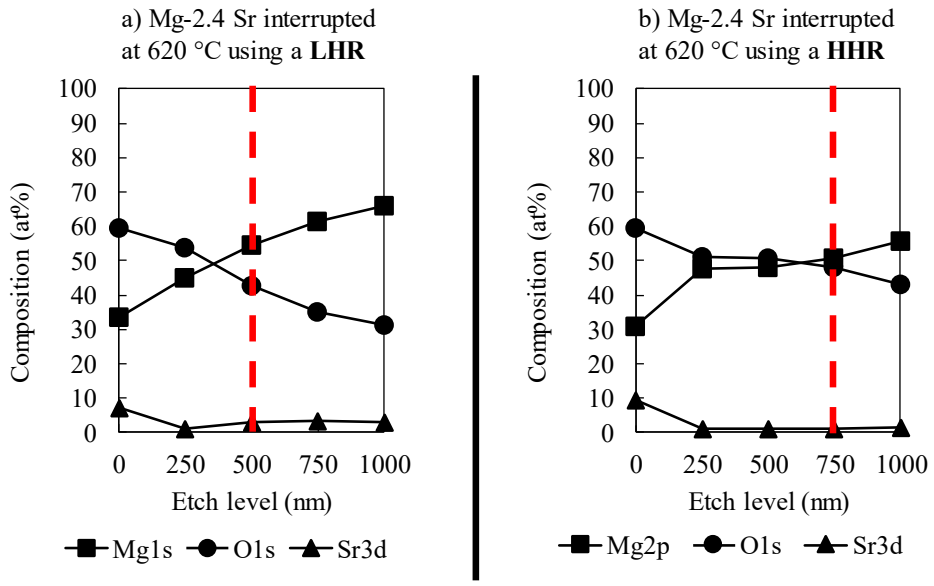

Fig, 7.11. XPS depth profiles after an interrupted test at 620 °C using (a) an LHR and (b) an HHR. Sr is enriched in the outermost surface and decreases towards the metal/oxide interface, which is shown with dotted lines.

7.3.2.4 Mg-2.4Sr after interrupted ignition test at 740° C

Fig. 7.2 indicates that, at 740 °C, the HHR sample ignited at 638 °C, hence, making it impossible to analyze it at this point. When the LHR sample reaches 740 °C, it is fully molten as seen in Fig. 7.1 phase diagram. Fig. 7.13a shows the SEM image of the top surface of the re-solidified LHR sample. The cross-section of this sample (Fig. 7.13b) shows a re-solidified network of $Mg_{17}Sr_2$ through the sample. Fig.7.13c shows the EDS mapping of the top surface of the re-solidified sample. The re-solidified Sr-rich phase observed in the semi-solid state is present at the liquid state as well, which is not strongly associated with oxygen on the surface. Sr appears to be concentrated through the oxide scale formed at early stages.

An XPS depth profile (Fig. 7.14) was performed up to a 2000 nm level; the Mg metallic component can be observed at 1000 nm, which is the double of the 500 nm oxide observed at 620

°C in the LHR sample. The oxide scale is composed mainly by Mg, with only a small amount of Sr in it.

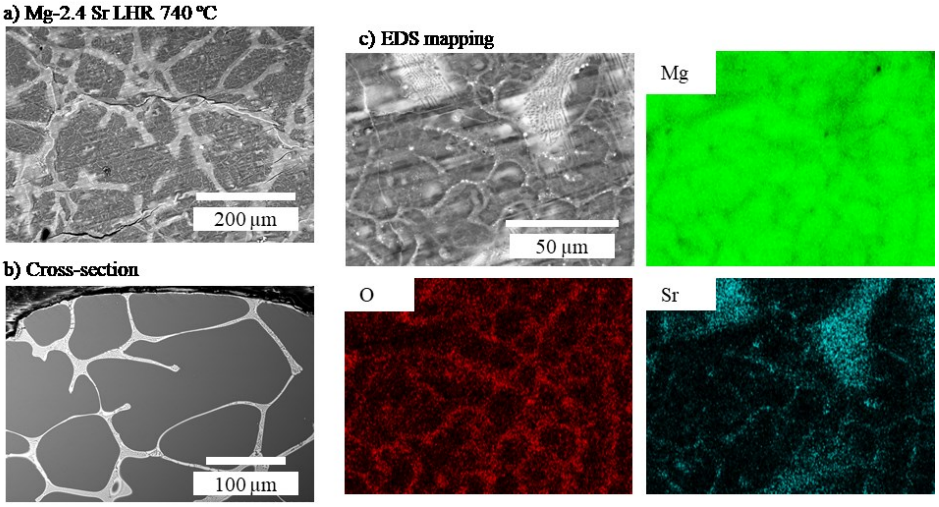

Fig, 7.12. SEM-BSE images of (a) the oxidized surface in the Mg-2.4Sr sample after interrupted ignition test at 740 ºC and (b) a cross-section of the same sample. (c) EDS maps of LHR Mg-2.4 Sr and interrupted at 740 °C. Sr-rich regions can be observed through the surface, which are *not strongly associated with oxygen.*

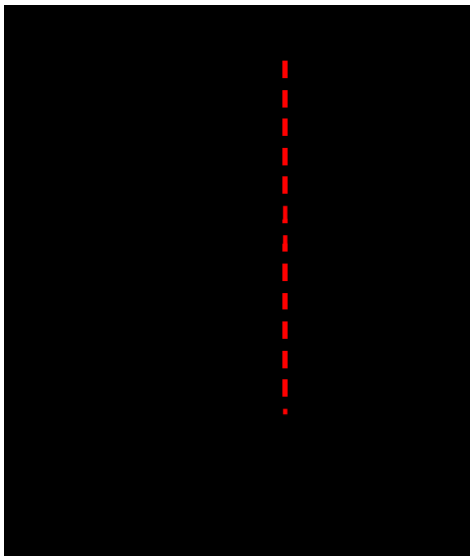

Fig, 7.13. XPS depth profile analysis (a) and Sr3d high-resolution scan (b) of Mg-2.4 Sr alloy after an interrupted test at 740 °C using an LHR. The oxide scale is composed mainly by MgO.

7.4 Discussion

The observations via SEM and XPS on the oxide scale evolution are summarized in Table 7.3.

Table 7.3. Summary of the results obtained through the interrupted ignition tests.

T (°C)/state	**Samples**	**Surface characteristics**	**Oxide scale characteristics**
Room T/solid	As-cast	Eutectic $Mg_{17}Sr_2$	MgO (with some hydroxylation/carbonation)
560 °C/solid	LHR	Oxidized interdendritic regions. Lateral oxide growth.	500 nm oxide scale with a high amount of Sr at the outermost surface
	HHR		
620 °C/ re-solidified semi-solid	LHR	Re-solidified $Mg_{17}Sr_2$ not associated with O. SrO particles engulfed in re-solidified $Mg_{17}Sr_2$ and SrO oxide nodules	500 nm oxide scale SrO enriched at the outermost region.
	HHR	Oxidized $Mg_{17}Sr_2$. Extensive interdendritic oxidation with lateral growth and presence of SrO nodules.	750 nm oxide scale. Slightly higher Sr content at the outermost surface when compared to LHR sample.
740 °C/ re-solidified liquid	LHR	Re-solidified $Mg_{17}Sr_2$ phase on the surface. No Sr-rich nodules.	1000 nm oxide scale. Mainly MgO, no SrO enrichment at the outermost surface
	HHR	Above the ignition temperature	

The solid-state (560 °C) oxidation behavior of both samples at this stage displays close similarities; 500-nm thickness oxide scale, selectively oxidized intermetallic compounds and high Sr content at the outermost surface. This increase of Sr at the outermost surface is caused by the lower oxygen affinity of Sr at this temperature when compared to Mg. During high-temperature oxidation in the solid-state, Sr will oxidize mostly from the interdendritic regions, and further growth will be controlled by (i) the lateral growth of this oxide and (ii) the diffusion of Sr though

the MgO formed at the matrix. This will drive Sr towards regions with a higher oxygen activity within the oxide scale (gas/oxide interface), while Mg will oxidize at regions with a lower oxygen activity (metal/oxide interface). One difference observed between heating rates at this stage is the amount of Sr over the matrix. Sr wt% in the HHR is double when compared to the LHR sample. This suggests a higher degree of lateral oxidation coming from the interdendritic region in the HHR sample.

During the semi-solid state (620 °C), the oxidation in the HHR sample seems to proceed mostly from the interdendritic regions and towards the matrix through lateral growth. This generates increasing stresses since *the lateral growth strain rate is proportional to the thickening rate of the oxide* [41]. This explains the cracks observed in 7.8g. Also, numerous SrO nodules are formed through the scale, creating vulnerable regions in the oxide scale. Once the liquid state is reached, the sample ignites due to the lack of a protective oxide through most of the sample surface. The LHR sample, on the other hand, allows the formation of Sr-rich pools which in turn results in the formation of a regular SrO scale at the gas/oxide interface, hindering oxidation through this stage and once the liquid state is reached. At the liquid stage (740 °C), SrO might be reduced by Mg as further oxidation proceeds, decreasing its overall content in the oxide scale.

Through the presented results, it is evident that the formation of a rich layer of SrO itself is not the only critical factor for the development of a protective scale. Although the formation of a compact oxide MgO/SrO scale at the gas/oxide interface would prove to be protective thanks to its Effective Pilling Bedworth Ratio (EPBR) higher than 1, there are some other factors to consider. Profuse oxidation and increase of internal stresses in the oxide scale over the interdendritic regions result in the early ignition of the HHR sample. The Sr surface enrichment in the liquid fraction of the LHR semi-solid state, improves the distribution of Sr through the surface, allowing the

formation of a more protective oxide scale than the one developed due to lateral growth in the solid-state. The protection offered by Sr against ignition is hindered by its close oxygen affinity to Mg at high temperatures and is dependent on its surface activity in the liquid state.

7.5 Conclusions

The ignition resistance of a series of Mg-Sr alloys (Mg-1.1Sr, Mg-1.5Sr, Mg-2.14Sr, and Mg-2.4Sr) was tested using two different heating rates. The results indicate that the use of a high heating rate (HHR) would cause the Mg-Sr alloys to ignite prematurely, close to their liquidus temperature. On the other hand, the use of a low heating rate (LHR) rate increases the ignition temperature of pure Mg significantly by adding as low as 1 wt% Sr. Interrupted ignition tests at the solid, semi-solid and liquid stages during continuous heating resulted in the following:

1. During the solid-state, the oxidation behavior of both samples is similar. Both samples show enrichment of Sr at the gas/oxide interface.
2. During the semi-solid state, the samples heated using an LHR display the formation of molten Sr-rich pools, allowing an even distribution of SrO.
3. The HHR samples do not develop Sr-rich pools due to the short time elapsed, resulting in more substantial oxide stress due to lateral growth and the formation of numerous SrO nodules.
4. At the liquid stage, the HHR sample ignites. The LHR withstands the temperature increase thanks to the continuous SrO scale formed at early stages due to the formation of Sr-rich pools.
5. The Sr content is rather low through the interrupted tests, even at the liquid stage, meaning that the protection mechanism is hindered by the low oxygen affinity of Sr when compared to Mg.

7.6 Acknowledgements

This project was conducted under the financial support of the Natural Sciences and Engineering Research Council of Canada (NSERC) Discovery Grant. The authors thanks Pierre Vermette from McGill University for his assistance in alloy making and casting. Luis Angel Villegas-Armenta gratefully acknowledges the financial support of CONACYT of Mexico for the scholarship 410607 and McGill Engineering Doctoral Award (MEDA).

7.7 References for Chapter 7

[1] T.-S. Shih, J.-H. Wang, and K.-Z. Chong, "Combustion of magnesium alloys in air," Mater. Chem. Phys., vol. 85, no. 2, pp. 302-309, 2004.

[2] S. K. Kim, J.-K. Lee, Y.-O. Yoon, and H.-H. Jo, "Development of AZ31 Mg alloy wrought process route without protective gas," J. Mater. Process. Technol., vol. 187, pp. 757-760, 2007.

[3] N. R. Kumar, J. Blandin, M. Suery, and E. Grosjean, "Effect of alloying elements on the ignition resistance of magnesium alloys," Scr. Mater., vol. 49, no. 3, pp. 225-230, 2003.

[4] B.-H. Choi, B.-S. You, W.-W. Park, Y.-B. Huang, and I.-M. Park, "Effect of Ca addition on the oxidation resistance of AZ91 magnesium alloys at elevated temperatures," Met. Mater. Int., journal article vol. 9, no. 4, pp. 395-398, 2003.

[5] B. S. You, W. W. Park, and I. S. Chung, "The effect of calcium additions on the oxidation behavior in magnesium alloys," Scr. Mater., vol. 42, pp. 1089–1094, 2000.

[6] L. Jin-Kyu, "Effect of CaO composition on oxidation and burning behaviors of AM50 Mg alloy," Trans. Nonferrous Met. Soc. China, vol. 21, pp. 23-27, 2011.

[7] D. S. Aydin, Z. Bayindir, and M. O. Pekguleryuz, "The effect of strontium (Sr) on the ignition temperature of magnesium (Mg): a look at the pre-ignition stage of Mg–6 wt% Sr," J. Mater. Sci., vol. 48, no. 23, pp. 8117-8132, 2013.

[8] F. Jianfeng, C. Zhiyuan, Y. Weidong, F. Shuang, and X. Bingshe, "Effect of yttrium, calcium and zirconium on ignition-proof principle and mechanical properties of magnesium alloys," J. Rare Earths, vol. 30, no. 1, 2012.

[9] J.-K. Lee, H.-H. Jo, and S. K. Kim, "Effet of CaO addition on ignition behavior in molten AZ31 and AZ91D magnesium alloys," Rare Met., vol. 25, no. Special Issue, pp. 155-159, 2006.

[10] C. Liu, S. Lu, Y. Fu, and H. Zhang, "Flammability and the oxidation kinetics of the magnesium alloys AZ31, WE43, and ZE10," Corros. Sci., vol. 100, no. 177–185, 2015.

[11] A. Prasad, Z. Shi, and A. Atrens, "Flammability of Mg–X Binary Alloys," Adv. Eng. Mater., vol. 14, no. 9, pp. 772-784, 2012.

[12] D. S. Aydin, Z. Bayindir, M. Hoseini, and M. O. Pekguleryuz, "The high temperature oxidation and ignition behavior of Mg–Nd alloys part I: The oxidation of dilute alloys," J. Alloys Compd., vol. 569, no. 35–44, 2013.

[13] D. S. Aydin, Z. Bayindir, and M. O. Pekguleryuz, "High Temperature Oxidation Behavior of Hypoeutectic Mg–Sr Binary Alloys: The Role of the Two-Phase Microstructure and the Surface Activity of Sr," Adv. Eng. Mater., vol. 17, no. 5, pp. 697-708, 2015.

[14] D. S. Aydin, Z. Bayindir, and M. O. Pekguleryuz, "The high temperature oxidation behavior of Mg–Nd alloys. Part II: The effect of the two-phase microstructure on the on-set of oxidation and on oxide morphology," J. Alloys Compd., vol. 584, no. 558–565, 2014.

[15] D. B. Lee, "High temperature oxidation of AZ31 + 0.3 wt.%Ca and AZ31 + 0.3 wt.%CaO magnesium alloys," Corros. Sci., vol. 70, no. 243–251, 2013.

[16] L. A. Villegas-Armenta, R. A. L. Drew, and M. O. Pekguleryuz, "The Ignition Behavior of Mg-Ca binary alloys; The Role of Heating Rate," 2019.

[17] S.-Y. Chang, M. Matsushita, H. Tezuka, and A. Kamio, "Ignition prevention of magnesium by simultaneous addition of calcium and zirconium," Int. J. Cast Met. Res., vol. 10, no. 6, pp. 345-351, 1998.

[18] M. Liu, D. S. Shih, C. Parish, and A. Atrens, "The ignition temperature of Mg alloys WE43, AZ31 and AZ91," Corros. Sci., vol. 54, no. 139–142, 2012.

[19] J.-s. Rao, H.-j. Li, and H.-s. Xue, "Ignition-proof mechanism of ZM5 magnesium alloy added with rare earth," J. Cent. South Univ. Technol., vol. 17, no. 1, pp. 28-33, 2010.

[20] P. L.-m. Wu Yu-juan, Zhao Su, Li De-jiang, Huang Fei, Ding Wen-jiang, "Ignition-Proof Properties of a High-Strength Mg-Gd-Ag-Zr Alloy," J. Shanghai Jiaotong Univ., vol. 17, no. 643-647, 2012.

[21] A. Prasad, Z. Shi, and A. Atrens, "Influence of Al and Y on the ignition and flammability of Mg alloys," Corros. Sci., vol. 55, pp. 153-163, 2012.

[22] P.-y. Lin, H. Zhou, W. Li, W.-p. Li, N. Sun, and R. Yang, "Interactive effect of cerium and aluminum on the ignition point and the oxidation resistance of magnesium alloy," Corros. Sci., vol. 50, no. 9, pp. 2669-2675, 2008.

[23] Y. M. Kim, C. D. Yim, H. S. Kim, and B. S. You, "Key factor influencing the ignition resistance of magnesium alloys at elevated temperatures," Scr. Mater., vol. 65, no. 11, pp. 958-961, 2011.

[24] J. F. Fan, G. C. Yang, Y. H. Zhou, Y. H. Wei, and B. S. Xu, "Selective Oxidation and the Third-Element Effect on the Oxidation of Mg-Y Alloys at High Temperatures," Metall. Mater. Trans. A, vol. 40A, pp. 2184-2189, 2009.

[25] L. A. Villegas-Armenta, R. A. L. Drew, and M. O. Pekguleryuz, "X-Ray Photo-Electron Spectroscopy and Electron Microscopy Study of Oxide-Scale Evolution on Ignition Resistant Mg-3Ca Alloy at Low and High Heating Rates," 2019.

[26] D. S. Aydin, "High Temperature Oxidation and Ignition Behaviour of Magnesium Alloys Containing Strontium (Sr) and Neodymium (Nd)," ed. Montreal, Canada, 2014.

[27] O. Ozdemir, J. E. Gruzlesky, and R. A. L. Drew, "Effect of Low-Levels of Strontium on the Oxidation Behavior of Selected Molten Aluminum-Magnesium Alloys," Oxid. Met., vol. 72, pp. 241–257, 2009.

[28] K. Dennis, "Effects of Magnesium, Silicon, and Strontium on the Oxidation of Molten Aluminum," McGill University Libraries, 1999.

[29] M. O. Pekgueleryuez and M. M. Avedesian, Magnesium alloying - some metallurgical aspects. DGM Informationsges. Verl, Oberursel (Germany); Deutsche Gesellschaft fuer Materialkunde e.V., Oberursel (Germany), 1992, pp. Medium: X; Size: pp. 213-220.

[30] P. Politzer, R. G. Parr, and D. R. Murphy, "Approximate determination of Wigner-Seitz radii from free-atom wave functions," Phys. Rev. B, vol. 31, no. 10, p. 6809, 1985.

[31] P.-G. Reinhard and E. Suraud, Introduction to cluster dynamics. John Wiley & Sons, 2008.

[32] W. M. Fassell, L. B. Gulbransen, J. R. Lewis, and J. H. Hamilton, "Ignition temperatures of magnesium and magnesium alloys," J. Met., vol. 3, no. 7, pp. 522-528, 1951.

[33] P. Boris, "A Study of the Famability of Magnesium," Federal Aviation Agency, Washington, D.C.1964, Available: http://www.dtic.mil/dtic/tr/fulltext/u2/644408.pdf.

[34] Y. Chunmiao, H. Dezheng, L. Changc, and L. Gang, "Ignition behavior of magnesium powder layers on a plate heated at constant temperature," J. Hazard. Mater., vol. 246-247, no. 283-290, 2013.

[35] C. Liu, S. Lu, Y. Fu, and H. Zhang, "Flammability and the oxidation kinetics of the magnesium alloys AZ31, WE43, and ZE10," Corr. Sci., vol. 100, pp. 177-185, 2015.

[36] T. R. Marker, "DOT/FAA/TC-13/52 - Development of a Laboratory-Scale Flammability Test for Magnesium Alloys Used in Aircraft Seat Construction," Federal Aviation Administration, New Jersey2014.

[37] M. Santamaria, F. Di Quarto, S. Zanna, and P. Marcus, "Initial surface film on magnesium metal: a characterization by X-ray photoelectron spectroscopy (XPS) and photocurrent spectroscopy (PCS)," Electrochim. Acta, vol. 53, no. 3, pp. 1314-1324, 2007.

[38] V. Fournier, P. Marcus, and I. Olefjord, "Oxidation of magnesium," Surf. Interface Anal., vol. 34, no. 1, pp. 494-497, 2002.

[39] S. Ardizzone, C. Bianchi, M. Fadoni, and B. Vercelli, "Magnesium salts and oxide: an XPS overview," Appl. Surf. Sci., vol. 119, no. 3-4, pp. 253-259, 1997.

[40] H. V. Doveren and J. A. T. Verhoeven, "XPS spectra of Ca, Sr, Ba and their oxides," J. Electron. Spectrosc. Relat. Phenom., vol. 21, no. 3, pp. 265-273, 1980.

[41] D. R. Clarke, "The lateral growth strain accompanying the formation of a thermally grown oxide," Acta Mater., vol. 51, no. 5, pp. 1393-1407, 2003.

Chapter 8 - General Discussion

The initial analysis in this thesis consisted in the ignition testing of a ternary Mg-2.5Sr-1.0Ca alloy, which showed an ignition temperature improvement (747 °C) when compared to pure Mg (634 °C) or commercial alloys such as AZ91 (580 °C) [1]. This was attributed to the formation of a protective CaO/SrO scale with an Effective Pilling Bedworth Ratio (EPBR) greater than 1, due to the difference in molar volume between the alloy itself and the oxide formed on its surface. With this, it was defined that both SrO and CaO had the potential to form protective oxide scales under this principle. However, most of the contribution in the solid state came from the formation of CaO, while SrO was formed virtually only at the liquid state. In either way, the lower content of MgO on the surface would allow the formation of a protective barrier which increases igntion temperature.

However, when this ternary alloy was compared to its binary counterparts reported in the literature, it was observed that the simultaneous addition of Ca and Sr resulted in an apparently detrimental result. The ignition temperature of a Mg-2.0 wt% Sr binary alloy was reported to reach 766 °C [2]. The simultaneous use of Sr and Ca would not cause a synergistic effect increasing the ignition temperature of Mg.

Hence, binary Mg-Ca (1.1, 1.7, and 3 wt% Ca) and Mg-Sr (1.05, 1.5, 2.1, 2.4 wt%) alloys were cast to analyze the underlying mechanisms that might cause this discrepancy. *The use of two heating rates, a High Heating Rate (HHR) of 45 °C/min and a Low Heating Rate of 25 °C/min (LHR) in the binary alloys, not only revealed one of the reasons for the different ignition temperatures found in the literature, but also unveiled some mechanisms not previously reported in Mg-Sr and Mg-Ca binary systems, revealing interesting differences between them*. These differences are summarized as follows:

Ignition temperature: The difference observed between using an LHR and an HHR rate was only evident when larger amounts of Ca (2 wt% and 3 wt% Ca) were used, while at 1 wt% Ca the difference was not clearly discernible. On the other hand, the Mg-Sr alloys demonstrated a dramatic change in ignition temperature, where the use of an HHR resulted in ignition at the melting temperature at any Sr wt%. This explained the difference against the values found in the literature, as the Mg-2.5Sr-1.0Ca alloy was tested using an HHR, but the causes for this phenomenon in the Mg-Sr and Mg-Ca systems were still unclear. It is important to remember that these discrepancies were not observed in pure Mg, but only in the Mg-Ca and Mg-Sr alloys. This pointed out the importance of microstructural evolution in the ignition outcome, especially in multi-phase systems.

Table 8.1. Summary of the average ignition temperatures obtained for the Mg-Ca and Mg-Sr binary alloys. Units are in degrees Celsius.

Mg-Ca alloys	**LHR**	**HHR**	**Mg-Sr alloys**	**LHR**	**HHR**
Pure Mg	655	658	**Pure Mg**	655	658
Mg-1.1Ca	753	775	**Mg-1.0Sr**	750	640
Mg-1.7Ca	841	752	**Mg-1.5Sr**	782	643
-	-	-	**Mg-2.1Sr**	808	646
Mg-3.0Ca	861	787	**Mg-2.4Sr**	802	638

Surface microstructure evolution: In both Mg-Ca and Mg-Sr alloys, the presence of molten eutectic pools defined the effectiveness of the alloying elements in increasing the igntion temperature of Mg. In the Mg-Ca alloys, the presence of oxidation-resistant pools (using an LHR) allowed the formation of a thin and compact CaO scale through the alloy surface. Otherwise, the use of an HHR would result in the profuse oxidation of the solid intermetallics causing the

formation of CaO nodules and early oxide breakdown. Here, there is little competition between MgO and CaO formation, as the latter has a significantly higher oxygen affinity, overpowering MgO formation. The cause for the early igntion using an HHR is related mainly to the profuse oxidation of Ca and oxide failure which exposes molten Mg to the atmosphere, rather than the lack of CaO formation. Compared to Mg-Sr alloys, the early ignition is related to a substantially different mechanism. The presence of Sr-rich molten pools allowed the formation of a continuous SrO oxide scale evenly distributed over these pools. Using an HHR results in the oxidation of SrO mostly from the solid interdendritic regions, resulting in oxide nodules and an oxide scale that grows laterally with higher internal stresses. Once the liquid state is reached under these conditions, the poor SrO coverage of the surface results in early ignition.

In summary, the semi-solid state played an important role in the ignition temperature due to the formation of molten pools for both binary alloys. This is contrary to the previous belief that the formation of eutectic pools is imperatively a cause for Mg evaporation and early ignition [3].

Oxide growth: XPS depth profiles were performed in the Mg-3Ca and Mg-2.4Sr alloys to track the oxide growth at each stage of the ignition test. In general terms, the Mg-3Ca alloy developed Ca-enrichment at the metal/oxide interface during the solid and semi-solid stages. Diffusion of Ca ions is slower than Mg ions through the initial MgO scale, but due to the higher oxygen affinity of Ca, CaO would tend to be formed at the metal/oxide interface (low oxygen partial pressure) reducing MgO. Sr, on the other hand, has an even lower diffusion rate in MgO compared to Ca ions, as diffusion of ionic species is inversely proportional to their ionic radius [4]. At low temperatures, Sr oxygen affinity is lower than that of Mg, hence driving the formation of SrO towards the gas/oxide interface, where more oxygen is available. For this reason, Sr tends to enrich the outermost surface of the alloy, but the inner layers are still composed mostly by MgO.

At the liquid stage, however, Ca oxidizes profusely in the Mg-3Ca when an HHR is used, causing breakage of the oxide scale despite its protective nature. The LHR sample develops a thin and protective oxide scale, thanks to the formation of widespread oxidation-resistant eutectic molten pools. In the liquid Mg-2.4Sr alloy, the amount of Sr in the oxide scale is very low, even at the outermost surface, but once again, the use of an LHR results in the formation of a thin oxide scale with a small amount of SrO at the outermost surface, resulting in a higher ignition temperature.

When we compare this to the Mg-2.5Sr-1Ca alloy, we can observe that in this alloy, the Sr and Ca contents are significantly high through the oxide scale during the liquid stage and at the onset of ignition. Despite the protective nature of a compact oxide scale with an EPBR higher than 1, the formation of thick oxide scales and oxide nodules results in early ignition, as observed in the two binary alloys. Hence, the combined use of Ca and Sr seemed to affect the effectiveness of Sr increasing the ignition temperature due to the vigorous oxidation of this element at the liquid stage, compared to the binary Mg-2.4Sr alloy heated with an LHR. This demonstrated that there are other mechanisms besides the EPBR that are critical for the formation of a protective oxide scale, which will be explained in the next section.

It is evident that there are significant differences between Mg-Sr and Mg-Ca systems; Ca has a higher oxygen affinity which allows a readily oxide formation that offers some degree of protection regardless of the heating rate used, thanks to its EPBR greater than 1 when alloyed with Mg. Sr, despite being able to form a compact oxide scale under the same principle, has a lower oxygen affinity (compared to Mg) that impedes the formation of a protective scale solely relying on this mechanism. It depends almost entirely on the formation of liquid pools to develop a

continuous SrO scale, which would explain the importance of Sr surface-segregation previously discussed in our group.

In summary, observing the comparison between Mg-Sr, Mg-Ca and the Mg-Sr-Ca alloys, it is possible to state that the main factor improving Mg ignition temperature resides in the use of high oxygen affinity elements, followed by their capacity to develop an oxide with an EPBR higher than 1. The use of surface-active elements will be an asset if the selected element complies with these two characteristics. Localized vigorous oxidation of second phases would result in early ignition despite the protective nature of the oxides formed over the alloy. Hence, the matrix solubility, early liquid formation, and second phase distribution greatly affect the ignition temperature of Mg alloys. The third element seemed to not display an effect in the Mg-Sr-Ca system as SrO and MgO oxygen affinities lie very close. This hindered the capability of Sr to provide a proper protection as Mg and Ca higher oxygen affinities were dominant in the oxidation process, despite the surface-active behavior of Sr. The use of an element with an intermediate oxygen affinity between Mg and Ca, or, with an oxygen affinity higher than Ca would be an option to apply this effect in the Mg-Ca system. This could allow the formation of a barrier at the metal/oxide interface that allows the most oxygen reactive element to form a protective barrier using lower quantities in the alloy making.

References for Chapter 8

[1] N. V. R. Kumar, J. J. Blandin, M. Suéry, and E. Grosjean, "Effect of alloying elements on the ignition resistance of magnesium alloys," Scr. Mater., vol. 49, no. 3, pp. 225-230, 2003.

[2] D. S. Aydin, Z. Bayindir, and M. O. Pekguleryuz, "The effect of strontium (Sr) on the ignition temperature of magnesium (Mg): a look at the pre-ignition stage of Mg–6 wt% Sr," J. Mater. Sci., vol. 48, no. 23, pp. 8117-8132, 2013.

[3] Q. Tan, A. Atrens, N. Mo, and M.-X. Zhang, "Oxidation of magnesium alloys at elevated temperatures in air: A review," Corros. Sci., vol. 112, pp. 734-759, 2016.

[4] J. A. Van Orman and K. L. Crispin, "Diffusion in Oxides," Rev. Mineral. Geochem., vol. 72, no. 1, pp. 757-825, 2010.

Chapter 9 - General Conclusions and Future Work

9.1 General Conclusions

In this thesis work, the feasibility of developing Mg-Sr-Ca ignition resistant alloys was evaluated, along with the effect of heating rate on the ignition temperature of Mg-Ca and Mg-Sr binary alloys. For these three subjects, the following general conclusions were drawn:

9.1.1 The Mg-2.5Sr-1.0Ca Alloy

The simultaneous use of Ca (1.0 wt%) and Sr (2.5 wt%) results in an ignition temperature of 747 °C, which is an improvement of ~100 °C when compared to pure Mg (658 °C). However, this improvement is less when compared to the ignition temperature of 775 °C of the Mg-1.1Ca binary alloy, obtained under the same conditions. Hence, the addition of Sr does not show a synergistic effect when used simultaneously with Ca. The following highlights can be drawn from the mechanism behind this result.

1. The protective behavior of elements with a Pilling-Bedworth Ratio (PBR) lower than 1 can be explained due to the difference that exists between the molar volume of the pure elements and the molar volume of the alloy (substrate) in which these elements are employed. The calculation of an Effective Pilling-Bedworth Ratio (EPBR) demonstrates that considering the molar volume of CaO and SrO over an Mg alloy, results in EPBR values greater than 1, hence explaining the protective behavior of these elements as alloying elements in Mg.
2. During the solid-state oxidation of the Mg-2.5Sr-1.0Ca alloy, Ca is the main element being oxidized, increasing its amount over the alloy surface during isothermal holding tests at

500 °C. This element oxidizes preferably due to its high oxygen affinity when compared to Mg and Sr.

3. At the liquid state, Sr on the surface increases as it can spread through the liquid surface, with its oxide being formed at the gas/oxide interface due to its lower oxygen affinity. However, the amount of MgO is still high at this stage.
4. The increase in ignition temperature observed in the alloy seems to be caused by the oxidation of Ca at early stages and the combined, but limited, protection provided by Sr and Ca in the liquid state.

9.1.2 The Mg-Ca Alloys

Two papers presented in this work, analyze the effect of heating rate on the ignition temperature of binary Mg-Ca alloys. The following highlights were drawn:

1. The use of two different heating rates results in different ignition temperatures for Mg-2Ca and Mg-3Ca alloys. A high heating rate (HHR) results in a lower ignition temperature compared to the ones obtained using a low heating rate (LHR). The ignition temperature of pure Mg and the Mg-1Ca alloy is virtually the same using either heating rate.
2. Interrupted ignition tests in the solid, semi-solid and liquid states revealed that the use of an LHR promotes the formation of extensive molten eutectic pools in the semi-solid state. The HHR samples displayed the same molten eutectic pool formation in a lesser degree, along with the formation of numerous internal CaO nodules.
3. Thermodynamic calculations revealed that the molten eutectic pools were more resistant to oxidation compared to the solid intermetallic compound present in the eutectic micro constituent.

4. The early oxidation of the solid intermetallic regions promoted the formation of a mottled and irregular oxide scale. Despite being rich in CaO, this scale would oxidize profusely, lowering the ignition temperature of the sample compared to the more continuous and protective oxide scale developed in the LHR samples.

9.1.3 The Mg-Sr Alloys

The effect of heating rate on binary Mg-Sr alloys was analyzed. Contrary to Mg-Ca alloys, where an improvement in ignition temperature was observed despite using either heating rate, the addition of Sr to Mg displayed a detrimental effect in pure Mg ignition temperature when an HHR was used. The following highlights can be drawn:

1. Ignition temperatures for 1, 1.5, 2.1 and 2.4 wt% Sr additions were close to the melting temperature of each alloy in the HHR samples.
2. Ignition temperature increased to a maximum of 808 °C with 2.1 wt% using an LHR. The addition of 2.4 wt% Sr resulted in a similar temperature (802 °C).
3. As in the Mg-Ca alloys, the main difference observed was in the interrupted ignition test during the semi-solid state. The use of an LHR resulted in the formation of molten pools that were widespread through the alloy. The HHR sample showed vigorous oxidation over the solid $Mg_{17}Sr_2$ intermetallic compound.
4. Using both heating rates, it was seen that SrO nodules are present, and the overall oxide scale is rich in SrO at the gas/oxide interface.
5. The formation of the molten pools in the LHR sample allowed the formation of a continuous oxide scale at the gas/oxide interface.
6. Selective oxidation of the solid intermetallic compounds in the HHR sample causes the formation of a thick oxide scale and numerous oxide nodules. The oxide growth extends

from the interdendritic regions and into the matrix through lateral growth. This induces internal stresses in the oxide scale due to the accelerated oxidation, resulting in early ignition.

7. Despite having an EPBR greater than 1, the close oxygen affinity of Sr and Mg seems to hinder Sr capability of creating a continuous protective oxide scale, as observed in Mg-Ca alloys.

9.2 Future Work

Based on the work presented in this thesis, the following points are proposed for future research work in the development of ignition resistant Mg alloys:

1. According to the work presented in Chapter 4, some potential elements that have an oxygen affinity greater and can develop a protective oxide scale based on their EPBR are presented in table 9.1. It is important to note that the effectiveness of these elements can be limited by their surface-active behavior or the resulting microstructure when alloyed with Mg. Localized oxidation can result in the development of a non-protective oxide scale despite these characteristics:

Table 9.1. Potential alloying elements for the development of ignition resistance Mg alloys.

Proposed element	Oxide	Molar mass g/mol	Density g/cm^3	Molar volume cm^3/mol	EPBR of oxide over a Mg alloy (1.8 g/cm^3)
Er	**Er_2O_3**	382.56	8.64	44.28	**1.6**
Sc	**Sc_2O_3**	137.91	3.86	35.73	**1.3**
Y	**Y_2O_3**	225.81	5.01	45.07	**1.7**
La	**La_2O_3**	325.81	6.51	50.05	**1.9**
Ce	**Ce_2O_3**	328.24	6.20	52.94	**2.0**
Nd	**Nd_2O_3**	336.48	7.24	46.48	**1.7**
Gd	**Gd_2O_3**	362.50	7.07	51.27	**1.9**
Tb	**Tb_2O_3**	365.85	7.91	46.25	**1.7**

2. Third Element Effect: It was seen in this study that a combination of Sr and Ca added to Mg did not lead to the most effective alloy design for ignition resistance. Sr, having lower affinity to oxygen compared to Mg and Ca, oxidizes less. Extensive oxidation of Ca leads eventually to the growth of to a thick oxide that loses its compactness exposing Mg to oxygen. It is argued that an effective alloy design can be possible by combining Ca with an element that oxidizes more than Mg and Ca or one that has affinity between Ca and Mg. The third element should also have an EPBR greater 1. In both cases oxidation of Mg and Ca would be slowed down, a compact scale would form, and its extensive growth would be avoided. Table 9.2 displays the elements that could activate this effect in Mg-Ca binary

alloys, either by having an oxide whose Gibbs energy of formation is intermediate between Mg and Ca or higher than both, making Ca the intermediate element.

Table 9.2. Alloying elements that have an intermediate or higher oxygen affinity (in terms of Gibbs free energy change for their oxides considering 1 mol of O_2) to activate the third element effect.

Elements whose oxide Gibbs free energy change is intermediate between Mg and Ca	**Elements whose oxide Gibbs free energy change is higher than Mg and Ca**
La, Ce, Nd, Gd, Ho, Tb	*Sc, Y, Er*

3. Kinetic studies of binary Mg-Ca and Mg-Sr alloys using different heating rates. This would help to understand the growth rates of the analyzed oxide scales under different conditions.
4. Analyze the effect of geometry in the ignition temperature. It is known that a large surface to volume ratio is detrimental for ignition. However, the presence of sharp corners and edges might play an important role in the integrity of Mg pieces exposed to high temperatures.
5. Flammability testing can be performed on Mg-Sr alloys to observe if the mechanisms observed in the high heating rate tests have the same impact in samples exposed to a direct flame.
6. In-depth analysis of the internal stresses generated due to lateral growth for Mg-Sr alloys. The addition of other alloying elements may reduce stress accumulation and improve the oxide scale covering.

Chapter 10 - Contributions to Original Knowledge

This doctoral study discovered and developed important concepts related to the ignition behavior of Mg alloys.

10.1 The Effect of Heating Rate on Ignition Temperature:

It was determined that for Mg alloys with Ca and/or Sr additions, the ignition mechanism and ignition temperature are dependent on the heating rate. The effect of heating rate was especially important in altering the outcome during the semi-solid stage when heating of the alloy towards the ignition temperature. It was shown that the discrepancy in the ignition temperatures of specifically Mg-alkaline earth alloys can be largely due to the differing heating rates used in ignition tests. This effect can also be investigated for Mg-rare earth alloys in the future. The finding has bearing on the FAA standards on flammability tests that are used in evaluating Mg alloys for aircraft in-cabin applications.

10.2 The Differing oxidation resistance of the second phases in solid and liquid states in Mg-Ca Based Alloys

A very important finding is that thermodynamics predict, and the experimental studies confirm, that the oxidation resistance of the solid eutectic second phase in the interdendritic regions of Mg-Ca based alloys is lower than the oxidation resistance of the molten eutectic micro-constituent during the semi-solid stage. This refutes previous research which suggested that the presence of molten regions during the semi-solid state would be detrimental for ignition resistance due to the enhanced Mg evaporation.

10.3 Effective Pilling Bedworth Ratio

A new concept in the study of Mg ignition, that of Effective Pilling Bedworth Ratio, was developed and used to explain the effectiveness of CaO and SrO on Mg alloys. This new concept removes the confusion in using the conventional Pilling-Bedworth Ratio to explain the protective nature of the oxide scale that forms on an alloy. It reveals that the volume of the oxide scale should be compared to the volume of the Mg alloy and not to the volume of the pure alloying elements.

10.4 Mechanisms of Ignition in in Ternary Mg-Ca-Sr Alloys

This is a very first look at the ignition behavior of Mg-Ca-Sr ternary alloys. More importantly than being merely a first look the study has developed principles for the combined addition of alloying elements to Mg for the purpose of improving the ignition resistance. It was discovered that the principle of third element effect is one of the significant factors for alloy design of ignition-proof Mg alloys. In this study it was seen that Sr did not provide improvement over Mg-Ca alloy. During the solid-state Sr does not provide evident protection, while Ca seems to hinder its performance. It was noted that in general the solid eutectic intermetallic has a lower oxidation resistance.

10.5 Third Element Effect on Mg-Sr-Ca

It was seen in this study that a combination of Sr and Ca added to Mg did not lead to the most effective alloy design for ignition resistance. Sr having lower affinity to oxygen compared to Mg and Ca oxidizes less. Extensive oxidation of Ca leads eventually to the growth of to a thick oxide that loses its compactness exposing Mg to oxygen. It is argued that an effective alloy design can be possible by combining Ca with an element that oxidizes more than Mg and Ca or one that has affinity between Ca and Mg. The third element should also have an EPBR greater 1. In both

cases oxidation of Mg and Ca would be slowed down, a compact scale would form, and its extensive growth would be avoided.